Lightwave, Phonon, and Charge-Transfer Dynamics in Quantum Semiconductors

by

Qiannan Wen

A dissertation submitted in partial fulfillment
of the requirements for the degree of
Doctor of Philosophy
(Applied Physics)
in the University of Michigan
2024

Doctoral Committee:

Professor Mackillo Kira, Chair
Professor Steven Cundiff
Professor Emmanouil Kioupakis
Professor Zetian Mi
Professor Duncan Steel

Qiannan Wen
qnwen@umich.edu
ORCID iD: 0000-0002-4658-8327

© Qiannan Wen 2024

DEDICATION

To my parents.

ACKNOWLEDGMENTS

I would like to express my gratitude to my advisor, Mack Kira, for being a supportive, insightful, and encouraging mentor who taught me lots of things from the fundamentals, walked me through details to understand complex concepts, expanded my view with his great knowledge, and encouraged me to pursue excellence in scientific research.

I want to thank my committee members, Steven Cundiff, Manos Kioupakis, Zetian Mi, and Duncan Steel, for their support throughout my PhD - in teaching, research collaborations, and committee service.

Also, I am grateful to have many wonderful collaborators that enriched this Thesis. I want to thank Rupert Huber (University of Regensburg) for the great experimental resources, and Christian Meineke for the hard experimental work and patience to explain his measurement details. I want to thank Parag Deotare for the chance to work on a variety of interesting topics, and Zidong Li for offering great motivation and insightful discussions. I also want to mention some of the other collaborators, Ping Wang, Yuanpeng Wu, and David Laleyan, on various projects that we have learned together over the years.

I want to thank all my lab mates in Quantum Science Theory Lab, especially Woncheol Lee with whom I explored lots of computational details, Matthias Florian who provided invaluable guidance and mentorship with his expertise in the field, and all the remaining people - Ady Hambarde, Ben Girodias, Cody Patterson, Markus Borsch, Weiwei Jiang, Xiaoying Lu, and You Wu, for the quantum-lunch chat, and for solving challenging problems together.

Finally, I want to thank both families for their love, trust, and support. To my husband, Michael, for sharing good and bad times with me.

TABLE OF CONTENTS

DEDICATION ii

ACKNOWLEDGMENTS iii

LIST OF FIGURES v

LIST OF APPENDICES vi

ABSTRACT vii

CHAPTER

1 Introduction **1**

2 Theoretical Background **5**

2.1 System Hamiltonian 5
2.2 Quantum dynamic cluster expansion (QDCE) 6
2.3 Semiconductor Bloch equations (SBEs) 7
2.4 Local charging in semiconductors 8

3 Unipolar Pulse Generation from Heterostructure Charging Dynamics **11**

3.1 Introduction 11
3.2 Theoretical approach 14
3.2.1 Local charging dynamics 14
3.2.2 Carrier relaxation 17
3.3 Mechanism of unipolar pulses 18
3.4 Control of unipolar pulses 20
3.4.1 Effect of pump field strength 20
3.4.2 Effect of pump field averaging 22
3.4.3 Effect of QW thickness 24
3.4.4 Towards super unipolarity 26
3.4.5 Scalability of peak field 28
3.5 Conclusion 30

4 Terahertz Switching in III-nitride Ferroelectrics **31**

4.1 Introduction 31
4.2 Many-body aspects of ionic latching 32

4.3 Relaxation via Monte Carlo method . . . 34
4.3.1 Decay of the kinetic energy . . . 36
4.3.2 Convergence with the number of realizations . . . 38
4.4 Natural switching time . . . 39
4.4.1 Polarization switching with a linearly ramped field . . . 39
4.4.2 A simple model for tunneling time . . . 41
4.4.3 Classical avalanche time . . . 45
4.5 THz control of polarization switching . . . 46
4.5.1 Multiple switchings with THz pulses . . . 47
4.5.2 Effect of pump duration on switching efficiency . . . 48
4.5.3 Experiment–theory comparison of ultrafast switching . . . 51
4.6 Conclusion and outlook . . . 52

5 Coherent-Phonon Oscillations in Quantum Heterostructures . . . 54

5.1 Introduction . . . 54
5.2 Dynamics of coherent phonon amplitude . . . 55
5.3 Theoretical methods for photoluminescence . . . 56
5.4 Coherent phonon sidebands in TMDC heterobilayers . . . 57
5.4.1 Ultrafast charging . . . 58
5.4.2 Long-lived carrier oscillations . . . 61
5.5 Conclusion and outlook . . . 64

6 Hyperspectral Absorption of Semiconductor Monolayer Crystals . . . 66

6.1 Introduction . . . 66
6.2 Many-body theory for linear absorption in semiconductors . . . 68
6.3 Artificial studies of multilayer absorption . . . 68
6.4 Strategy towards hyperspectral absorbers . . . 70
6.5 Conclusion and outlook . . . 74

7 Excitons in Monolayer Hexagonal Boron Nitride . . . 75

7.1 Introduction . . . 75
7.2 Excitons in ML hBN . . . 76
7.2.1 Symmetry of degenerate excitons . . . 76
7.2.2 Phase in Coulomb matrix elements . . . 78
7.2.3 A reduced model for the phase in Coulomb matrix elements . . . 78
7.3 Natural linewidth of ML hBN . . . 80
7.3.1 Elliott formula for absorption with phonons . . . 81
7.3.2 Natural linewidth of ML hBN . . . 82
7.4 Conclusion and outlook . . . 84

8 Conclusion . . . 85

APPENDICES . . . 88

Bibliography . . . 98

LIST OF FIGURES

FIGURE

2.1 Schematic of Coulomb interactions within a semiconductor, including the repulsive interaction between ions (V^{i-i}) and electrons (V^{e-e}), as well as the attractive interaction between electrons and ions (V^{e-i}). The white and gray spheres indicate ions and electrons, respectively. 8

2.2 Distribution of electrons (gray spheres) and holes (white spheres) in a two-dimensional heterostructure formed by two types of materials indicated by the green and blue regions. (a) With equal distribution of electrons and holes in each material, the system is charge neutral. (b) When electrons and holes are separated into different materials, the system is locally charged, producing a Hartree potential (red line) that changes the energy of electrons along the growth direction. 10

3.1 **Definition of unipolar pulses.** A perfect unipolar pulse (shaded area) with its electric field in one direction only, compared to an asymmetric pulse (red line) where the magnitude of the peak field is larger than that of dip field. 12

3.2 **Shift current in a 2D heterostructure.** (a) Optical excitation (red arrow) of electrons from the valence band (dashed line) to the conduction band (shaded area), generating (b) a short burst of shift current $J(t)$ and (c) bipolar electric field. (d) The separation of electrons (gray circles) and holes (white circles) creates a charging potential (red line) that pulls electrons and holes towards the interface. 13

3.3 **Mechanism of unipolar pulses**. (a) Mean positions of electrons (red solid line) and holes (red dashed line) from full results, compared to electron (black solid line) and hole (black dashed line) positions when Hartree potential is switched off. The color-coded background depicts spatial distribution of electron density from full results. (b) Shift current $J(t)$ and (c) electric field from full results (red) and results obtained without Hartree potential (black). The envelope of pump field is indicated by shaded area. All quantities are normalized to have peak field along positive direction. The vertical lines indicate peak time of electric field from full computations. 19

3.4 **Pump field strength dependence of THz transients.** (a) THz transients and (b) the maximal Hartree potential along the growth direction for different pump strengths (in arbitrary units) $E_{\mathrm{pump}} = 0.5$ (black dashed line), $E_{\mathrm{pump}} = 1.0$ (red line), and $E_{\mathrm{pump}} = 2.0$ (cyan line). The peak fields are indicated by vertical dotted lines. The shaded area indicates envelope of pump field. (c) Peak field in THz transients and (d) unipolarity computed from dip1 before main peak (dashed line) and dip2 after main peak (solid line) as function of the ratio of pump strength to unipolarity threshold. 21

3.5 **Effect of pump field averaging on the shape of THz transients.** (a) The spatial distribution of field strength for Gaussian (shaded area) and parabolic (red solid line) profiles. The dashed horizontal lines indicate cutoff in field strengths used in averaging. Normalized THz field for (b) Gaussian and (c) parabolic beam profiles averaged over full area (shaded area), and with cutoff in field strength at $E_c = 0.25E_0$ (black lines) and $E_c = 0.50E_0$ (red lines). 23

3.6 **Enhancement of peak field strength with QW thicknesses.** (a) The first few states in the valance band of 7nm/7nm double QWs. The vertical dashed lines indicate mean positions of the first state on left (z_L) and right (z_R) side. (b) Distance between left and right states $d_{L,R}$ (black line, on the left axis) and THz peak field (red line, on the right axis) as function of L_2. (c) Mean positions of electrons (solid lines) and holes (dashed lines), and (d) corresponding electric field for the QWs with right-layer thickness $L_2 = 3.5$ nm (black lines), $L_2 = 5.5$ nm (blue lines), and $L_2 = 7.0$ nm (red lines). The vertical lines mark the moments when the fields reach their peak strengths. The shaded area indicate pump-field envelope. 25

3.7 **Experiment–theory comparison of peak field enhancements via QW thicknesses.** (a) Experimental measurements of THz field from QWs of thicknesses 7.0 nm/3.5 nm (black line) and 7.0 nm/7.0 nm (red line) on the left/right side. (b-c) Theory predictions of electric field for the corresponding structures without (b) and with (c) pump field averaging. 26

3.8 **Super unipolarity via engineering the number of states on two sides of the double-QW interface.** (a) The first few hole subband states in double-QW structures. The letter indicates the mean position of each state on the left (L) or the right (R) side of the interface starting with the state with the highest valance-band energy. (b) Mean positions of electrons (solid lines) and holes (dashed lines) and (c) corresponding electric field from three structures shown in (a) with unipolarity of uni=4 (LLLR), uni=5 (LLRR), and uni=15 (LRRR). The electric field in (c) is scaled to have same magnitude at the first dip near $t = -290$ fs. (d) Normalized THz emission spectra. 27

3.9 **Peak field scalability.** (a) Peak field of THz transients as function of the ratio between pump field strength and unipolar threshold E/E_{uni} for the LLLR (black line), LLRR (blue line), and LRRR (red line) structures. (b) Unipolarity computed from the dip before main peak (Dip1) and the dip after main peak (Dip2). The black, blue, and red solid (dashed) lines represent electrons (holes) in the LLLR, LLRR, and LRRR strucures. (c) THz field at selected pump field strengths $E = E_{uni}$ (black line), $E = 1.3\ E_{uni}$ (cyan line), $E = 1.9\ E_{uni}$ (red line), and $E = 2.7\ E_{uni}$ (blue line) for the LRRR structure. The envelope of pump field in indicated by shaded area. . . . 29

4.1 **Coulomb effects on ionic potential and distribution.** (a) A double-well potential U_{DW} (shaded area) with two valleys at $z = \pm z_0$. The ionic density (blue line) is symmetrical on two sides, resulting in a vanishing polarization. (b) The ionic potential with many-body Coulomb effects (shaded area) and the shifted ionic distribution (blue line). 32

4.2 **Decay of kinetic energy due to relaxation.** (a) The color-coded plot of ionic density during the excitation of a Gaussian pulse (red line). The white line indicates the mean position of ion. (b) Numerical results (black solid line) of kinetic energy during the switching, compared to the analytics (red dashed line). 37
4.3 **Convergence with the number of realizations.** The error in the mean position of ion as a function of the number of realizations N, with respect to the reference computed from $N_0 = 2 \times 10^4$ realizations. 38
4.4 **Polarization switching under a linearly ramped field.** (a) Color-coded plot of ionic density close to the switching. The external field $E(t)$ (red line) is linear in time. The vertical dashed lines are selected times at which the wave functions $|\phi|^2$ (shaded areas) and full potential energy V (red solid lines) are shown in (b-c). The black dashed lines indicate double-well potential without charging or external field. The red horizontal dashed lines indicate the total energy of ion at selected times. (d) Tunneling region as function of time. The vertical solid indicates the vanishing of tunneling region. 40
4.5 **A simple model for the tunneling threshold.** a) Ionic density (color-coded background) under a constant electric field (red line) turned on at $t = 0$. (b) Kinetic energy E_k, potential energy V, and the total energy of the ion $E_{ion} = E_k + V$ as a function of time. The vertical lines in (a-b) indicate the selected times at which the ionic potentials $V_d(z)$ are shown in (c). The average position of the ion d_1, d_2 are indicated by vertical lines. The horizontal dashed line indicates E_{ion} that is kept constant at $t > 0$. 43
4.6 Probability of wave function on the right side R as function of d/z_0. The solid line shows R from full results, and the red dashed line shows the linear model. The vertical line indicates the threshold ionic position d_{th} for which the tunneling is removed. 44
4.7 **Probability current during tunneling.** (a) Scaled probability current $\Delta R_j = j\Delta t$ at selected ionic positions $\langle z \rangle = -0.7z_0$ (black line), $\langle z \rangle = -0.6z_0$ (red line), and $\langle z \rangle = -0.5z_0$ (cyan line), during a time interval of $\Delta t = 100$ fs. (b) Magnitude of the scaled probability current ΔR_j at the center of two valleys ($z = 0$). 45
4.8 **Classical avalanche time.** (a) Ionic wave function $|\phi|^2$ (shaded area) and the potential (red line) at the onset of classical transition. In classical model, we assume a particle is released at $z = -0.3z_0$ (light blue sphere) with a small initial velocity to the right side. Due to the lower potential on the right side, it moves to the potential minimum (dark blue sphere). (b) Average position and (c) velocity from full computation (shaded areas), compared to classical dynamics (blue lines). The position of the particle in classical model is shifted to full results at $t = 0$. 46
4.9 **Ultrafast switching driven by THz field.** (a-c) Color-coded plot of ionic density driven by THz field with durations of (a) 0.75 cycles, (b) one cycle, and (c) two cycles at the frequency of $\nu = 0.2$ THz. The blue shaded areas indicate the THz field. (d) Emission spectra of polarization switching under pump field of the durations of 0.75 cycles (black dashed line), one cycle (red solid line), and two cycles (gray shaded area). 47

4.10 **Effect of pump duration on switching efficiency.** (a) The maximum R during the pump pulse (black line) and the final R after the pump (red line) as a function of τ/T_{flip}. The shaded area indicate the regime where the flip is reversible. (b) The maximal E_k during the excitation (black line) compared to the potential depth V_{depth} for the ion to move to the center. (c) Color-coded plot of ionic density for selected cases $\tau/T_{flip} = 0.3$ (top frame), 1.0 (middle frame), and 3.6 (bottom frame). The white line shows the average ionic position, and shaded area shows the pump field. 49
4.11 Switching efficiency R as a function of τ/T_{flip}, for selected ratios between relaxation time and the flip time τ_{rlx}/T_{flip}=1.6 (black line), 0.8 (red line), and 0.4 (cyan line). . . 50
4.12 **Experiment–theory comparison of ultrafast switching.** Normalized THz fields from (a) ferroelectric $Sc_{0.1}Al_{0.9}N$ and (b) a control sample of silicon at pump power of 17.5 W (black line), 35.0 W (blue line), and 70.0 W (red line). (c) Computed field without (shaded area) and with (red line) polarization switching. The field strengths are scaled to be the same at t=-0.5ps before switching occurs. (d) Ionic density (color-coded background) and mean position (white line) under strong excitations. The gray shaded area indicates the THz pump field. 52

5.1 Relative oscillation amplitude A_{osc} of coherent phonons as a function of the ratio between charge switch time τ and phonon period T. 59
5.2 **Coherent phonon sidebands in $MoSe_2$/WSe_2 heterobilayers with ultrafast charging.** (a) Schematic of $MoSe_2$/WSe_2 heterobilayers, including the lowest conduction band in each material and a single valance band from WSe_2 monolayer. The electron wave functions for two conduction bands are shown in shaded areas. (b) Electron density in $MoSe_2$ monolayer (black lines) with pump durations τ=10 fs (top row), 40 fs (middle row), and 100 fs (bottom row). (c) Band gap oscillations and (d) PL near 1s-exciton energy with different pump durations. 60
5.3 Amplitude of coherent-phonon oscillations as a function of pump duration τ, at selected ratios $r = 10^{-5}$ (black line), $r = 10^{-4}$ (red line), $r = 10^{-3}$ (cyan line) representing the fraction of total carrier density that oscillates at phonon frequency. 62
5.4 **Coherent phonon sidebands induced by phonon-coupled carrier oscillations.** (a) Carrier density N^e in the $MoSe_2$ monolayer without (shaded area) and with (red solid line) phonon-coupled carrier oscillations. The red dashed line shows the amplitude of the oscillations in carrier density relative to total density. (b) Change in band gap without (black line) and with (red line) phonons. The inset shows a zoomed-in plot in the time window indicated by blue area in the main frame. (c) Computed PL near 1s-exciton energy without (shaded area) and with (red line) phonon-coupled oscillations. The vertical dashed lines indicate phonon energies relative to ZPL. (d) Experimental data of PL in $MoSe_2$/WSe_2 heterobilayers under the excitation by a continuous-wave laser (black line) and a 20 ps pump pulse (red line). 63

6.1 (a) Color-chirped monolayer (ML) array near a mirror. The barriers between monolayers have a thickness L, and a mirror is distance L_m away from the first monolayer. (b) MLs color chirped to have *different* excitonic resonances, producing a broadband absorption. 67

6.2 (a) Absorption of N=1, 10, 120 TMDC-type monolayers at $\lambda_{1s}/4$ distance from a mirror. Blue vertical lines mark the 1*s*, 2*s*, and continuum energies. (b) Absorption peak as a function of $r(N) = \gamma/\Gamma(N)$. 69
6.3 Absorption spectra of N=120 identical monolayers positioned at (a) L=0, (b) L=10 nm and (c) L=$\lambda_{1s}/2$ spacing. For each case, the absorption from full states (shaded area) is compared to that without $n_{1s} \equiv \mathrm{Re}[\xi_{1s}]$ (red line) or without $\alpha_{1s} \equiv \mathrm{Im}[\xi_{1s}]$ (black line). 71
6.4 (a) Average absorption within 2 eV bandwidth as a function of N. Absorption spectrum of (b) N=120 TMDC monolayers, (c) N=700 nitride monolayers and (d) N=240 GaAs quantum wells, color-chirped (solid line) vs fixed-energy (shaded area) structures. 73

7.1 **Wave functions for the 1s exciton in ML hBN.** (a-b) Absolute value of exciton wave functions for the degenerate 1s states obtained from GW and BSE calculations (Woncheol Lee). (c) The relative phase $\theta_{1,2}$ of the excited state $\lambda = 2$ with respect to ground state $\lambda = 1$. (d) Phase-smoothed exciton wave functions under exciton gauge along the high-symmetry line. 77
7.2 **Phase in Coulomb matrix elements under exciton gauge.** (a) Cosine and (b) sine of the phase $\theta_{\mathbf{k},\mathbf{k}'}$ in the Coulomb matrix elements with $\mathbf{k} = K$. 79
7.3 **A reduced model for the in Coulomb matrix elements.** (a) Exciton energies of the ground state ($\lambda = 1$, black solid line) and the first excited state ($\lambda = 2$, black dashed line) computed with the Gaussian model. The vertical line indicates the selected parameter for which the wave functions of two lowest excitons are shown in (b-d), comparing results from BSE and that from the reduced model in SBE. (e) Cosine of the phase in Coulomb matrix elements in the reduced model. 80
7.4 **Absorption linewidth and energy shift with phonons.** (a) Imaginary part of linear susceptibility near 1s-exciton energy without phonon (shaded area) and with phonon at $T = 12$ K (black line), 100 K (red line), and 300 K(cyan line). (b) Imaginary part and (c) real part of $z(\omega) = z^+(\omega) + z^-(\omega)$ using the same color scheme as (a). (d) Halfwidth and (e) energy shift of 1s exciton as a function of temperature. 83

LIST OF APPENDICES

Appendix A. Energy Conservation with Dynamic Charging **88**

Appendix B. Wannier Equation with General Coulomb **90**

Appendix C. Elliott Formula for Absorption with Phonon **93**

Appendix D. Author's Contributions **96**

ABSTRACT

Quantum semiconductors, when engineered at the nanoscale or even down to atomic-layer thickness, display tunable electronic states and strong interactions among charge carriers. The heterostructures formed by stacking different materials are an exciting platform for interface physics and novel quantum phases. Understanding how electrons move within solids and at the interface of different materials is the key to advancing semiconductor electronics and future quantum devices. This Thesis presents theoretical methods I have developed to describe the motion of charge carriers and crucial insights for controlling carrier motion in semiconductors, designing novel quantum materials, and advancing the field of quantum technology.

In semiconductor heterostructures, the positive and negative charges often separate spatially, causing local charging. Based on semiconductor Bloch equations, I develop a method to study how this impacts charge-transfer dynamics. Our calculations in a double-quantum-well system reveal that a significant local charging prompts electrons and holes to move towards the interface to counterbalance the charging. This unique charge-transfer dynamics leads to the emission of a subcycle unipolar pulse which has its electric field significantly stronger in one direction than the other. This type of pulse is highly desired as a control source to move electronic states along one direction near its peak field, while the back motion due to negative peaks is negligible. Experimental results confirm the creation of these unipolar pulses in the spectral range of terahertz fields, an important step towards ultrafast, unidirectional control of quantum states to overcome decoherence challenges in quantum information processing.

The local charging aspects are then extended to describe the ionic motion in semiconductors. This is particularly interesting in ferroelectric materials, where a spontaneous electric polarization is present due to lattice asymmetry and can be switched by external electric fields. I present a quantum dynamic theory to describe the detailed switching process of this electric polarization. Our results demonstrate ultrafast, sub-picosecond switching time in nitride ferroelectrics enabled by local charging. In addition, I discuss the potential of controlling polarization switching using terahertz fields. As the switchable polarization is a key element in memory devices and could potentially encode quantum information, our findings shed light on using ferroelectrics for high-speed electronics and quantum computing.

Beyond influencing charge carriers, local charging also disturbs the crystal lattice via the in-

teraction between electrons and lattice vibrations. I discuss a particular type of lattice dynamics known as coherent-phonon oscillations, which correspond to a macroscopic lattice displacement under ultrafast excitations. I present a detailed discussion on the mechanism of coherent-phonon oscillations and the spectroscopic features they lead to. Specifically, in transition metal dichalcogenide heterobilayers, I explore different scenarios where the charge transfer between the bilayer can induce coherent-phonon oscillations and sidebands. Our results demonstrate the potential of using coherent phonon sidebands to study charge-transfer dynamics in heterostructures.

Finally, aiming at reaching ultrabroadband absorption via semiconductor heterostructures, I apply many-body theory to compute the absorption of artificial crystals formed by stacking semiconductor monolayers. Our results show that by combining strong, peaked excitonic absorption with intrinsically broad continuum absorption enhanced by radiative coupling among monolayers, hyperspectral absorption can be realized that covers the spectrum of sunlight. This prediction shows the potential of using quantum materials for efficient solar cells. The design principles I present also offer important guidance to the development of quantum heterostructures that utilize collective coupling among different materials.

CHAPTER 1

Introduction

Semiconductors are solid-state materials with band gaps of a few eV. Under optical excitation of semiconductors, electrons transition from the valence band to the conduction band, leaving vacancies in the valence band known as holes. The electron and hole bind together via the attractive Coulomb interaction to form an exciton. In addition, atoms within a semiconductor vibrate around their equilibrium positions, a process that can be described by phonon. Semiconductors play a fundamental role in modern electronics, owing to their electrical transport and optical properties [1–3]. Since the 1980s, advancements in semiconductor fabrication have allowed for the growth of quantum structures smaller than the Bohr radius in some dimensions. An example among such structures is the quantum well. This is a thin layer of semiconducting material, typically with a thickness ranging from 10 to 100 nm, which is placed between two barrier layers. A key characteristic of this structure is its ability to confine electrons and holes within the plane of the quantum well, resulting in discrete energy levels. Quantum confinement also allows for tuning electronic band energies by changing the size of the structure. Moreover, materials with similar lattice structures but different band gaps can be grown on top of each other to form heterostructures. The development of these structures has led to the advancement of various electronic devices including solar cells, light emitting diodes, and semiconductor lasers.

Since the groundbreaking discovery of graphene in 2004 [4], the field of quantum semiconductor research has entered a new phase where the material is reduced to a single atomic-layer thickness. These ultrathin materials are commonly known as two-dimensional (2D) materials. In addition to graphene, the realm of 2D materials includes a variety of materials. Notable among these are transition metal dichalcogenide (TMDC) monolayers, nitrides monolayers, and 2D oxides. The electronic and optical properties of these 2D materials are markedly distinct from those observed in their bulk forms. The first experimental demonstration of the direct gap in a monolayer of MoS_2 was conducted in 2010 [5], where the crossover from indirect to direct gap was shown as the thickness decreases from a few layers to a single layer. In 2D materials, charge carriers experience strong Coulomb interactions. This is evident in the exciton binding energies of nitride monolayers [6] and TMDC monolayers [7], which can reach hundreds of meV. These

values are an order of magnitude larger than those found in bulk materials. Similar to quantum well heterostructures, 2D materials can also be stacked together to form heterostructures. For example, the stacked bilayer of TMDCs with different materials typically form a type-II aligned heterostructure [8], where the conduction band minimum and valence band maximum are located in different materials. Upon optical excitation, electrons and holes are separated into different materials. This process occurs on the ultrafast time scale of sub-100fs. [9, 10] The interlayer exciton, which is formed by an electron and a hole from different materials, has a lifetime on order of 100 ns, significantly larger than the lifetime of excitons within a monolayer. [11] The development of these heterostructures opens up the possibility of creating artificial crystals, where the electronic and optical properties can be precisely tailored by the design of atomic layers they consist of. [12] Given the complexity of the lattice structures and materials compositions, it is crucial to systematically address the interactions both within a monolayer and among different materials during the development of these artificial crystals.

One of the key aspects in this Thesis is ferroelectric semiconductors, a class of materials having an electric polarization in the absence of an electric field. This polarization arises from the asymmetry in lattice structure where a relative separation between positive and negative ions occurs within each unit cell. Moreover, the direction of this polarization can be reversed by applying an external electric field. Typically, ferroelectrics are characterized by the hysteresis loop, observed in their polarization as the electric field changes. The phenomenon of ferroelectricity was first observed in Rochelle salt in 1921. [13] After that, research in the field of ferroelectric materials shifted focus towards perovskite materials. [14, 15] A significant advancement was made in the year of 2019 when ferroelectricity was demonstrated in ScAlN, a semiconductor belonging to the III-nitride family. [16] Typically, nitride materials do not exhibit ferroelectric properties. However, ScAlN becomes ferroelectric as a result of the reduced barrier in the ionic potential when scandium atoms are added to AlN, which was computed in Ref. [17]. A key feature of ferroelectric materials is their remnant polarization, which has enabled their use in memory devices. This application has been commercially available since the 1990s. [18, 19] One important measure of memory devices is the switching time, which affects the efficiency of the memory and the overall computing speed. Typically, the switching time of ferroelectric memories is on the order of nanoseconds [20]. Due to the escalating demands for big data processing, increasing the operation speed of ferroelectric memory devices will make a breakthrough in high-speed computing. [19] The intrinsic speed at which ferroelectric polarization switching occurs, governed by their fundamental properties such as atomic mass and ionic potential, remains not well understood. This highlights the need for a detailed microscopic theory to better comprehend the switching behavior of ferroelectrics.

The dynamic processes within a semiconductor can be manipulated using light pulses. Under

optical excitations, changes of electronic states within the semiconductor are affected by multiple factors of the pump fields, including their central frequencies, intensities, and durations. Ultrafast pump pulses, typically with a duration about 100 fs, have been employed to study the motion of electrons in semiconductors. Some examples include measurement of band structures [21], monitoring of carrier relaxation [9], and high-harmonic generation [22]. In an emerging field of lightwave electronics (LWE) [23], the time scale to manipulate electronic states is further reduced, reaching the limit below a single optical cycle. Lightwave electronics use a strong, ultrashort light pulse to instantaneously alter the electronic states of a material when the light pulse reaches its peak field. [23] This concept was initially demonstrated on dielectric materials using few-cycle optical pulses to induce the switching of electric current in the petahertz range. [24] Since then, the control of electronic states via LWE has been broadened to different systems, including molecules [25] and 2D quantum materials [26]. The realization of ultrafast control of semiconductors is crucial not only for enhancing the operation speed of optoelectronic devices but also holds promise for harnessing the quantum properties of semiconductors for information processing [23, 26, 27].

Apart from manipulating electronic states, ultrafast light pulses can also affect lattice vibrations in solid state systems. It has been observed on a variety of systems [28–32] that when the material is excited by strong, femtosecond pump pulses, oscillations are detected in transmission or reflection in the time domain. These oscillations are characterized by the phonon frequencies within the material. They are a type of lattice dynamics, known as coherent-phonon oscillations [33, 34], which corresponds to a macroscopic lattice displacement under ultrafast excitations. In this scenario, an ultrafast pump pulse with a duration of about 100 fs excites a large number of charge carriers within the material. Due to the interactions between electrons and phonons, the crystal lattice structure experiences significant disturbance due to alterations in the electronic states. This leads to the generation of coherent-phonon oscillations before the lattice relaxes to equilibrium. A straightforward way to visualize this phenomenon is by considering a simple harmonic oscillator. Imagine if the equilibrium position of this oscillator is suddenly shifted. In response, the particle will start to oscillate around this new position. Similarly, when the lattice structure within a material is altered on a time scale shorter than its typical atomic vibration cycles, coherent phonon oscillations are driven. The microscopic process by which coherent-phonon oscillations are generated in quantum heterostructures remains unclear. This includes understanding how these oscillations are connected to the charge-transfer process within the semiconductor. Understanding the fundamental mechanism of coherent-phonon oscillation is crucial to assess the effect of lattice dynamics on the electronic behaviors of semiconductors, and to explore possibilities of the coupling between electronic and vibrational degrees of freedom to manipulate quantum states in semiconductors.

The study of semiconductors is a many-body problem due to the interactions between a large number of electrons and phonons, as well as their interactions with optical fields. Understanding even basic processes such as light absorption and the motion of charge carriers is a challenging task. Quantum dynamic cluster expansion (QDCE) [35] is a systematic approach for describing the quantum kinetics in semiconductors. This method includes the interactions between electrons, lattice vibrations, and optical fields at the microscopic level. [35] The basic idea of QDCE is that the many-body quantities are grouped into clusters based on the number of interacting particles. [35] In numerical computations, the first few clusters are solved precisely, while higher-order clusters are truncated. [35] In this Thesis, I apply QDCE to study charge-transfer mechanisms, absorption features, and effect of lattice vibrations in various systems including quantum-well heterostructures, TMDC bilayers, III-nitride ferroelectrics, and monolayer semiconductors.

This Thesis is organized as follows. In chapter 2, a brief introduction to the theoretical background of the many-body Hamiltonian and QDCE is presented. In chapter 3, I study the mechanism for generating a subcycle light pulse via the motion of charge carriers in quantum well heterostructures. This pulse is characterized by its asymmetry where the electric field in one direction is much stronger than that in the other direction, referred to as a unipolar pulse. In chapter 4, I present a quantum dynamic theory for the ionic motion during polarization switching in ferroelectric materials. This theory includes many-body Coulomb interactions, upon which the natural switching process is analyzed in a microscopic picture. I also discuss the potential of using light fields in the terahertz frequency to control the polarization switching. In chapter 5, I discuss the mechanism of coherent phonon oscillations in semiconductor heterostructures. The coherent phonon oscillations and the corresponding spectroscopic features are computed for TMDC bilayers. In chapter 6, I outline the design principles of ultrabroadband absorbers via collective coupling among semiconductor monolayer crystals. In chapter 7, I explore excitonic properties of monolayer hexagonal boron nitride showing unusual Coulomb interactions as the key to understanding exciton symmetries. In chapter 8, I summarize key findings in this Thesis and discuss future work that are essential for advancing quantum materials and quantum technologies.

CHAPTER 2

Theoretical Background

In solid-state systems, there are a large number of particles interacting with each other, making direct computations of wave functions complex. In this Chapter, I provide a brief review of the method, discussed in detail in Ref. [35], for solving quantum dynamics in semiconductors - a topic further explored in subsequent chapters. We start with the system Hamiltonian in second quantization, and introduce quantum dynamic cluster expansion (QDCE) which is a systematic way for analyzing many-body interactions. Based on QDCE, we introduce semiconductor Bloch equations (SBEs) that are used to compute the dynamics of semiconductors. Additionally, we discuss the effects of electron–hole separation that often occur in heterostructures formed by different materials. This Chapter is largely based on the concepts and methods presented in Ref. [35].

2.1 System Hamiltonian

In constructing system Hamiltonian in second quantization, it is standard to use Bloch states of electrons as a basis. The system Hamiltonian including single-particle electron energy, phonon energy, light–matter interaction, Coulomb interaction, and electron–phonon interaction reads [35]

$$\begin{aligned}\hat{H} = &\sum_{\lambda,\mathbf{k}} E_{\lambda,\mathbf{k}}\ \hat{a}^{\dagger}_{\lambda,\mathbf{k}}\hat{a}_{\lambda,\mathbf{k}} + \sum_{\mathbf{p}} \hbar\Omega_{\mathbf{p}}\ D^{\dagger}_{\mathbf{p}}D_{\mathbf{p}} \\ &- \sum_{\lambda,\lambda'\neq\lambda}\sum_{\mathbf{k}} \mathbf{d}^{\lambda,\lambda'}_{\mathbf{k}}\cdot\mathcal{E}(t)a^{\dagger}_{\lambda,\mathbf{k}}a_{\lambda',\mathbf{k}} + \frac{1}{2}\sum_{\lambda,\lambda'}\sum_{\mathbf{k},\mathbf{k}',\mathbf{q}\neq 0} V^{\lambda,\lambda'}_{\mathbf{q}}\hat{a}^{\dagger}_{\lambda,\mathbf{k}}\hat{a}^{\dagger}_{\lambda',\mathbf{k}'}\hat{a}_{\lambda',\mathbf{k}'+\mathbf{q}}\hat{a}_{\lambda,\mathbf{k}-\mathbf{q}} \\ &+ \sum_{\lambda,\lambda'}\sum_{\mathbf{k},\mathbf{p}} G^{\lambda,\lambda'}_{\mathbf{k},\mathbf{p}}\ \hat{a}^{\dagger}_{\lambda,\mathbf{k}+\mathbf{p}}\hat{a}_{\lambda',\mathbf{k}}\left(\hat{D}_{\mathbf{p}} + \hat{D}^{\dagger}_{-\mathbf{p}}\right)\ , \end{aligned} \tag{2.1}$$

where $a^{(\dagger)}_{\lambda,\mathbf{k}}$ is the annihilation (creation) operator for the electron at band λ and crystal momentum $\mathbf{k}$, $D^{(\dagger)}_{\mathbf{p}}$ is the phonon annihilation (creation) operator at wavevector $\mathbf{p}$, $E_{\lambda,\mathbf{k}}$ is electron band energy, $\hbar\Omega_{\mathbf{p}}$ is the phonon energy, and $\mathcal{E}(t)$ is the electric field amplitude. We use envelope-function

approximation [35] for electron wave function $\phi_{\lambda,\mathbf{k}}(\mathbf{r}) = \xi_\lambda(z)\frac{e^{i\mathbf{k}_\parallel\cdot\mathbf{r}_\parallel}}{\mathcal{L}}u_{\lambda,\mathbf{k}}(\mathbf{r})$, where $\xi_\lambda(z)$ is the confinement along z direction, $\mathcal{L}$ is the quantization length, $\mathbf{k}_\parallel$ is the in-plane crystal momentum, and $u_{\lambda,\mathbf{k}}(\mathbf{r})$ is the cell-periodic Bloch function. In Eq. (2.1), $\mathbf{d}_\mathbf{k}^{\lambda,\lambda'}$ is the dipole matrix element and $V_\mathbf{q}^{\lambda,\lambda'}$ is Coulomb matrix element defined via [35]

$$\mathbf{d}_\mathbf{k}^{\lambda,\lambda'} = \frac{1}{\Omega_0}\int_{\Omega_0} d^3r\; u^*_{\lambda,\mathbf{k}}(\mathbf{r})\; e\mathbf{r}\; u_{\lambda',\mathbf{k}}(\mathbf{r})\;, \tag{2.2}$$

$$V_\mathbf{q}^{\lambda,\lambda'} = \frac{e^2}{2\epsilon_0\epsilon_r\mathcal{L}^2|\mathbf{q}|}\int dz\int dz'|\xi_\lambda(z)|^2|\xi_{\lambda'}(z)|^2\; e^{-|q(z-z')|}\;, \tag{2.3}$$

where Ω_0 is the volume of the unit cell, e is the electron charge, ϵ_0 is the vacuum permittivity, and ϵ_r is the dielectric constant. In addition, the electron–phonon matrix element in Eq. (2.1) are [36]

$$G_{\mathbf{k},\mathbf{q}}^{\lambda,\lambda'} \equiv \frac{1}{\sqrt{N}}\langle u_{\lambda,\mathbf{k}+\mathbf{q}}|\Delta_\mathbf{q}\nu^{KS}|u_{\lambda',\mathbf{k}}\rangle\;, \tag{2.4}$$

$$\Delta_\mathbf{q}\nu^{KS} \equiv \sum_{n,\kappa,\alpha}\sqrt{\frac{\hbar}{2M_\kappa\Omega_\mathbf{q}}}e_{\kappa,\alpha}(\mathbf{q})\frac{\partial V^{KS}}{\partial R_{\kappa,n,\alpha}}e^{-i\mathbf{q}\cdot(\mathbf{r}-\mathbf{R}_n)}\;, \tag{2.5}$$

where N is the number of unit cells, n,κ,α are indices for the unit cell, the ion within a unit cell, and Cartesian coordinate used in the calculation, respectively. Also, $\hbar$ is the reduced Planck constant, M_κ is the ionic mass, $\Omega_\mathbf{q}$ is phonon frequency, and $e_{\kappa,\alpha}(\mathbf{q})$ is phonon eigenvector, V^{KS} is the Kohn-Sham potential [37], and $\mathbf{R}$ is the lattice vector. In the work discussed in this Thesis, electron–phonon matrix elements are computed from first-principles calculations by Woncheol Lee and Matthias Florian. The system Hamiltonian shown in Eq. (2.1) serves as a starting point for computing the dynamics of semiconductors discussed in the following.

2.2 Quantum dynamic cluster expansion (QDCE)

Based on the system Hamiltonian given in Sec. 2.1, the dynamics of an operator is calculated using the Heisenberg equation of motion

$$i\hbar\frac{\partial}{\partial t}\hat{O} = [\hat{O},\;\hat{H}]_-\;. \tag{2.6}$$

For a general N-particle expectation value $\langle N\rangle$, the dynamics cannot be solved in a closed form due to its coupling to the $(N+1)$-particle quantities via Coulomb, light–matter, and electron–

phonon interactions. The hierarchical coupling has the general form [35]

$$i\hbar\frac{\partial}{\partial t}\langle N\rangle = T[\langle N\rangle] + H[\langle N+1\rangle]\ , \tag{2.7}$$

where $T\left[...\right], H\left[...\right]$ denote functionals of the expectation value.

In cluster expansion [35], $\langle N\rangle$ is factorized into different clusters catergorized by the level of complexity. Singlets $\langle 1\rangle$ are independent single particles. The Bosonic singlets include coherent photon $\langle B\rangle$ and coherent phonon $\langle D\rangle$. The carrier singlets include coherent polarization ($\lambda \neq \lambda'$) and density ($\lambda = \lambda'$) in the form $\langle a^\dagger_{\lambda,\mathbf{k}} a_{\lambda',\mathbf{k}'}\rangle$, where a pair of Fermionic operators is defined as one particle. In the next level, doublet $\Delta\langle 2\rangle = \langle 2\rangle - \langle 2\rangle_s$ is a two-particle correlation that describes an interacting pair. The higher-order clusters are defined recursively. The quantum dynamic cluster expansion (QDCE) approach [35] addresses the hierarchical problem by solving the exact dynamics for the first few clusters and truncating high-order clusters. The level of this simplification depends on the experimental conditions and the key features we aim to investigate. Due to the sequential built-up of higher-order correlations, it typically provides a good approximation for semiconductors excited by classical fields on the ultrafast time scale.

2.3 Semiconductor Bloch equations (SBEs)

Starting from the general structure QDCE, the singlet dynamics defines semiconductor Bloch equations (SBEs) [35]. For a homogeneous system, only terms with $\mathbf{k} = \mathbf{k}'$ in the carrier singlet $\langle a^\dagger_{\lambda,\mathbf{k}} a_{\lambda',\mathbf{k}'}\rangle$ do not vanish. We denote $P^{\lambda,\lambda'}_{\mathbf{k}} = \langle a^\dagger_{\lambda,\mathbf{k}} a_{\lambda',\mathbf{k}}\rangle$ for the singlet between electronic bands λ and λ'. The dynamic equations for the optical polarization $P^{v,c}_{\mathbf{k}}$, and densities of electrons $f^e_{\mathbf{k}} = P^{c,c}_{\mathbf{k}}$ and holes $f^h_{\mathbf{k}} = 1 - P^{v,v}_{\mathbf{k}}$ are [35]

$$i\hbar\frac{\partial}{\partial t}P^{v,c}_{\mathbf{k}} = \left(\tilde{E}^e_{\mathbf{k}} + \tilde{E}^h_{\mathbf{k}}\right)P^{v,c}_{\mathbf{k}} - \left(1 - f^e_{\mathbf{k}} - f^h_{\mathbf{k}}\right)\Omega^{v,c}_{\mathbf{k}} + \Gamma^{v,c}_{\mathbf{k}}\ , \tag{2.8}$$

$$\hbar\frac{\partial}{\partial t}f^e_{\mathbf{k}} = 2\ \mathrm{Im}\left[P^{v,c}_{\mathbf{k}}\left(\Omega^{v,c}_{\mathbf{k}}\right)^* + \Gamma^{c,c}_{\mathbf{k}}\right]\ , \tag{2.9}$$

$$\hbar\frac{\partial}{\partial t}f^h_{\mathbf{k}} = 2\ \mathrm{Im}\left[P^{v,c}_{\mathbf{k}}\left(\Omega^{v,c}_{\mathbf{k}}\right)^* - \Gamma^{v,v}_{\mathbf{k}}\right]\ , \tag{2.10}$$

where $\tilde{E}^\lambda_{\mathbf{k}} = E^\lambda_{\mathbf{k}} - \sum_{\mathbf{k}'} V^{\lambda,\lambda}_{\mathbf{k}-\mathbf{k}'} f^\lambda_{\mathbf{k}'}$ is the renormalized band energy in the presence carriers, $\Omega^{v,c}_{\mathbf{k}} = d^{v,c}_{\mathbf{k}}\mathcal{E}(t) + \sum_{\mathbf{k}'} V^{v,c}_{\mathbf{k}-\mathbf{k}'} P^{v,c}_{\mathbf{k}'}$ is the renormalized Rabi energy, and $\Gamma^{\lambda,\lambda}_{\mathbf{k}}$ is doublet due to Coulomb and phonon interactions. In this Thesis, we use SBEs to compute for semiconductors under the excitation of classical pump pulses. We consider scenarios where the pump energies are near the lowest interband transition, and include the lowest conduction $\lambda = c$ and valence $\lambda = v$ bands in SBEs. For quantum heterostructures, we include multiple subbands to describe

the carrier distribution along the growth direction. This is discussed in more detail in Chapter 3. For the analysis of doublet and higher-order correlations, our computation approaches and the approximations vary depending on each specific system, as discussed in Chapters 3 and 5 to 7.

2.4 Local charging in semiconductors

This Thesis primarily focuses on the electronic behavior within semiconductor heterostructures. In these heterostructures, electrons and holes are often spatially separated into distinct regions due to the differences in electronic confinement potential across different materials. This phenomenon appears to challenge our earlier assumption in Sec. 2.3 regarding the homogeneity of the system. To address this, we begin this section with a discussion about Coulomb Hamiltonian in real space and introduce the effects of electron–hole separation.

Figure 2.1 shows a schematic of Coulomb interactions within a semiconductor. The periodic lattice of positively charged ions (white spheres) are surrounded by negatively charged electrons (gray spheres). An electron repels another electron (black arrows), an interaction described by the potential energy V^{e-e}. Similarly, the potential energy for the ion-ion interaction (blue arrows) is denoted in V^{i-i}. An electron is also attracted to an ion (red arrows), described by the potential energy V^{e-i}. As the ionic mass is several orders of magnitude larger than the electron mass, ions are assumed to move slowly while electrons respond instantaneously to the ionic motion, which is known as Born-Oppenheimer approximation [38]. For simplicity, the positive charges from the ions are approximated by a uniform background, referred to as jellium model [2].

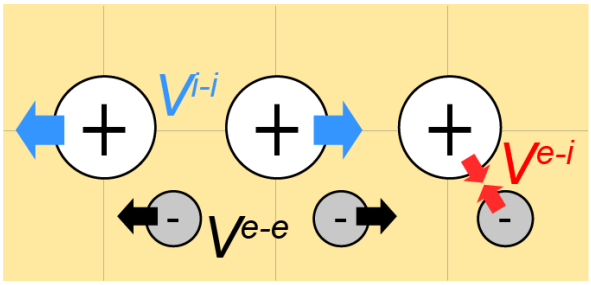


Figure 2.1: Schematic of Coulomb interactions within a semiconductor, including the repulsive interaction between ions (V^{i-i}) and electrons (V^{e-e}), as well as the attractive interaction between electrons and ions (V^{e-i}). The white and gray spheres indicate ions and electrons, respectively.

Denoting $n(\mathbf{r})$ as the ionic density, Coulomb Hamiltonian including both electrons and ions

reads [2]

$$\begin{aligned}\hat{V} &= \hat{V}^{e-e} + \hat{V}^{i-i} + \hat{V}^{e-i} \\ &= \frac{1}{2}\sum_{\nu,\nu'}\int d^3r \int d^3r' \; \hat{\Psi}^\dagger_\nu(\mathbf{r})\hat{\Psi}^\dagger_{\nu'}(\mathbf{r}')V(\mathbf{r},\mathbf{r}')\hat{\Psi}_{\nu'}(\mathbf{r}')\hat{\Psi}_\nu(\mathbf{r}) + \frac{1}{2}\int d^3r \int d^3r' \; n(\mathbf{r})n(\mathbf{r}')V(\mathbf{r},\mathbf{r}') \\ &- \sum_\nu \int d^3r \int d^3r' \; \hat{\Psi}^\dagger_\nu(\mathbf{r})V(\mathbf{r},\mathbf{r}') \; n(\mathbf{r}')\hat{\Psi}_\nu(\mathbf{r}) \; , \end{aligned} \tag{2.11}$$

where $V(\mathbf{r},\mathbf{r}') = \frac{e^2}{4\pi\epsilon_0\epsilon_r|\mathbf{r}-\mathbf{r}'|}$ is the Coulomb energy between two electrons in real space. In general, the expectation value of the product of two Fermionic field operators $\langle\Psi_{\lambda_1}(\mathbf{r}_1)\Psi_{\lambda_2}(\mathbf{r}_2)\rangle$ defines optical polarization for off-diagonal terms $\lambda_1 \neq \lambda_2$ and carrier density for diagonal terms $\lambda_1 = \lambda_2$. On the singlet level, its Heisenberg equation of motion derived from Eq. (2.11) yields [2]

$$\begin{aligned} i\hbar\frac{\partial}{\partial t}\langle\Psi_{\lambda_1}(\mathbf{r}_1)\Psi_{\lambda_2}(\mathbf{r}_2)\rangle|_{HF} = \int d^3r \left[V(\mathbf{r}_2,\mathbf{r}) - V(\mathbf{r}_1,\mathbf{r})\right] \Big(\Delta n(\mathbf{r})\langle\Psi_{\lambda_1}(\mathbf{r}_1)\Psi_{\lambda_2}(\mathbf{r}_2)\rangle \\ - \sum_\nu \langle\Psi^\dagger_{\lambda_1}(\mathbf{r}_1)\Psi_\nu(\mathbf{r})\rangle\langle\Psi^\dagger_\nu(\mathbf{r})\Psi_{\lambda_2}(\mathbf{r}_2)\rangle\Big) \; , \end{aligned} \tag{2.12}$$

$$\Delta n(\mathbf{r}) \equiv \sum_\nu \langle\Psi^\dagger_\nu(\mathbf{r})\Psi_\nu(\mathbf{r})\rangle - n(\mathbf{r}) \; , \tag{2.13}$$

where the total charge distribution in Eq. (2.13) includes all the electronic bands ν and ionic charge distribution $n(\mathbf{r})$. As the contribution from the completely filled valance band is compensated by the ionic contribution, the total charge distribution is defined by the excited electrons and holes [39]

$$\Delta n(\mathbf{r}) = n_e(\mathbf{r}) - n_h(\mathbf{r}) \; , \tag{2.14}$$

where $n_e(\mathbf{r}) = \langle\Psi^\dagger_c(\mathbf{r})\Psi_c(\mathbf{r})\rangle$, $n_h(\mathbf{r}) = \langle\Psi_v(\mathbf{r})\Psi^\dagger_v(\mathbf{r})\rangle$ are the distributions of electrons and holes.

We illustrate charge distributions in a heterostructure formed by two types of materials indicated by green and blue regions in Fig. 2.2. We assume carriers are homogeneously distributed along the in-plane direction, but can be confined in different regions along the growth direction. When electrons and holes are uniformly distributed [Fig. 2.2(a)], charge neutrality is preserved in both regions. In this case, $\Delta n(\mathbf{r}) = 0$ and the first line of Eq. (2.12) does not produce any effects. However, when electrons and holes are separated into different layers [Fig. 2.2(b)], there are excess electrons (holes) in the right (left) layer, and thus the total charge distribution [Eq. (2.13)] does not vanish. This is what we refer to as local charging problem. The charging density $\Delta n(\mathbf{r}) \neq 0$

produces a Hartree potential [39]

$$HT(\mathbf{r}) = \int d^3r' \; \Delta n(\mathbf{r}')V(\mathbf{r}', \mathbf{r}) \; . \tag{2.15}$$

This is also the solution to Poisson equation given total charge distribution $\Delta n(\mathbf{r})$, which describes the mean-field potential experienced by an electron due to the charging density $\Delta n(\mathbf{r})$. The red line in Fig. 2.2(b) shows the Hartree potential in this heterostructure with electrons and holes in the right and left layer, respectively. In this case, the Hartree potential increases (decreases) the potential energy of electrons in the right (left) layer. In principle, the modified confinement potential will also change electronic band energies, wave functions, and interaction matrix elements in SBEs. This approach becomes computationally inefficient as the band structure needs to be computed at each time step. As an alternative, as the field operator can be expanded in any basis [35], we solve SBEs in the original basis where the system is unexcited. Upon the optical excitation of carriers and the local charging that follows from it, the Hartree potential can be self-consistently included via an effective Hamiltonian that couples different states in the initial basis. This approach is discussed in detail in Chapter 3.

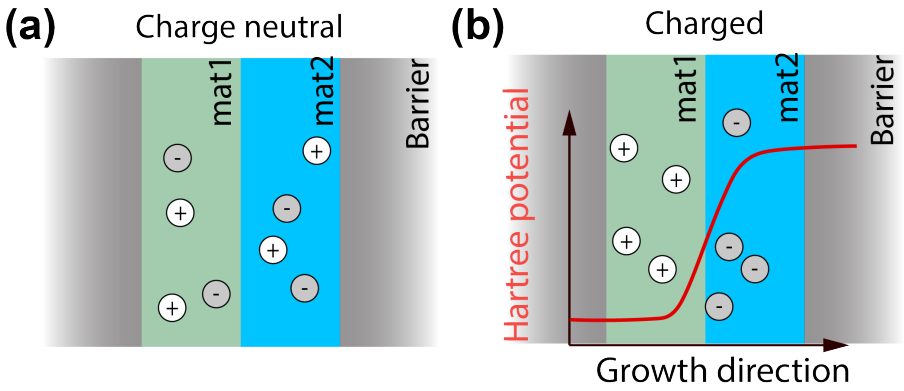


Figure 2.2: Distribution of electrons (gray spheres) and holes (white spheres) in a two-dimensional heterostructure formed by two types of materials indicated by the green and blue regions. (a) With equal distribution of electrons and holes in each material, the system is charge neutral. (b) When electrons and holes are separated into different materials, the system is locally charged, producing a Hartree potential (red line) that changes the energy of electrons along the growth direction.

CHAPTER 3

Unipolar Pulse Generation from Heterostructure Charging Dynamics

3.1 Introduction

The advancement of ultrafast light sources with a few optical cycles is important for nonlinear optics, attosecond physics, and next-generation quantum electronics [22, 40, 41] In the emerging field of lightwave electronics [23], a strong electric bias is used to manipulate electronic states within a subcycle of light pulse. This short time scale of electronic motion holds the potential to beat decoherence challenges in solids. For an effective operation in lightwave electronics, it is desirable to have an electric field that is dominant in a single direction. Such a configuration allows the unidirectional control of electronic states, as it avoids the back-and-forth motion caused by positive and negative cycles. An example for such a field is illustrated in the shaded area in Fig. 3.1, where the electric field consistently points in one direction throughout its duration. This is referred to as a perfect unipolar pulse.

However, based on the general relation in free space [42] that the time integration of electric field vanishes at far field $\int_{-\infty}^{\infty} dt E(t) = 0$, the perfect unipolar pulse cannot propagate at far field. The second best pulse that has the electric field dominant in one direction has an asymmetric shape, shown in the red line in Fig. 3.1. In this scenario, the strength of peak field significantly exceeds that of the dip field. Additionally, the duration of the dip field is longer than that of the peak field so that its time integration vanishes. We define the unipolarity as the ratio between the strength of peak field and that of the dip field

$$\mathrm{uni} = \frac{\mathrm{Peak}}{\mathrm{Dip}} \, . \tag{3.1}$$

In a typical electromagnetic wave with electric field of similar strengths in both positive and negative directions, the unipolarity approaches one. This type of pulse is referred to as a bipolar pulse. On the other hand, unipolar pulses are characterized by a unipolarity value greater than

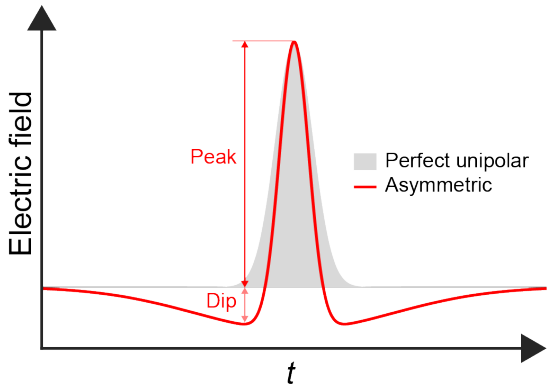


Figure 3.1: **Definition of unipolar pulses.** A perfect unipolar pulse (shaded area) with its electric field in one direction only, compared to an asymmetric pulse (red line) where the magnitude of the peak field is larger than that of dip field.

one. As the n^{th}-order nonlinear response in optical polarization scales to the power of electric field strength $P^{(n)} \propto |E|^n$, in the nonlinear regime ($n > 1$), the peak field in the asymmetric pulse produces dominant effects while the negative dips field can be neglected. Therefore, the asymmetric pulse acts as an effective unipolar pulse in nonlinear optics. Typically, when creating subcycle pulses in terahertz (THz) frequencies, the unipolarity is slightly above one. [43, 44] Recent experiments [45] have aso demonstrated strongly unipolar pulses with unipolarities close to four. These pulses have the great potential to advance lightwave electronics.

The generation of strongly unipolar pulses [45] is based on the spatial dynamics of electrons in quantum-well heterostructures. In a type-II aligned heterostructure shown in Fig. 3.2(a) where the minima of conduction and valance band energies are in different materials, the ground states of electrons and holes are separated along the growth direction. Under the optical excitation resonant at the lowest interband transition (red arrow), electrons are excited from the valance band on the left side (dashed line) to the conduction band on the right side (shaded area). This translation of electrons along the growth direction results in a shift current. Figure. 3.2(b) shows a short burst of shift current during the excitation. As the electric field is proportional to the time-derivative of current $E(t) \propto \frac{dJ}{dt}$, the expected field $E(t)$ is bipolar with a positive half cycle followed by a negative half cycle of the same magnitude [Fig. 3.2(c)]. This bipolar field falls short of our goal of achieving a unipolar pulse.

It is important to note that once the shift current is induced, electrons and holes are inhomogeneously distributed along the growth direction. For the shift current shown in Fig. 3.2(a), there are excess electrons (holes) in the right (left) layer, leading to a disturbance to local charge neutrality shown in Fig. 3.2(d). The separation of electrons and holes creates a charging potential [red line in FIg. 3.2(d)] that increases (decreases) the electronic energy in the right (left) layer.

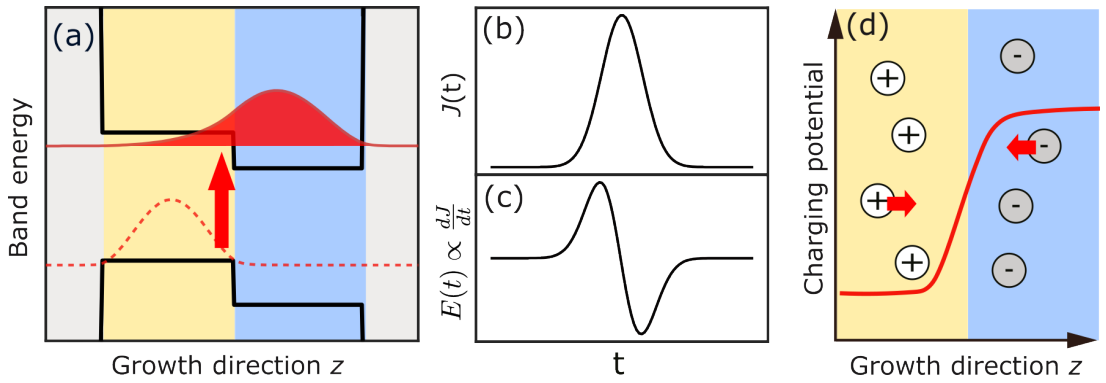


Figure 3.2: **Shift current in a 2D heterostructure.** (a) Optical excitation (red arrow) of electrons from the valence band (dashed line) to the conduction band (shaded area), generating (b) a short burst of shift current $J(t)$ and (c) bipolar electric field. (d) The separation of electrons (gray circles) and holes (white circles) creates a charging potential (red line) that pulls electrons and holes towards the interface.

Also, the charging potential applies a force on charged carriers, causing electrons and holes to move to the interface. During this process, carrier dynamics is affected by a complex interplay of shift current, Coulomb interaction, optical excitation, and relaxation. Therefore, the simple picture of shift current shown in Fig. 3.2 is not enough to describe the actual carrier dynamics, and a systematic description is needed to explore the generation of light pulses in such structures.

Here, we present a self-consistent approach to compute charge-transfer dynamics in semiconductor heterostructures. Our results show that the local charging induced carrier redistribution is significant to alter the shape of the light pulse generated during this process. Specifically, a unipolar pulse is generated when the separated charge carriers accelerate towards the interface to compensate the charging. In addition, we discuss the effects of pump field amplitude, pump field averaging, the thickness of the quantum wells (QWs), and wave function engineering on the shape and peak strength of the unipolar pulse. We compare theory results with experimental data for the unipolar pulses generated from GaAs-type double-QW structures, verifying the peak enhancement with QW thickness. We also discuss strategies to improve the unipolarity beyond the current record realized in experiments. Our findings reveal the fundamental mechanism of unipolar pulse from semiconductor heterostructures and offer guidance for pulse shaping to reach nearly perfect unipolar pulses.

3.2 Theoretical approach

When semiconductor heterostructures are excited, the charge carriers tend to be confined in different regions due to the varying energy landscape among different materials. This results in a local disturbance to charge neutrality, which is typically ignored in the structures with only one type of material. Furthermore, the distribution of charge carriers shifts rapidly when the system is excited by ultrafast light pulses. To describe various effects including the optical excitation and many-body interactions within semiconductors, we develope a self-consistent strategy based on semiconductor Bloch equations (SBEs) [35] to compute carrier dynamics.

3.2.1 Local charging dynamics

To describe the interaction among charge carriers in semiconductors, we start with the general Coulomb Hamiltonian in second quantization [35]

$$\hat{H}_c = \sum_{\nu,\nu'} \frac{1}{2} \int d\mathbf{r} \int d\mathbf{r}' \hat{\Psi}^\dagger_\nu(\mathbf{r}) \hat{\Psi}^\dagger_{\nu'}(\mathbf{r}') V(\mathbf{r},\mathbf{r}') \hat{\Psi}_{\nu'}(\mathbf{r}') \hat{\Psi}_\nu(\mathbf{r}) \ , \tag{3.2}$$

where $\hat{\Psi}^\dagger_\nu(\mathbf{r}), \hat{\Psi}_\nu(\mathbf{r})$ is creation and annihilation operator of electrons at band ν and position $\mathbf{r}$, and $V(\mathbf{r},\mathbf{r}')$ is Coulomb potential in real space. The expectation value $\langle \hat{\Psi}^\dagger_{\lambda_1}(\mathbf{r_1}) \hat{\Psi}_{\lambda_2}(\mathbf{r_2}) \rangle$ defines the optical polarization for off-diagonal terms $\lambda_1 \neq \lambda_2$ and the carrier density for diagonal terms $\lambda_1 = \lambda_2$. On the singlet level, its Heisenberg's equation of motion reads [39]

$$\begin{aligned} i\hbar \frac{\partial}{\partial t} \langle \hat{\Psi}^\dagger_{\lambda_1}(\mathbf{r_1}) \hat{\Psi}_{\lambda_2}(\mathbf{r_2}) \rangle|_{\mathrm{HF}} \ &= \int d^3r \ [V(\mathbf{r_2},\mathbf{r}) - V(\mathbf{r_1},\mathbf{r})] \Big[\textstyle\sum_\nu \langle \hat{\Psi}^\dagger_\nu(\mathbf{r}) \hat{\Psi}_\nu(\mathbf{r}) \rangle \langle \hat{\Psi}^\dagger_{\lambda_1}(\mathbf{r_1}) \hat{\Psi}_{\lambda_2}(\mathbf{r_2}) \rangle \\ &\quad - \textstyle\sum_\nu \langle \hat{\Psi}^\dagger_{\lambda_1}(\mathbf{r_1}) \hat{\Psi}_\nu(\mathbf{r}) \rangle \langle \hat{\Psi}^\dagger_\nu(\mathbf{r}) \hat{\Psi}_{\lambda_2}(\mathbf{r_2}) \rangle \Big] \ . \end{aligned} \tag{3.3}$$

The first line in Eq. (3.3) is the Hartree contribution that is determined by total carrier distribution $n(\mathbf{r}) = \sum_\nu \langle \hat{\Psi}_\nu(\mathbf{r}) \hat{\Psi}_\nu(\mathbf{r}) \rangle$. For a system where positive and negative charges are equally distributed throughout the entire space $n(\mathbf{r}) = 0$, this Hartree contribution is vanishing. In heterostructures however, inhomogeneous carrier distribution can easily occur, leading to a significant Hatree contribution. The second line in Eq. (3.3) is the Fock contribution that describes the exchange energy of electrons.

Here, we extend the discussion from Ref. [39] and present a method to compute charge dynamics self-consistently. Assuming jellium model for the ionic background [2], total carrier density is defined by the electronic density from conduction ($\nu = c$) and valence ($\nu = v$) bands

$$n(\mathbf{r}) = \sum_{\nu=c,v} \sum_{n,n'} \langle \hat{\Psi}^\dagger_{\nu,n}(\mathbf{r}) \Psi_{\nu,n'}(\mathbf{r}) \rangle \ , \tag{3.4}$$

where n is the index for subband state. The completely filled valance band is excluded as it has been included in band energies. [35] For electrons and holes confined in different regions, a local charging density is created $n(\mathbf{r}) \neq 0$ which influences the system dynamics via the first line in Eq. (3.3).

Introducing a Hartree potential via

$$V_{HT}(\mathbf{r}) = \int d^3r' \; n(\mathbf{r}')V(\mathbf{r}', \mathbf{r}) \; , \tag{3.5}$$

the Hartree contribution in Eq. (3.3) can be written into

$$i\hbar\frac{\partial}{\partial t}\langle\hat{\Psi}^\dagger_{\lambda_1}(\mathbf{r_1})\hat{\Psi}_{\lambda_2}(\mathbf{r_2})\rangle|_{\mathrm{HT}} = [V_{HT}(\mathbf{r}_2) - V_{HT}(\mathbf{r}_1)]\,\langle\hat{\Psi}^\dagger_{\lambda_1}(\mathbf{r_1})\hat{\Psi}_{\lambda_2}(\mathbf{r_2})\rangle \; , \tag{3.6}$$

showing its single-particle property clearly. The potential energy defined Eq. (3.5) is also the solution to Poisson's equation. It is the mean-field potential which can lead to the shift in band energies, carrier oscillations, and band mixing. The conventional method [46] to solve this problem if via the iteration of Poisson's equation and Schrödinger equations until a self-consistent solution is found. This can be computationally expensive for dynamic systems or when solving complex band structures. Here, we present a new approach to compute charge-transfer dynamics without repeatedly solving band structures.

It is discussed in Ref. [39] that the Hartree contribution to full dynamics [Eq. (3.6)] can be equivalently obtained via an effective Hartree Hamiltonian

$$H_{\text{eff}} = \sum_\nu \int d^3r \; \Psi^\dagger_\nu(\mathbf{r})V_{HT}(\mathbf{r})\Psi_\nu(\mathbf{r}) \; . \tag{3.7}$$

To convert this Hamiltonian into momentum space, we expand the electronic field operator in the initial, unexcited basis $\hat{\Psi}_\nu(\mathbf{r}) = \sum_{n,\mathbf{k}} a_{\nu,n,\mathbf{k}}\phi_{\nu,n,\mathbf{k}}(\mathbf{r})$ where $a_{\nu,n,\mathbf{k}}$ is electron annihilation operator at band ν, subband n, and crystal momentum $\mathbf{k}$, and $\phi_{\nu,n,\mathbf{k}}(\mathbf{r})$ is electronic wave function for the QW without local charging effects. As the field operator can be expanded in any basis, the excited system can also be described in this basis as long as full states are included. On the confinement level $\phi_{\nu,n,\mathbf{k}}(\mathbf{r}) = \frac{e^{i\mathbf{k}\cdot\mathbf{r}_\parallel}}{\mathcal{L}}\xi_{\nu,n}(z)$ where $\xi_{\nu,n}(z)$ is the envelope function determining the spatial distribution of carriers in the subband n, the effective Hartree Hamiltonian can be written in terms of Hartree matrix elements

$$H_{\text{eff}} = \sum_\nu \sum_{n,n'} \sum_{\mathbf{k}} h^\nu_{n,n'} \; a^\dagger_{\nu,n,\mathbf{k}}a_{\nu',n',\mathbf{k}} \; , \tag{3.8}$$

$$h^\nu_{n,n'} = \int dz \, [\xi_{\nu,n}(z)]^* \, V_{HT}(z)\xi_{\nu,n'}(z) \; , \tag{3.9}$$

where $V_{HT}(z)$ is the Hartree potential defined in Eq. (3.5) along the growth direction. The diagonal elements of Eq. (3.9) describe the shift in subband energy, and off-diagonal terms describe the coupling between subbands in the presence of local charging.

Including light–matter, Coulomb, and phonon interactions, as well as with local charging effects, we solve SBEs [35] for a multi-subband QW heterostructure. The equations of motion for the inter-band polarization $P_{\mathbf{k}}^{v,n;c,n'}$, electronic inter-subband polarization $P_{\mathbf{k}}^{c,n;c,n'}$, and electron density $f_{\mathbf{k}}^{e}$ are

$$\begin{aligned} i\hbar\frac{\partial}{\partial t}P_{\mathbf{k}}^{v,n;c,n'} &= \left(\tilde{E}_{\mathbf{k}}^{e,n'} + \tilde{E}_{\mathbf{k}}^{h,n}\right) P_{\mathbf{k}}^{v,n;c,n'} - (1 - f_{\mathbf{k}}^{e,n'} - f_{\mathbf{k}}^{h,n})\tilde{\Omega}_{\mathbf{k}}^{v,n;c,n'} \\ &\quad - \sum_{\tilde{n}} \left(h_{\tilde{n},n}^{v} P_{\mathbf{k}}^{v,\tilde{n};c,n'} - h_{n',\tilde{n}}^{c} P_{\mathbf{k}}^{v,n;c,\tilde{n}}\right) + \Gamma_{\mathbf{k}}^{v,n;,c,n'} \ , \end{aligned} \tag{3.10}$$

$$i\hbar\frac{\partial}{\partial t}P_{\mathbf{k}}^{c,n;c,n'} = \left(\tilde{E}_{\mathbf{k}}^{e,n'} - \tilde{E}_{\mathbf{k}}^{e,n}\right) P_{\mathbf{k}}^{c,n;,c,n'} - \sum_{\tilde{n}} \left(h_{\tilde{n},n}^{c} P_{\mathbf{k}}^{c,\tilde{n};c,n'} - h_{n',\tilde{n}}^{c} P_{\mathbf{k}}^{c,n;c,\tilde{n}}\right) + \Gamma_{\mathbf{k}}^{c,n;c,n'} \ , \tag{3.11}$$

$$\hbar\frac{\partial}{\partial t}f_{\mathbf{k}}^{e,n} = 2\mathrm{Im}\left[\sum_{\tilde{n}} P_{\mathbf{k}}^{v,\tilde{n};,c,n}\left(\tilde{\Omega}_{\mathbf{k}}^{v,\tilde{n};,c,n}\right)^{*} - \sum_{\tilde{n}} h_{\tilde{n},n}^{c} P_{\mathbf{k}}^{c,\tilde{n};c,n}\right] - i\Gamma_{\mathbf{k}}^{c,n;c,n} \ , \tag{3.12}$$

where $\tilde{E}_{\mathbf{k}}^{\lambda,n}$ is renormalized band energy, $\Omega_{\mathbf{k}}^{v,n;,c,n'} = d_{\mathbf{k}}^{v,n;c,n'}E(t) + \sum_{\mathbf{k}'} V_{\mathbf{k},\mathbf{k}'}^{v,n;c,n'} P_{\mathbf{k}'}^{v,n;c,n'}$ is renormalized Rabi energy, and $V_{\mathbf{k},\mathbf{k}'}^{\lambda,n;\lambda',n'}$ is Coulomb matrix element. The dynamics for inter-subband polarization for valance band $P_{\mathbf{k}}^{v,n;v,n'}$ and hole density $f_{\mathbf{k}}^{h,n}$ are similar to Eq. (3.11) and Eq. (3.12), respectively. The effects of local charging are included via Hartree matrix elements defined in Eq. (3.9).

In Eq. (3.10), the doublet $\Gamma_{\mathbf{k}}^{v,n;c,n'}$ to interband polarization describes excitation-induced dephasing. In our computations in the following, we approximate it via a reduced model $\Gamma_{\mathbf{k}}^{v,n;c,n'} = -i\gamma_{v,n;c,n'}P_{\mathbf{k}}^{v,n;c,n'}$ where the value of the dephasing constant is affected by the carrier densities via

$$\gamma_{v,n;c,n'} = \gamma_0 + \gamma_1 \frac{n_{h,n} + n_{e,n'}}{n_0} \ . \tag{3.13}$$

In Eq. (3.13), γ_0 is background dephasing in the absence of carrier density, γ_1 is a parameter that describes the linear dependence of dephasing on carrier density, n_0 is a fixed density parameter, and $n_{\lambda,n} = \sum_{\mathbf{k}} f_{\mathbf{k}}^{\lambda,n}$ is the carrier density in a single subband n within band λ. The doublet $\Gamma_{\mathbf{k}}^{\lambda,n;\lambda,n'}$ to carrier dynamics in eqs. (3.11) and (3.12) describes carrier relaxation due to phonon interactions. Details for this term are discussed in Sec. 3.2.2.

3.2.2 Carrier relaxation

When excited by strong, ultrashort light pulses, carriers are generated across multiple subbands within the QWs. We assume all carriers relax to the ground state within a relaxation time τ. The coupling between different $\mathbf{k}$ states is ignored. Starting with effective Hartree Hamiltonian in Eq. (3.8), we include subband energies into the diagonal Hartree matrix elements via

$$\tilde{h}^{\nu}_{n,n'} = h^{\nu}_{n,n'} + \delta_{n,n'}\tilde{E}_{\nu,n} \ , \tag{3.14}$$

where $\tilde{E}_{\nu,n} = E_{\nu,n} - \sum_{\mathbf{k}'} V^{\nu,n;\nu,n}_{\mathbf{k},\mathbf{k}'} f^{\nu,n}_{\mathbf{k}'}|_{\mathbf{k}=0}$ is the Fock renomalized band energy with $\mathbf{k}$ dependence approximated by its value at $\mathbf{k} = 0$. Then, we diagonalize the Hartree matrix

$$\tilde{h}^{\lambda}_{n,n'} = \sum_{\beta} u_{\lambda,\beta}(n)\mathcal{E}_{\lambda,\beta} \ [u_{\lambda,\beta}(n')]^* \ , \tag{3.15}$$

where $\mathcal{E}_{\lambda,\beta}$ is eigenvalue of state β in the band λ, and $u_{\lambda,\beta}$ is the corresponding eigenvector. The basis of original subbands $a_{\lambda,n,\mathbf{k}}$ is connected to the eigenbasis $A_{\lambda,\beta,\mathbf{k}}$ via

$$A_{\lambda,\beta,\mathbf{k}} = \sum_{n} [u_{\lambda,\beta}(n)]^* \, a_{\lambda,n,\mathbf{k}} \ , \tag{3.16}$$

$$a_{\lambda,n,\mathbf{k}} = \sum_{\beta} u_{\lambda,\beta}(n) A_{\lambda,\beta,\mathbf{k}} \ , \tag{3.17}$$

such that the Hartree Hamiltonian is diagonal in the new basis

$$\hat{H}_{HT} = \sum_{\lambda}\sum_{n,n'}\sum_{\mathbf{k}} \tilde{h}^{\lambda}_{n,n'} \ a^{\dagger}_{\lambda,n,\mathbf{k}} a_{\lambda,n',\mathbf{k}} = \sum_{\lambda}\sum_{\beta}\sum_{\mathbf{k}} \mathcal{E}_{\lambda,\beta} \ A^{\dagger}_{\lambda,\beta,\mathbf{k}} \ A_{\lambda,\beta,\mathbf{k}} \ . \tag{3.18}$$

Within each band $\lambda = c, v$, we assume carriers relax to the lowest subband $\beta = \beta_0$ in the potential modified by the Hartree potential. The relaxation dynamics in new basis reads

$$\frac{\partial}{\partial t}\langle A^{\dagger}_{\lambda,\beta,\mathbf{k}} A_{\lambda,\beta',\mathbf{k}}\rangle = -\frac{1}{\tau}\left[\langle A^{\dagger}_{\lambda,\beta,\mathbf{k}} A_{\lambda,\beta',\mathbf{k}}\rangle - \delta_{\beta,\beta_0}\delta_{\beta',\beta_0} F_{\lambda,\mathbf{k}}\right] \ , \tag{3.19}$$

where $F_{\lambda,\mathbf{k}} = \sum_n \langle a^{\dagger}_{\lambda,n,\mathbf{k}} a_{\lambda,n,\mathbf{k}}\rangle$ is the total carrier density from all subbands. The total density is conserved during relaxation. Using Equations (3.16) and (3.17), the relaxation dynamics in Eq. (3.19) can be converted to the original basis, yielding

$$\frac{\partial}{\partial t}\langle a^{\dagger}_{\lambda,n,\mathbf{k}} a_{\lambda,n',\mathbf{k}}\rangle|_{\mathrm{rlx}} = -\frac{1}{\tau}\left[\langle a^{\dagger}_{\lambda,n,\mathbf{k}} a_{\lambda,n',\mathbf{k}}\rangle - [u_{\lambda,\beta_0}(n)]^* \, u_{\lambda,\beta_0}(n') F_{\lambda,\mathbf{k}}\right] \ . \tag{3.20}$$

This relaxation contribution is included to in Equations (3.11) and (3.12) via $\Gamma^{\lambda,n;\lambda,n'}_{\mathbf{k}}$ terms.

3.3 Mechanism of unipolar pulses

To explore the carrier dynamics beyond the shift current, we compute for a GaAs-type double-QW structure based on Equations (3.10) to (3.12). The thickness of each QW is 7 nm. The band offset is 90 meV between the conduction bands and 110 meV between the valance bands. The pump pulse is at 50 meV above the lowest 1s-exciton energy, and it has a duration of 130 fs. The excitation-induced dephasing is computed with $\gamma_0 = 40$ meV, $\gamma_1 = 80$ meV, and $n_0 = 3 \times 10^{13}/\text{cm}^2$ in Eq. (3.13). We assume carrier relaxation time $\tau = 0.1$ ps for both electrons and holes. Figure. 3.3(a) shows the spatial distribution (color-coded background) of electrons along the growth direction as a function of time relative to pump center at $t = 0$. The white horizontal line indicates the interface between two QWs. At $t < -400$ fs, more electrons are excited on the positive side than the negative side. The mean positions of electrons (red solid line) and holes (red dashed line) are located on opposite sides with a separation of 5 nm. As the electron density increases, both electrons and holes accelerate towards each other. This process continues until the distance between them is reduced sharply to 2.2 nm at $t = -100$ fs (white vertical line).

To isolate the effects of local charging, we perform an artificial study where the Hartree potential is switched off from full computations. Other conditions are kept the same in this study. Without the Hartree potential, electrons (black solid line) and holes (black dashed line) are separated to two sides without major changes to their positions. Compared to the full results, the reduction of electron–hole separation is primarily due to the presence of Hartree potential. As the carrier density increases initially, the local charging potential also increases. However, this local charging partially balances out when the distance between electrons and holes is reduced. This balancing occurs when Hartree potential is self-consistently included.

We compute total polarization along the growth z direction of the heterostructure

$$P = -|e| \int d^3r \Psi^\dagger(\mathbf{r}) z \Psi(\mathbf{r}) = -|e| \sum_\nu \sum_{n,n'} \sum_{\mathbf{k}} P_{\mathbf{k}}^{\nu,n;\nu,n'} z_{n,n'}^\nu \ , \tag{3.21}$$

where $z_{n,n'}^\nu = \int dz \left[\xi_{\nu,n}(z)\right]^* z \ \xi_{\nu,n'}(z)$ is the subband dipole along z direction. The shift current and electric field are computed from $J(t) = \frac{\partial}{\partial t} P$ and $E(t) = \frac{\partial^2}{\partial t^2} P$, respectively. Figure 3.3(b) compares normalized current $J(t)$ from full results (red line) with that computed without Hartree potential (black line). Without Hartree potential, the current $J(t)$ shows a single peak near $t = 0$. Including Hartree potential changes the shape of current and electric field significantly. Instead of a unidirectional current, $J(t)$ increases initially but reverses its direction at $t = -100$ fs. Figure 3.3(c) shows the corresponding electric fields, normalized to have peak field along the positive direction. The shaded area indicates the envelope of pump field. As expected, a bipolar field (black line) is generated without Hartree contribution. Including Hartree potential results in

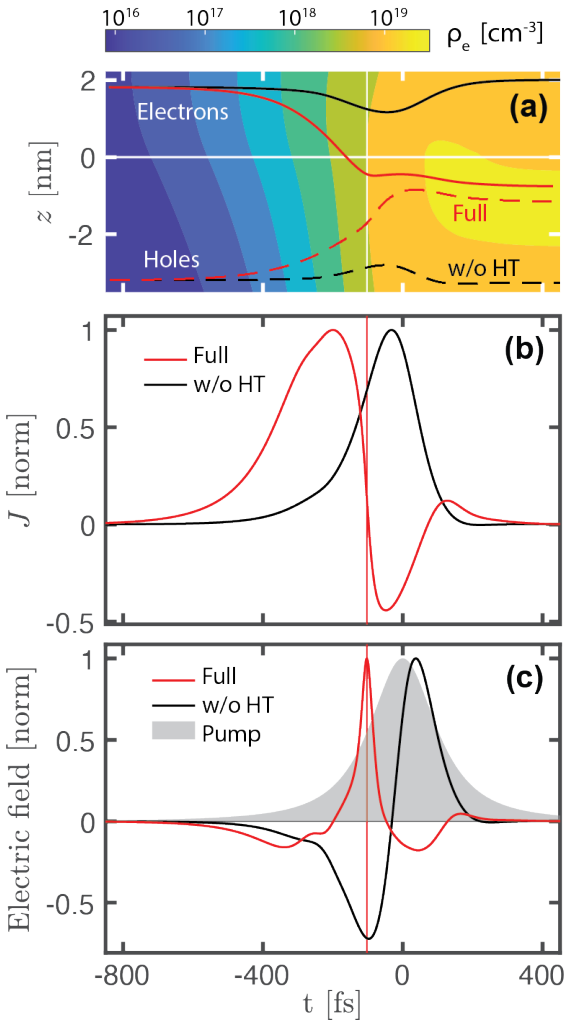


Figure 3.3: **Mechanism of unipolar pulses**. (a) Mean positions of electrons (red solid line) and holes (red dashed line) from full results, compared to electron (black solid line) and hole (black dashed line) positions when Hartree potential is switched off. The color-coded background depicts spatial distribution of electron density from full results. (b) Shift current $J(t)$ and (c) electric field from full results (red) and results obtained without Hartree potential (black). The envelope of pump field is indicated by shaded area. All quantities are normalized to have peak field along positive direction. The vertical lines indicate peak time of electric field from full computations.

a unipolar pulse (red line), characterized by unipolarity values of uni=6.3 and uni=5.6, computed from the dips before and after the highest peak, respectively.

The peak field of the unipolar pulse occurs near the time when the shift current changes its direction [red vertical lines in Fig. 3.3(b-c)]. It is also synchronized with the switching to charge neutrality as electron–hole separation is reduced sharply at $t = -100$ fs [white vertical line Fig. 3.3(a)]. The reduction of charge separation together with a reversed current compensates local charging in each layer and relaxes the system towards charge neutrality. Comparing full

results with those obtained without Hartree potential, the switching from local charging to charge neutrality is only found when Hartree potential is included. Therefore, we conclude that local charging induced carrier redistribution towards charge neutrality is mechanism of unipolar pulse generation.

3.4 Control of unipolar pulses

The mechanism of unipolar pulses discussed in Sec. 3.3 gives insight into the control of experimental conditions for enhanced pulse shaping. In this section, we discuss different aspects, ranging from the pump configuration to the engineering of QW structures, that can influence the shape and amplitude of the emitted field. We compare experimental and theoretical predictions for unipolar pulses generated from QWs of different thicknesses. In addition, we explore strategies in wave function engineering aimed at increasing unipolarities further. Furthermore, we examine the potential for scaling up the peak field strength, a key aspect for using such light sources to control electronic states in solids. These factors provide important guidance to create ultrashort unipolar pulses in the future.

3.4.1 Effect of pump field strength

It is shown in Sec. 3.3 that the carrier redistribution in the presence of local charging is an essential factor for realizing unipolar pulses. As the magnitude of the charging potential is determined by carrier densities, we expect the emitted electric field is affected by the strength of pump field. To analyze this effect, we compute for a double-QW structure that is excited with pump fields of varying strengths. Figure. 3.4(a) shows the THz fields generated under excitations of different field strengths. The pump field strength, denoted E_{pump}, is expressed in arbitrary unit here. The shaded area indicates the envelope of the pump field. At weak field $E_{\mathrm{pump}} = 0.5$ (black dashed line), the THz transient is bipolar with a negative dip followed by a positive peak. As pump field increases to $E_{\mathrm{pump}} = 1.0$ (red line), the magnitude of the dip before main peak is reduced. At the same time, a second dip starts to emerge after the main peak. Further increasing the pump strength to $E_{\mathrm{pump}} = 2.0$ produces a unipolar pulse with both dips of similar sizes. This indicates that the unipolar pulse is only produced when the pump field strength reaches a threshold. We define the onset of unipolar pulse to be the emergence of a second dip following the main peak, and define the threshold pump field strength, denoted as E_{uni}, to be the lowest pump field at which the second dip appears.

Figure 3.4(b) shows the maximal charging potential along the growth direction according to the pump strengths shown in Fig. 3.4(a). For all pump strengths, the magnitude of the charging

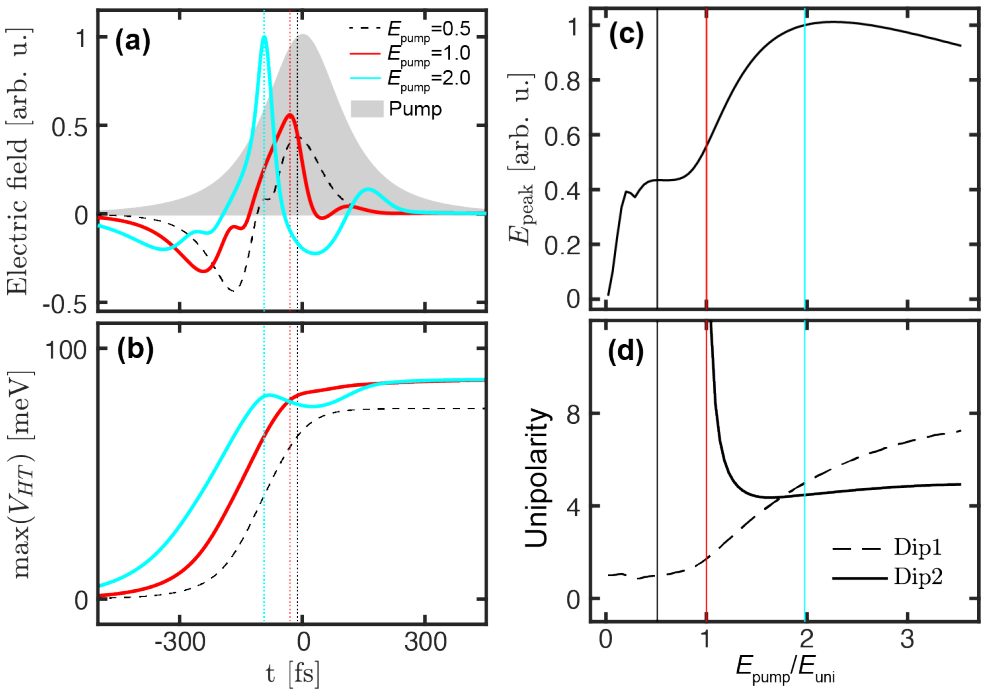


Figure 3.4: **Pump field strength dependence of THz transients.** (a) THz transients and (b) the maximal Hartree potential along the growth direction for different pump strengths (in arbitrary units) $E_{\text{pump}} = 0.5$ (black dashed line), $E_{\text{pump}} = 1.0$ (red line), and $E_{\text{pump}} = 2.0$ (cyan line). The peak fields are indicated by vertical dotted lines. The shaded area indicates envelope of pump field. (c) Peak field in THz transients and (d) unipolarity computed from dip1 before main peak (dashed line) and dip2 after main peak (solid line) as function of the ratio of pump strength to unipolarity threshold.

potential increases for $t < -100$ fs, with a faster increase rate for higher pump field strengths. This corresponds to the initial excitation where electrons and holes are generated to opposite sides of the double QWs. As the time approaches $t = -100$ fs, the potential reaches a saturation at 80 meV for the strongest excitation ($E_{\text{pump}} = 2.0$). The saturation at similar level is also reached for the pump field $E_{\text{pump}} = 1.0$ at a later time. This potential level is close to the initial band offsets between two QWs. For the weakest excitation ($E_{\text{pump}} = 0.5$), the saturation level of the charging potential is slightly lower than those obtained at higher pump strengths. Also, it is observed that the saturation in potential occurs at the same time when THz transient reaches its peak field, as indicated by vertical dotted lines.

Figure. 3.4(c) shows the strength of THz peak field as a function of the ratio between pump field strength and the unipolar threshold $E_{\text{pump}}/E_{\text{uni}}$. The vertical lines indicate the selected pump strengths plotted in Fig. 3.4(a-b). Starting from weak excitations, the peak field E_{peak} of THz transient increases linearly and reaches a saturation before the unipolar threshold. At

$E_{\text{pump}}/E_{uni} = 1$, the peak field starts to increase again before reaching a second saturation near $E_{\text{pump}}/E_{\text{uni}} = 2$. It is discussed above the peak field is signified when the charging potential reaches a level near the initial band offset. When charging potential reaches this threshold, massive carrier redistribution occurs to compensate the charging. Thus, the saturation in THz peak field is limited by the finite number of carriers to reach the threshold in charging potential.

Figure 3.4(d) shows unipolarity computed from the dip before (dip1, dashed line) and after (dip2, solid line) the THz peak. Below the unipolar threshold $E_{\text{pump}}/E_{\text{uni}} < 1$, there is only one dip before the main peak with a unipolarity close to one. For $E_{\text{pump}}/E_{\text{uni}}$ slightly above one, the unipolarity for dip1 increases with pump field strength. At the same time, the unipolarity for dip2 drops from near infinity when the second dip just starts to form. The unipolarities from both dips become similar at elevated pump strengths, indicating the stability of THz pulse shape under strong excitations. Therefore, the shape and peak field strengths of the THz transients are strongly affected by the strength of the pump field at $E_{\text{pump}} < E_{\text{uni}}$. For higher excitation levels, the shape and peak field are stable with pump field strengths.

3.4.2 Effect of pump field averaging

In Sec. 3.4.1 we consider the excitation of QWs using a pump field set to a specific peak strength. It is important to note that in actual experiments, the pump beam typically has a finite spot size, where the field strength varies across the beam spot. This spatial distribution in pump field in turn affects the THz emission. This is because different areas within the beam spot are excited by varying field strengths, leading to different excitation levels. Thus, to compute the THz field collected from the finite pump spot, we need to average the emission field from various positions. To better understand how this averaging changes with pump profiles, we compute THz field for both Gaussian and parabolic pump profiles.

Figure 3.5(a) shows the spatial distribution of Gaussian (shaded area) and parabolic (red solid line) pump profiles. The field strength as a function of position in Gaussian beam is $E(r) = E_0\, e^{-\frac{r^2}{\sigma^2}}$ where r is the distance from the center of pump spot, σ is the width of the beam, and E_0 is peak field at the center of pump spot. The parabolic beam has $E(r) = E_0\left[1-\left(\frac{r}{L}\right)^2\right]$ where L is radius of pump spot. We denote $E_{THz}(r,t)$ as the emitted THz field at position r within the pump spot. Considering the finite size of pump beam, the averaged THz field is computed from

$$E_{THz}^{avg}(t) = 2\pi \int_0^{r_{max}} dr\; r E_{THz}(r,t) \Rightarrow \int_{E_c}^{E_0} dE\; f(E)\; E_{THz}(E,t)\;, \tag{3.22}$$

where the integral over position is converted to the integral over pump field strength E in the second step. The weight at each pump field, denoted as $f(E)$, is determined by the pump pro-

file. The integration range is limited to the central area with $r < r_{\max}$. We introduce a cutoff field strength, denoted as E_c, as the field amplitude at $r = r_{\max}$. The horizontal dashed lines in Fig. 3.5(a) shows the selected cutoff field $E_c = 0.25E_0$ (black dashed line) and $E_c = 0.50E_0$ (red dashed line) that we use in the following.

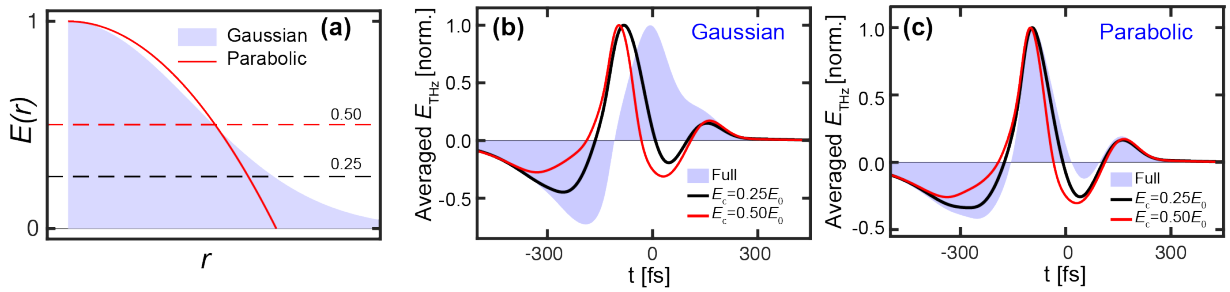


Figure 3.5: **Effect of pump field averaging on the shape of THz transients.** (a) The spatial distribution of field strength for Gaussian (shaded area) and parabolic (red solid line) profiles. The dashed horizontal lines indicate cutoff in field strengths used in averaging. Normalized THz field for (b) Gaussian and (c) parabolic beam profiles averaged over full area (shaded area), and with cutoff in field strength at $E_c = 0.25E_0$ (black lines) and $E_c = 0.50E_0$ (red lines).

We choose peak field at the center of the beam spot to be significantly above the unipolar threshold $E_0 = 2.6\ E_{\text{uni}}$. The averaged THz field is computed from the full area and from the central area with field strength above the cutoff $E_c = 0.25E_0$ and $E_c = 0.50E_0$. For Gaussian pump profile [Fig. 3.5(b)], including full spot size (shaded area) produces a bipolar field even though the peak field $E_0 = 2.6E_{uni}$ is above the unipolar threshold. With a cutoff field strength $E_c = 0.25E_0$ (black line), the averaged E_{THz} becomes unipolar, with the magnitude of the first dip larger than that of the second dip. The dips on two sides become more symmetric for a higher cutoff field $E_c = 0.50E_0$ (red line).

For parabolic pump profile [Fig. 3.5(c)], a unipolar field is produced when the entire spot area is included (shaded area). This is due to the faster decay of pump field with position compared to that in Gaussian beam. In this case, the bipolar emission contributions from the weak excitation area near the edge of the pump spot are reduced. Including cutoff field strengths reduces (increases) the size of the first (second) dip, which is similar to the results obtained from Gaussian beam. For the highest cutoff field $E_c = 0.50E_0$, the averaged THz transients from Gaussian and parabolic pump profiles show similar pulse shapes. This is expected as these two pump profiles in the range of $E > 0.5E_0$ have only minor differences, as is compared in Fig. 3.5(a).

Thus, the pump profile affects the shape of the averaged THz transient. For a Gaussian beam, the averaged THz field from the full pump spot can be bipolar even when the peak field at the center of the spot exceeds the unipolar threshold. When areas of weak excitations near the edge

of the beam spot are neglected, the averaged field becomes unipolar. In the case of a parabolic beam, the contribution from beam edge is lower as the pump field decays faster towards the edge, allowing for a unipolar field even when the entire spot is included. In addition, in both pump profiles analyzed here, two dips in the unipolar pulses become more similar in sizes as the cutoff field is increased.

3.4.3 Effect of QW thickness

In Sec. 3.3, we showed that the peak field of the unipolar pulse is reached when the charging-to-charge-neutral switching occurs. This carrier motion is affected by the initial carrier separation which is turn determined by the thicknesses of QWs. Therefore, we expect that the thickness of the QWs can have an impact on the peak field strength. Here, we compute for different double-QW structures where the left QW has a fixed thickness of $L_1 = 7$ nm and the right layer has an adjustable thickness L_2. Figure 3.6(a) depicts the valance band energy and wave function $|\psi|^2$ for the first few hole subbands in the 7nm/7nm QW structure. The wave functions for the first state on the left and on the right are highlighted in red lines. The mean positions for these two states, denoted as $z_{L(R)}$, are indicated by the vertical dashed lines, with their distance denoted in $d_{L,R} = z_R - z_L$. As the thickness of the right layer L_2 is adjusted, we compute subband wave functions and $d_{L,R}$ accordingly. The black line in Fig. 3.6(b) shows $d_{L,R}$ increases linearly with L_2. This is expected as a larger L_2 shifts the mean position of the first state on the right side further away from the ground state on the left.

We computed THz field emitted from QWs structures of varying L_2 under the same excitation conditions. Figure 3.6(b) shows that the peak field in THz transient increases with L_2. The corresponding carrier dynamics and THz transients are plotted in Fig. 3.6 (c-d) for L_2 =3.5 nm (black lines), 5.5 nm (blue lines), and 7.0 nm (red lines). The shaded area indicates the envelope of the pump field, and the vertical lines indicate the peaks of THz transients. As L_2 increases, the initial separation between electron and hole increases. This leads to a larger displacement during the switching towards charge neutrality and thus enhanced THz peak field. The more pronounced displacement in holes for larger L_2 is connected to the larger $d_{L,R}$ shown in Fig. 3.6(b). As the optically excited holes on the left side move to the right side, the maximal distance it can travel is determined by the separation between left and right states $d_{L,R}$. Therefore, a larger $d_{L,R}$ as L_2 increases leads to an increase in the displacement of holes. The acceleration of carriers towards charge neutrality is also faster for larger L_2, leading to an increased THz peak field. The amplitude of THz peak field doubles for $L_2 = 7.0$ nm compared to that from the structure with $L_2 = 3.5$ nm.

Experiments are conducted on two samples with QW thicknesses of 7.0 nm/7.0 nm and

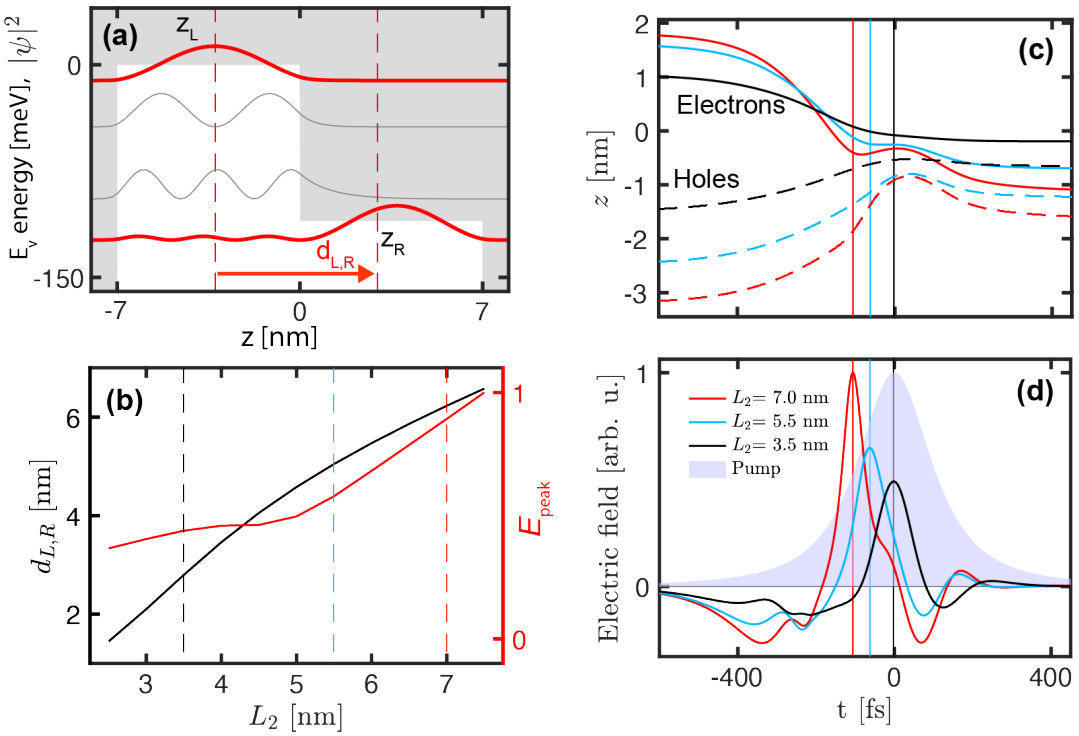


Figure 3.6: **Enhancement of peak field strength with QW thicknesses.** (a) The first few states in the valance band of 7nm/7nm double QWs. The vertical dashed lines indicate mean positions of the first state on left (z_L) and right (z_R) side. (b) Distance between left and right states $d_{L,R}$ (black line, on the left axis) and THz peak field (red line, on the right axis) as function of L_2. (c) Mean positions of electrons (solid lines) and holes (dashed lines), and (d) corresponding electric field for the QWs with right-layer thickness $L_2 = 3.5$ nm (black lines), $L_2 = 5.5$ nm (blue lines), and $L_2 = 7.0$ nm (red lines). The vertical lines mark the moments when the fields reach their peak strengths. The shaded area indicate pump-field envelope.

7.0 nm/3.5 nm, respectively. The QWs consist of $GaAs_{0.9}Sb_{0.1}$ in the left layer and $In_{0.14}Ga_{0.86}As$ in the right layer. To enhance the emission, a total of 100 double-QWs are stacked. The pump pulse used in the experiment has a duration of 130 fs with central energy of 1.2 eV and pump fluence 1 mJ/cm^2. Under identical excitation conditions, the THz fields emitted from both samples are shown in Fig. 3.7(a). The THz fields are shifted to their peak times t_{peak}. The peak field increases from 0.28 kV/cm in the 7.0 nm/3.5 nm QWs (black line) to 0.49 kV/cm in the 7.0 nm/7.0 nm QWs. The thicker structure also sees a broadening in the main peak.

Theory results for the same structures are shown in Fig. 3.7(b-c). We include the lowest four valance subbands and three conduction subbands. Same excitation conditions are applied to both QWs for the comparison of THz transients. Without field averaging [Fig. 3.7(b)], the thicker structure (7.0nm/7.0nm, red line) has the peak field strength doubled compared to that from the thinner structure (7.0nm/3.5nm, black line). There is also a noticeable shoulder peak at $t - t_{peak} =$

90 fs in the thicker structure. This shoulder peak is produced when the back and forth motion of charge carriers occurs, as is shown in Fig. 3.6(c-d). The enhancement in peak field and broadening due to the shoulder peak agree with experimental results.

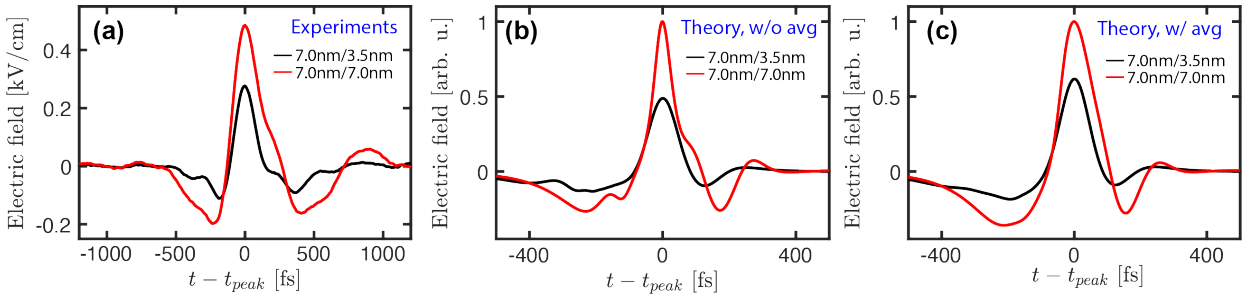


Figure 3.7: **Experiment–theory comparison of peak field enhancements via QW thicknesses.** (a) Experimental measurements of THz field from QWs of thicknesses 7.0 nm/3.5 nm (black line) and 7.0 nm/7.0 nm (red line) on the left/right side. (b-c) Theory predictions of electric field for the corresponding structures without (b) and with (c) pump field averaging.

We also compute the averaged THz transients for two structures. We assume a parabolic pump profile and include central area of the beam spot with $r_{\max} = 0.8L$ according to Eq. (3.22). The peak field at the center of the beam spot is the same for both QWs. Figure. 3.7(c) shows the peak field in the 7.0nm/3.5nm QWs (black line) reaches 60% of peak field in the 7.0nm/7.0nm QWs (red line). The width of the main peak is also larger for $L_2 = 7$ nm, as a result of the shoulder peak observed in unaveraged THz transients in Fig. 3.7(b). Overall, the increased peak field amplitude and temporal width in the thicker structure agree with experimental measurements. The comparison between experiment and theory verifies the enhancement in THz peak field via QW thickness.

3.4.4 Towards super unipolarity

The current record of unipolarity that has been realized in experiments [45] is close to four. To explore the possibility of increasing unipolarity towards $\mathrm{uni} > 10$, we engineer subband wave functions with a goal to enhance carrier motion further. Figure 3.8(a) shows schematics of three structures where the black solid line indicates valence-band energy in the double QWs. From the top frame to bottom frame, the position of the interface between two QWs is shifted to the left side so that the mean positions of wave functions $|\psi|^2$ relative to the interface are also changed. We denote each structure with the mean position of each subband state - the first structure being LLLR due to the first three hole states centered on the left (orange shaded area) and the fourth state on the right (blue shaded area). As the interface is shifted to the left, the number of states in

right layer is increased to two in the second structure (LLRR) and increased to three in the third structure (LRRR).

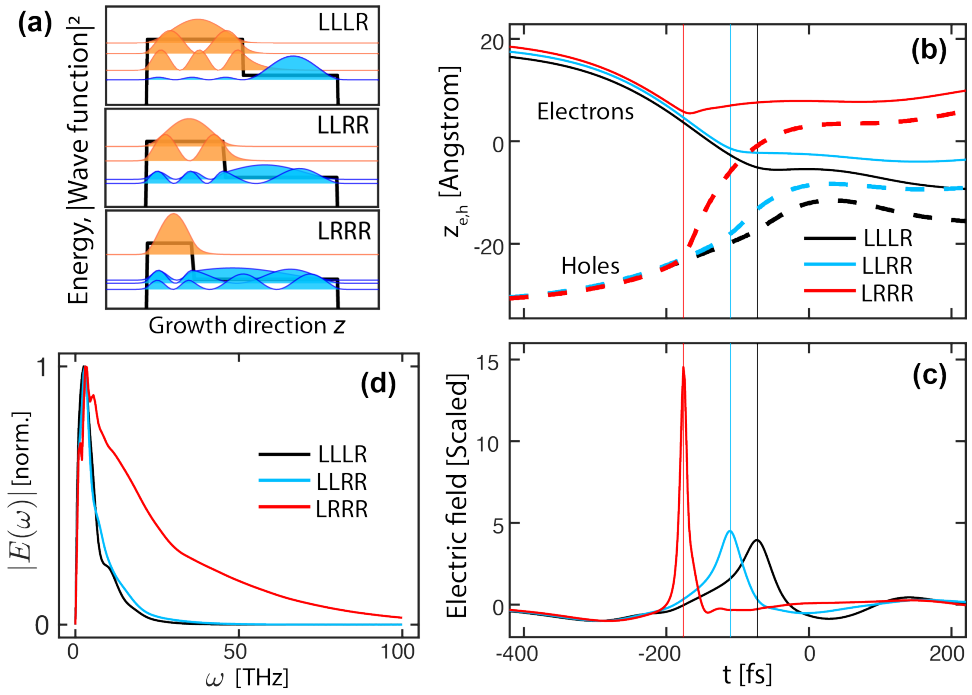


Figure 3.8: **Super unipolarity via engineering the number of states on two sides of the double-QW interface.** (a) The first few hole subband states in double-QW structures. The letter indicates the mean position of each state on the left (L) or the right (R) side of the interface starting with the state with the highest valance-band energy. (b) Mean positions of electrons (solid lines) and holes (dashed lines) and (c) corresponding electric field from three structures shown in (a) with unipolarity of uni=4 (LLLR), uni=5 (LLRR), and uni=15 (LRRR). The electric field in (c) is scaled to have same magnitude at the first dip near $t = -290$ fs. (d) Normalized THz emission spectra.

We compute THz fields from three structures under the same excitation condition. Figure 3.8(b) shows mean positions of electrons and holes as a function of the time relative to the pump center at $t = 0$. The electrons (solid lines) and holes (dashed lines) initially move from two sides separated by about 50Å. The major shifts in carrier positions start at $t = -200$ fs. Compared to the LLLR and LLRR structures, a dramatic increase in the displacement of hole is observed in the LRRR structure. The average position of holes changes from $z = -22$ Å to $z = 3$ Å within 150 fs. This rapid carrier redistribution can be understood from the characteristics of their wave functions shown in Fig. 3.8(a). Under resonant excitation of ground state, the majority of carriers are excited to the ground state on the left. As excitation level increases, carriers from ground state on the left side tend to move to the right side to balance charging. Due to the smallest en-

ergy separation between the first excited state relative to the ground state, the coupling between these two states is most significant among all states. For the LLLR and LLRR structures, both the ground state and the first excited state are centered on the left - the carrier redistribution resulting from such coupling is also redistricted to the left layer. This scenario changes for LRRR structure where the first excited state is located on the right, leading to an extensive separation from the ground state. The dominant left-right coupling between the lowest two states moves carriers dramatically.

The corresponding electric fields from three structures are shown in Fig. 3.8(c), with vertical lines indicating the times for reaching THz peaks. The field amplitude is scaled to have the first dip (near $t = -290$ fs) to have the same magnitude. The unipolarity is increased from uni=4 in the LLLR structure (black line) to uni=15 in the LRRR structure (red line). The spectrum of THz emission field [Fig. 3.8(d)] peaks at $\omega = 2.6,\ 2.8,\ 3.2$ THz for LLLR (black line), LLRR (blue line), and LRRR (red line), respectively. In addition, the spectral width at half maximum increases from 5 THz to 20 THz with a larger number of states on the right. Therefore, increasing the number of states opposite the ground state enhances carrier displacement and the unipolarity of the THz field. Specifically, for the structure (LRRR) with the maximum number of excited states positioned on the opposite side of the ground state, we predict a super unipolarity of uni=15 along with a spectral width of 20 THz.

3.4.5 Scalability of peak field

In addition to the ability to adjust the unipolarity and spectral width of the THz field, the capability to scale the peak field strength is a crucial aspect for the practical use of unipolar sources. We compare three structures shown in Fig. 3.8(a) in terms of the emitted THz field strength as a function of pump field strength. Figure 3.9(a) shows the peak field as a function of the ratio between pump strength and unipolar threshold E/E_{uni} for the LLLR (black line), LLRR (blue line), and LRRR (red line) structures. The peak field in each case is normalized with respect to the maximum peak field it reaches as the pump field increases. At $E < E_{\text{uni}}$ where bipolar field is emitted, the peak of THz transient increases with pump strength E/E_{uni} before reaching a saturation. Above the unipolar threshold ($E/E_{uni} = 1$), the peak field increases about linearly with pump strength. This increase continues until it reaches a second plateau when the pump strengths exceeds twice the unipolar threshold $E/E_{uni} > 2$. For the super unipolar structure (LRRR), the range of peak field in the unipolar regime reaches 9 times that of the bipolar regime. This unipolar range is significantly larger than those from the LLLR and LLRR structures.

Figure 3.9(b) shows the unipolarities computed from the first (solid lines) and the second (dashed lines) dips in THz transients. Lines colored in black, red, and cyan represent the emis-

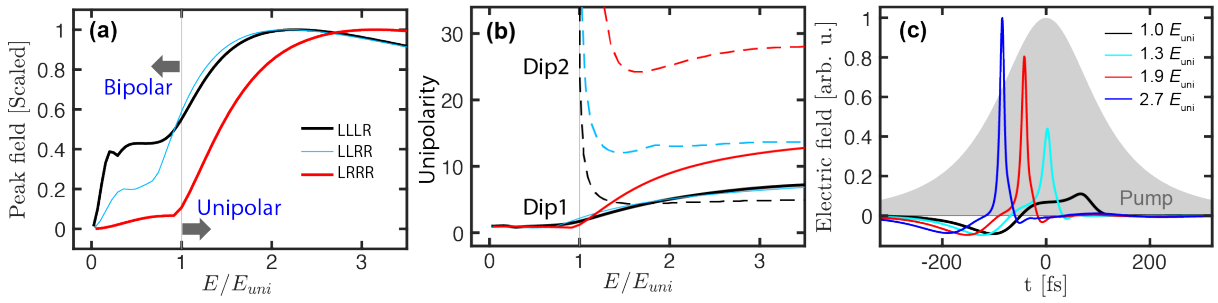


Figure 3.9: **Peak field scalability.** (a) Peak field of THz transients as function of the ratio between pump field strength and unipolar threshold E/E_{uni} for the LLLR (black line), LLRR (blue line), and LRRR (red line) structures. (b) Unipolarity computed from the dip before main peak (Dip1) and the dip after main peak (Dip2). The black, blue, and red solid (dashed) lines represent electrons (holes) in the LLLR, LLRR, and LRRR strucures. (c) THz field at selected pump field strengths $E = E_{uni}$ (black line), $E = 1.3\ E_{uni}$ (cyan line), $E = 1.9\ E_{uni}$ (red line), and $E = 2.7\ E_{uni}$ (blue line) for the LRRR structure. The envelope of pump field in indicated by shaded area.

sion from LLLR, LLRR, and LRRR structures, respectively. For $E/E_{uni} < 1$, there is only a sinlge dip with unipolarity close to one. The unipolarity for dip1 increases for $E > E_{uni}$ in all three structures. The largest enhancement is observed in the LRRR structure (red solid line) reaching uni> 10 for $E/E_{uni} > 2.3$. The unipolarity computed from the second dip is also significantly greater in the LRRR structure than those from the other structures, consistently maintaining uni> 24 in the entire range of pump field strength.

Figure 3.9(c) shows temporal traces of THz transients for the LRRR structure at selected pump field strengths. The envelope of pump field is indicated by shaded area. At the threshold field for unipolar pulse $E = E_{uni}$, the THz field (black line) is almost bipolar but starts to develop a shallow dip after the positive peak. Increasing the pump strength sees a dramatic increase in the THz peak field. Specifically, the peak field is ten times increased at the pump field $E = 2.7\ E_{uni}$ compared to that from the pump field equal the unipolar threshold $E = E_{uni}$. At $E = 2.7\ E_{uni}$, the unipolarity reaches uni=11 and uni=27 for the first and second dip, respectively.

Our results show that the peak field of THz transient can be controlled by adjusting the strength of pump field. We observed that as the number of excited states centered on the opposite side of the ground state increases, the range of peak field in the unipolar regime also increases. Specifically, in the case of the LRRR structure, the range of the uniplar field reaches nine times larger than that in the bipolar regime. The unipolarity maintains consistently above ten for the strength of pump field in the range $E_{\mathrm{pump}}/E_{\mathrm{uni}} > 2.3$. The extensive range of the unipolar peak field and the consistent unipolar shape highlight the potential of LRRR structure as a scalable unipolar source.

3.5 Conclusion

In conclusion, we presented a self-consistent method to compute charge carrier dynamics in semiconductor heterostructures. While the simple picture of shift current results in a bipolar field only, the pulse shape is significantly altered when local charging effects are included. Our analysis shows that following the initial separation of electrons and holes, rapid charge redistribution occurs as the local charging potential increases. As a result, electrons and holes accelerate towards the interface with a sharp reduction in their distance. This switching from local charging to charge neutrality produces a unipolar pulse that is distinct from the bipolar pulse expected without charging effects. Therefore, we identified the local charging dynamics as the mechanism of unipolar pulse generation.

We also discussed different factors that affect the peak field strength and the shape of the unipolar pulses, including pump field strength, pump field averaging, and wave function engineering within the QWs. Experiment–theory comparison of the unipolar pulses generated from QWs of different thicknesses verifies the peak field enhancement with QW thickness. Further improvements in the unipolarity of THz pulses were discussed. We found that by maximizing the number of states on the opposite side to the ground state, super unipolar pulses with unipolarity approaching uni=15 can be realized. The optimal structure also exhibits an extensive range in field strength that can be scaled with pump field strength while maintaining consistent unipolar shape. Our theoretical predictions for super unipolar pulses indicate a need for experimental validation of enhanced unipolarity via QW structures engineering. The prospect of achieving nearly perfect unipolar pulses shows significant potential for advancing lightwave electronics, offering precise control over electronics states.

CHAPTER 4

Terahertz Switching in III-nitride Ferroelectrics

4.1 Introduction

In ferroelectric materials, the relative displacement between positive and negative ions creates an electric polarization in the absence of an electric field. The direction of the polarization can be reversed by applying an external field. Ferroelectrics are typically characterized by the hysteresis loop in their polarization and electric fields, a key property allowing them to be used for memory devices [47]. The most common materials that exhibit ferroelectric properties are perovskite structures [48]. In recent years, III-nitrides with the incorporation of Scandium or Boron atoms have been found as a new class of ferroelectric materials, with the switchable polarization along c direction of the wurtzite structure. [17, 49, 50] Nitride ferroelectrics offer advantages of high stability, large polarization, and distinct nonlinear properties [51]. Theory investigations on ferroelectric materials have largely been focused on their structural parameters [17, 50]. Yet, there is a lack of insight into the dynamic mechanism that govern the switching behaviors.

There is a wide range of time scales reported for ferroelectric polarization switching, ranging from sub-picoseconds to nanoseconds [52–55]. The dynamics of switching has been found to be affected by defects [56], the strength and frequency of electric fields [52, 57], excitation of phonons [53], and manipulation of lattice structures via light fields [54]. Understanding the natural switching time determined by the intrinsic materials properties such as the ionic potential and mass is important to guide the functional design of ferroelectrics. In addition, achieving systematic control of polarization switching via lightwave opens possibilities for high-speed electronics. To analyze the atomic response of ferroelectrics to lightwave, a microscopic theory for the ferroelectric polarization switching is essential.

Here, we present a quantum theory including many-body Coulomb and phonon interactions to describe the ionic motion during the polarization switching in ferroelectrics. We highlight the importance of local charging effects that govern the fundamental switching behaviors. The natural switching time is analyzed under a quasi-static electric field, where the switching process

is identified via a three-step model. In addition, we explored the manipulation of ionic motion via terahertz (THz) fields. The ultrafast switching on the sub-picosecond time scale is revealed, during which process strong high-harmonic generation is predicted. We also present preliminary experimental-theory comparison for picosecond switching time in ScAlN ferroelectric materials. Our findings demonstrate the possibility for using THz fields to control the switching in III-nitride ferroelectrics, as a potential route to ferroelectric THz memories.

4.2 Many-body aspects of ionic latching

In ferroelectric materials, the ionic potential adopts a double-well like profile $U_{DW}(z)$ with two valleys symmetric around the center. Figure 4.1(a) shows a schematic of the confinement potential (gray area) along z direction. The valley positions $\pm z_0$ are indicated by vertical lines, which correspond to opposite polarizations when the ion is displaced to different sides. However, the ground state has ionic density equally distributed on two sides (blue line). As a result, there is no preferred site for the ionic position and thus polarization switching is not expected to occur.

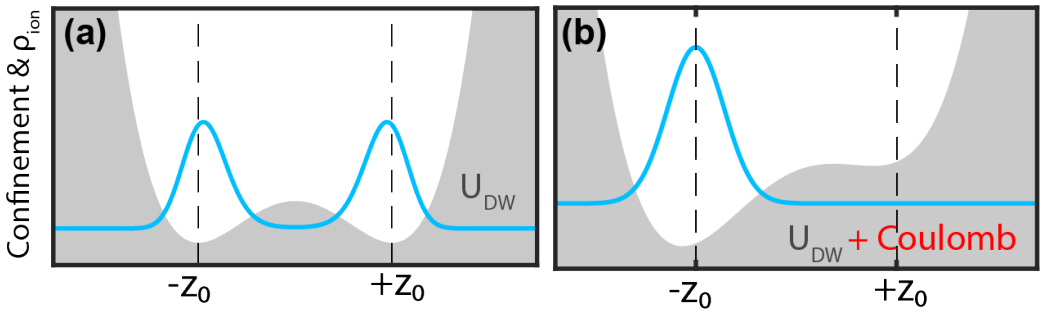


Figure 4.1: **Coulomb effects on ionic potential and distribution.** (a) A double-well potential U_{DW} (shaded area) with two valleys at $z = \pm z_0$. The ionic density (blue line) is symmetrical on two sides, resulting in a vanishing polarization. (b) The ionic potential with many-body Coulomb effects (shaded area) and the shifted ionic distribution (blue line).

In order for ionic latching to occur, symmetry in the ionic potential needs to be broken. In solid state systems, a large number of ions and electrons interact via Coulomb interactions. For simplicity, we assume that the negative charges form a uniform background, and that the positive ions move during polarization switching. When an ion displaced from the center of the unit cell, it disturbs the ions in its surrounding through a repulsive force so that other ions tend to move in the same direction. More precisely, the distribution of ion $|\phi(\mathbf{r})|^2$ altered from its ground state $|\phi_0(\mathbf{r})|^2$ in the double-well potential $U_{DW}(\mathbf{r})$ leads to a disturbance to charge neutrality. This local charge density, denoted as $\Delta\rho(\mathbf{r})$, is the difference between the actual ionic distribution to

the ground-state distribution

$$\Delta\rho(\mathbf{r}) \equiv |\phi(\mathbf{r})|^2 - |\phi_0(\mathbf{r})|^2 \ . \tag{4.1}$$

Accordingly, a charging potential is generated

$$\Delta V(\mathbf{r}) = \sum_{\mathbf{R}\neq 0} \int_{\Omega_0} d^3x \ V(\mathbf{r}-\mathbf{x}) \ \Delta\rho(\mathbf{x}-\mathbf{R}) \ , \tag{4.2}$$

for a unit cell centered at $\mathbf{R} = 0$. The self interaction is excluded $\mathbf{R} \neq 0$. In Eq. (4.2), Ω_0 is the unit-cell volume, and $V(\mathbf{r}) = \frac{e^2}{4\pi\epsilon_0\epsilon_r r}$ is the Coulomb potential defined by electron charge e, vacuum permittivity ϵ_0, and dielectric constant of the material ϵ_r. Figure 4.1(b) depicts the total ionic potential (shaded area) when ions are displaced to the left side. The potential is lower near $z = -z_0$ as a result of Coulomb effects, enabling the latching of ion to the left side (blue line). Therefore, the switching of polarization is allowed when Coulomb interaction is included.

Inserting Coulomb potential into Eq. (4.2), we obtain

$$\Delta V(\mathbf{r}) = \frac{e^2}{4\pi\epsilon_0\epsilon_r} \sum_{\mathbf{R}\neq 0} \int_{\Omega_0} d^3x \frac{\Delta\rho(\mathbf{x})}{|\mathbf{r}-\mathbf{x}-\mathbf{R}|} \ . \tag{4.3}$$

As the distance within a unit cell is small compared to the lattice vector $|\mathbf{r}-\mathbf{x}| < \mathbf{R}$, Eq.(4.3) can be approximated using multipole expansion. As a result, the quadrupole term produces the leading-order contribution to charging potential

$$\Delta V(\mathbf{r}) = \frac{e^2}{8\pi\epsilon_0\epsilon_r} \sum_{\mathbf{R}\neq 0} \frac{1}{R^3} \int d^3x \ \Delta\rho(\mathbf{x}) \left[3\left[\hat{u}_R \cdot (\mathbf{r}-\mathbf{x})\right]^2 - (\mathbf{r}-\mathbf{x})^2\right] + \mathcal{O}(\frac{1}{R^4}) \ , \tag{4.4}$$

where $\hat{u} = \frac{\mathbf{R}}{R}$ is a unit vector. To simplify Eq. (4.4), we assume charge distribution is factorizable along in-plane $\mathbf{r}_\parallel$ and perpendicular z directions $\Delta\rho(\mathbf{r}) = g(\mathbf{r}_\parallel)\Delta n(z)$ with $\int d^2r_\parallel g(\mathbf{r}_\parallel) = 1$ and $\int dz \Delta n(z) = 0$. The variations in the in-plane direction is neglected as well. With these simplifications, Eq. (4.4) becomes

$$\Delta V(\mathbf{r}) = -Q\left[2\langle\bar{z}\rangle\bar{z} - \langle\bar{z}^2\rangle\right] \ , \tag{4.5}$$

where $Q \equiv \frac{e^2\tilde{Q}}{8\pi\epsilon_0\epsilon_r \ a_{HO}}$, and $\tilde{Q}$ is a geometric factor

$$\tilde{Q} \equiv \sum_{\mathbf{R}\neq 0} \left(\frac{3R_z^2}{R^5} - \frac{1}{R^3}\right) a_{HO}^3 \ , \tag{4.6}$$

defined by the length of the lattice vector R, and the length of the lattice vector along the po-

larization direction R_z. In Eq. (4.5) and Eq. (4.6), a length scaling $a_{HO} = \sqrt{\frac{\hbar}{m\omega_0}}$ is introduced for convenience, where $\hbar$ is the reduced Planck constant, m is the ionic mass, and ω_0 is a frequency constant. Based on this, we use scaled position $\bar{z} = \frac{z}{a_{HO}}$ in Eq. (4.5) and in the following. The charging factor in Eq. (4.5) is defined as $\langle \bar{z}^J \rangle = \int dz \ \left(\frac{z}{a_{HO}}\right)^J \Delta n(z)$. The constant shift in charging potential in Eq. (4.5) does not affect the ionic dynamics. Therefore, major effects of local charging are described by the linear potential. For $Q > 0$, the effective ionic potential is lower on the latched side, favoring the switching of polarization when there is a small perturbation of the ionic position. In this case, the material is ferroelectric. For $Q < 0$, the ionic potential is higher on the side when the ion is displaced. As a result, the latching is unstable and the ion tends to move back. In this case, the material is nonferroelectric.

To describe ionic motion, we solve time-dependent Schrödinger equation for the ionic wave function $\phi(z,t)$

$$i\hbar\frac{\partial}{\partial t}\phi(z,t) = H_S\ \phi(z,t)\ , \tag{4.7}$$

$$H_S = -\frac{\hbar^2}{2m}\frac{\partial^2}{\partial z^2} + U_{DW}(z) + V_{THz}(t) + \Delta V(z,t)\ , \tag{4.8}$$

where H_S is the system Hamiltonian including the kinetic energy of an ion of mass m, the double-well potential, THz excitation along z direction $V_{THz} = -Q_e z E_{THz}(t)$, and the local charging potential $\Delta V(z,t)$. We assume double-well potential of the form $U_{DW}(z) \propto z^4 - Z^2 z^2$, where Z is a constant defining the positions of the potential wells and the depths of wells relative to the center. We choose the potential depth to be 50 meV, the mass $m = 7.47 \times 10^{-26}$ kg for Scandium atom, the ionic charge $Q_e = 3|e|$, the dielectric constant $\epsilon_r = 10$, and the geometric factor $\tilde{Q} = 10^{-3}$ in our calculations in the following. These parameters are only rough estimates for studying the general behaviors, and more accurate parameters are needed in future studies. We assume the ionic motion is within a single unit cell, and there is no leakage between different cells.

4.3 Relaxation via Monte Carlo method

During the switching of polarization, the interaction of the ion with the surrounding lattice leads to the dissipation of energy. The general method to solve dissipation is via the master equation [35]

$$i\hbar\frac{\partial}{\partial t}\rho_S = [H_S, \rho_S]_- + i\hbar\gamma\left(2\hat{a}\rho_S\hat{a}^\dagger - \hat{a}^\dagger\hat{a}\rho_S - \rho_S\hat{a}^\dagger\hat{a}\right)\ , \tag{4.9}$$

where $\rho_S(t) = |\phi(t)\rangle\langle\phi(t)|$ is the density matrix, H_S is the system Hamiltonian, γ is the decay constant, and $\hat{a}$ is an operator that acts on the system to describe the relaxation. In a large system that includes N components in its wave function, the elements in the density matrix grows with N^2. This quadratic growth makes the calculation of density matrix computationally expensive. As an alternative, Monte Carlo method [58] computes the dissipation based on the wave function only. The computational cost scales with N, making it a more efficient method than master equation.

In Monte Carlo calculations, the wave function is propagated with a non-Hermitian Hamiltonian [58]

$$H = H_S - i\hbar\gamma\hat{a}^\dagger\hat{a} \ , \tag{4.10}$$

where H_S is the system Hamiltonian in Eq. (4.8), $\hbar\gamma$ is the dephasing energy, and $\hat{a}^\dagger$ and $\hat{a}$ are relaxation operators. We assume the ion relaxes to the ground state of the total potential $V(z) = U_{DW}(z) + V_{THz}(t) + \Delta V(z,t)$. The THz excitation $V_{THz}(t)$ and charging potential $\Delta V(z)$ modifies the potential by adding linear terms. With these linear terms, there is a single position, denoted by z_{HO}, where $V(z)$ reaches its minimum. Using Taylor expansion at $z = z_{HO}$, the actual potential $V(z)$ is approximated by a harmonic potential $U_{HO}(z) = V(z_{HO}) + \frac{1}{2}V''(z_{HO})\,(z - z_{HO})^2$. The corresponding Hamiltonian for the harmonic oscillator is

$$H_{HO} = -\frac{\hbar^2}{2m}\frac{\partial^2}{\partial z^2} + \frac{1}{2}V''(z_{HO})\,(z - z_{HO})^2 \ , \tag{4.11}$$

where the constant $V(z_{HO})$ has been neglected. Based on the length scaling a_{HO} introduced above, the creation and annihilation operators for the harmonic oscillators are

$$\hat{a} = \frac{\sqrt{B}}{2^{\frac{3}{4}}}(\bar{z} - \bar{z}_{HO}) + \frac{1}{2^{\frac{1}{4}}\sqrt{B}}\frac{\partial}{\partial\bar{z}} \ , \tag{4.12}$$

$$\hat{a}^\dagger = \frac{\sqrt{B}}{2^{\frac{3}{4}}}(\bar{z} - \bar{z}_{HO}) - \frac{1}{2^{\frac{1}{4}}\sqrt{B}}\frac{\partial}{\partial\bar{z}} \ , \tag{4.13}$$

where $B = \frac{1}{\omega_0}\sqrt{\frac{2V''(z_{HO})}{m}}$ is unitless. The Bosonic commutation relation $[\hat{a}, \hat{a}^\dagger]_- = 1$ is satisfied.

The detailed steps of Monte Carlo calculations follow from Ref. [58] and briefly summarized here. First, the wave function is evolved with the Hamiltonian in Eq. (4.10), and a quantum jump is applied based on random processes. Then, the results are averaged over a large number of realizations to produced equivalent results to master equation. Specifically, the relaxation calculation is implemented in the following steps:

1. Evolve the wave function $|\phi(t)\rangle$ according to Eq. (4.10) in a small time step Δt

$$|\phi^{(1)}(t+\Delta t)\rangle = \left(1 - \frac{iH\Delta t}{\hbar}\right)|\phi(t)\rangle \ . \tag{4.14}$$

2. Compute the loss to the norm of the wave function $\Delta p = 1 - \langle\phi^{(1)}(t+\Delta t)|\phi^{(1)}(t+\Delta t)\rangle$.

3. Generate a random number r_{num} from a uniform distribution between 0 and 1.

4. Decide whether there is a quantum jump.

   - If $\Delta p < r_{num}$, there is no quantum jump. Normalize the new wave function $\phi(t+\Delta t) = \frac{\phi^{(1)}(t+\Delta t)}{\sqrt{\langle\phi^{(1)}(t+\Delta t)|\phi^{(1)}(t+\Delta t)\rangle}}$.
   - If $\Delta p > r_{num}$, introduce a quantum jump by computing $\phi(t+\Delta t) = a|\phi(t)\rangle$. Then, normalize the new wave function $\phi(t+\Delta t) = \frac{\phi(t+\Delta t)}{\sqrt{\langle\phi(t+\Delta t)|\phi(t+\Delta t)\rangle}}$.

With a large number of realizations $N \to \infty$, the quantity $\bar{\sigma}(t) = \frac{1}{N}\sum_{i=1}^{N}|\phi^{(i)}(t)\rangle\langle\phi^{(i)}(t)|$ is equivalent to the density matrix in the master equation in Eq. (4.9), if the initial condition $\rho(t=0) = \bar{\sigma}(t=0)$ is satisfied. [58] Therefore, the expectation value of an observable is computed by taking the average [58]

$$\langle A\rangle = \frac{1}{N}\sum_{i=1}^{N}\langle\phi^{(i)}|A|\phi^{(i)}\rangle \ , \tag{4.15}$$

where $\phi^{(i)}$ is the wave function obtained in the i^{th} realization of Monte Carlo calculations.

4.3.1 Decay of the kinetic energy

From the master equation in Eq. (4.9), the dynamics of an operator $\hat{O}$ is [35]

$$i\hbar\frac{\partial}{\partial t}\langle\hat{O}\rangle = [\hat{O}, H_S]_- + i\hbar\gamma\langle\hat{a}^\dagger[\hat{O}, a]_- + [\hat{a}^\dagger, \hat{O}]_-\hat{a}\rangle \ . \tag{4.16}$$

As an estimate of the decay rate of kinetic energy $E_k = \langle -\frac{\hbar^2}{2m}\frac{\partial^2}{\partial z^2}\rangle$, we evaluate the second term in and obtain

$$\frac{\partial}{\partial t}E_k|_{\text{deph}} = -2\gamma E_k + \frac{\hbar\gamma}{2}\sqrt{\frac{V''(z_{HO})}{m}} \ , \tag{4.17}$$

where γ is the decay rate. Denoting the decay time $\tau_{rlx} = \frac{1}{2\gamma}$, the time dependence of kinetic energy is

$$E_k(t) = E_k^0 \, e^{-\frac{t-t_0}{\tau_{rlx}}} + \frac{\hbar}{4}\sqrt{\frac{V''(z_{HO})}{m}}\left(1 - e^{-\frac{t-t_0}{\tau_{rlx}}}\right) , \tag{4.18}$$

where $E_k^0 = E_k(t_0)$ is the kinetic energy at t_0.

We compute for the ionic motion starting from the latched state on the negative side. A Gaussian pulse $E(t) = E_0 \, e^{-\frac{t^2}{\tau^2}}$ with a duration of $\tau = 160$ fs and peak field $E_0 = 25$ MV/cm is applied to switch the polarization. The relaxation time is set to $\tau_{rlx} = 80$ fs. Figure 4.2(a) shows the ionic density (color-coded background) during the excitation pulse (red line). The results are averaged from $N = 2 \times 10^4$ realizations. The solid line shows the average position $\langle z \rangle / z_0$ that shifts from the negative side to the positive side near $t = 0$. The polarization switching is followed by small oscillations near $\langle z \rangle = z_0$, which decay in about 100 fs due to relaxation. Figure 4.2(b) shows the corresponding kinetic energy during the polarization switching (black line). It reaches a maximum near $t = 0$ and decays as the ion is stabilized on the positive side. Denoting t_0 as the time when the maximum kinetic energy E_k^0 is reached, the red dashed line shows the analytics of kinetic energy following Eq. (4.18) for $t > t_0$. The decay of E_k from numerical results agree with analytics well, with small deviations due to the first term in Eq. (4.16) that is not evaluated explicitly here.

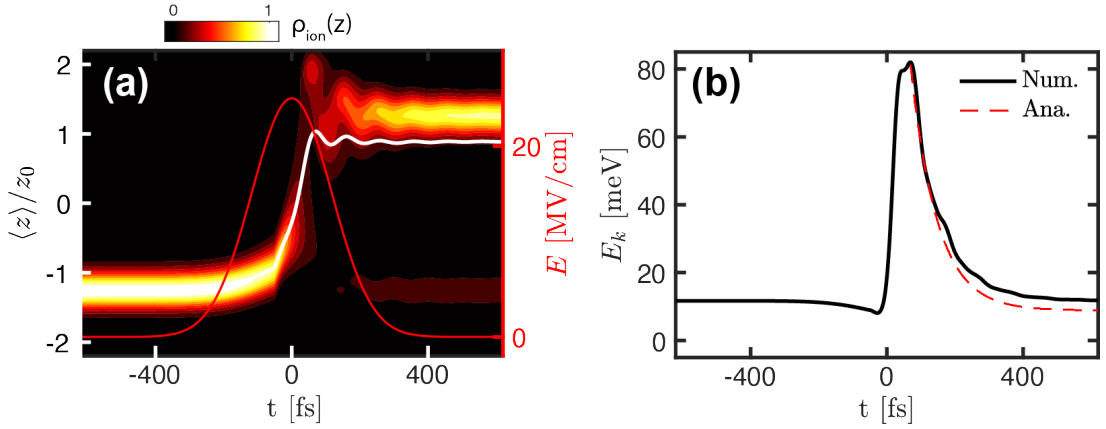


Figure 4.2: **Decay of kinetic energy due to relaxation.** (a) The color-coded plot of ionic density during the excitation of a Gaussian pulse (red line). The white line indicates the mean position of ion. (b) Numerical results (black solid line) of kinetic energy during the switching, compared to the analytics (red dashed line).

4.3.2 Convergence with the number of realizations

In Monte Carlo method, the error in the average value of an observable [Eq. (4.15)] decays with the number of realizations as $\epsilon \propto \frac{1}{\sqrt{N}}$. [58] To test the number of realizations needed in our calculations, we quantify the error in the mean position of the ion $\langle z \rangle$ during the polarization switching. Explicitly, we evaluate the relative error for different number of realizations N

$$\epsilon(N) = \frac{\max |\langle z \rangle_N(t) - \langle z \rangle_{N_0}(t)|}{\max |\langle z \rangle_{N_0}(t)|} , \tag{4.19}$$

where $\langle z \rangle_N(t)$ is the mean position as a function of time, averaged from a total of N realizations, and $N_0 = 2 \times 10^4$ is the maximum number of realizations for which $\langle z \rangle_{N_0}(t)$ is chosen as the reference. For the same excitation conditions as discussed in Sec. 4.3.1, we evaluate the relative error in $\langle z \rangle$ as a function of N. Figure. 4.3 shows the numerical results in black line, compared to the analytical trend $\epsilon = \frac{c}{\sqrt{N}}$ in the red dashed line. The constant c is found from the least-square fitting. The decrease in the relative error with the number of realizations agrees with the analytics. To reach a relative error of $\epsilon < 5\%$, a total of $N = 500$ realizations are needed. However, the convergence is pretty slow such that to get a better accuracy of $\epsilon < 1\%$, we need $N > 7500$ realizations.

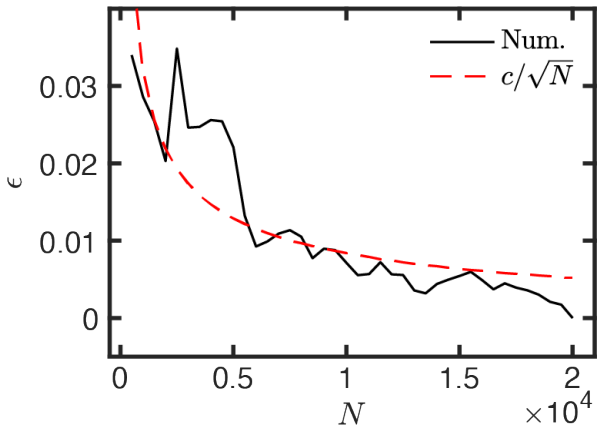


Figure 4.3: **Convergence with the number of realizations.** The error in the mean position of ion as a function of the number of realizations N, with respect to the reference computed from $N_0 = 2 \times 10^4$ realizations.

4.4 Natural switching time

In this section, we aim at identifying the natural time required for polarization to be reversed. In general, the switching of polarization is influenced by several factors including the ionic potential, strength of the pump field, and phonon relaxation. Here, our goal is to identify the natural switching time where the impact of external factors such as the strength of electric fields and relaxation are minimized. Understanding the natural switching process allows us to identify the root cause that limits the switching speed and thus provides insights into materials engineering for improving the switching speed. It also provides an estimate of the frequency of optical fields for the effective control of polarization switching.

4.4.1 Polarization switching with a linearly ramped field

To analyze the natural switching process, we apply a slow, linearly ramped electric field, to sure that changes in field strength occur over a significantly longer time scale than the motion of ions. The field $E(t)$ starts from $E = 0$ with a ramp rate of 8 MV/cm per picosecond. The linear ramp gradually increases the field strength over time, enabling the potential to exceed the threshold required for switching to take place. However, this gradual increase in field strength is intentionally slow to minimize disruptions to the ionic motion. The relaxation is switched off for simplicity. Figure 4.4(a) depicts the ionic density along z direction in a 200 fs time window near the reversal of polarization. The red line indicates the field strength. At $t < -100$ fs, the wave function is well confined, with the mean position (white solid line) changing slowly near the the left-side valley $\langle z \rangle = -z_0$. As the time approaches $t = 0$, the ion undergoes significant acceleration, leading to a rapid shift towards the positive-side valley, reaching a position near $\langle z \rangle = z_0$ within 100 fs.

Figure 4.4(b) shows ionic wave functions $|\phi(z)|^2$ (shaded area) at $t = -72$ fs when the ionic motion is slow, indicated by the first vertical dashed line in Fig. 4.4(a). The red solid line shows the ionic potential $V(z)$ lower in the right valley. Compared to the symmetric double-well potential (black dashed line), the asymmetry in the actual potential is mainly due to the external field that is used to drive the ionic motion. The wave function has a single main peak near the left-side valley. The horizontal dashed line indicates the total energy of the ion $E_{ion} = \langle \phi | \hat{H} | \phi \rangle$. In the central region where the total energy is below the potential $E_{ion} < V(z)$, the wave function enters a classically forbidden region (red shaded area). As a result, $|\phi(z)|^2$ decays from its peak position to the central region via quantum tunneling. This is indicated by the extended tail of the wave function on the right side of its peak. The existence of the tunneling region hinders the ionic motion such that $\langle z \rangle$ changes slowly as shown in Fig. 4.4(a).

Figure 4.4(c) shows the corresponding wave function and potential at $t = 50$ fs when the ionic motion is significantly faster than that shown in Fig. 4.4(b). This selected time is indicated

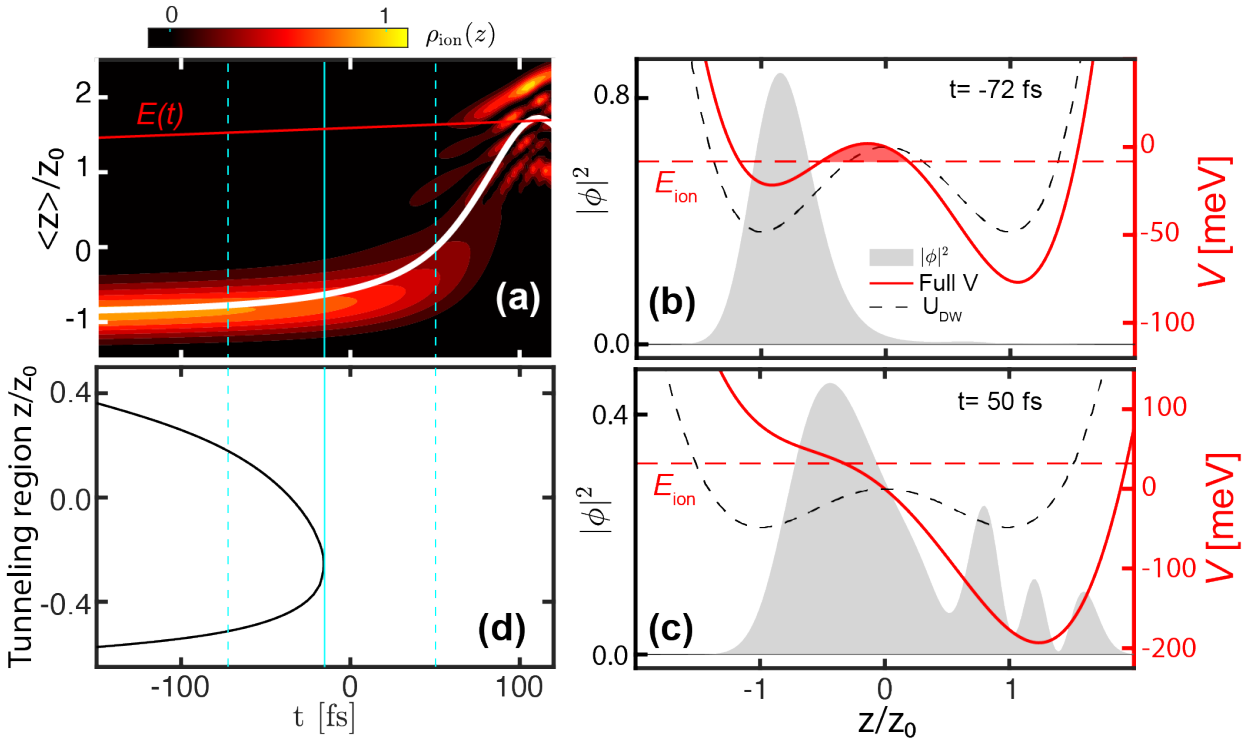


Figure 4.4: **Polarization switching under a linearly ramped field.** (a) Color-coded plot of ionic density close to the switching. The external field $E(t)$ (red line) is linear in time. The vertical dashed lines are selected times at which the wave functions $|\phi|^2$ (shaded areas) and full potential energy V (red solid lines) are shown in (b-c). The black dashed lines indicate double-well potential without charging or external field. The red horizontal dashed lines indicate the total energy of ion at selected times. (d) Tunneling region as function of time. The vertical solid indicates the vanishing of tunneling region.

by the second vertical dashed line in Fig. 4.4(a). As the peak of the wave function shifts near the center $z = 0$, there are major oscillatory features on the right side of the wave function, indicating a large kinetic energy. The ionic potential is significantly lower on the right side, favoring the motion of ion towards the right valley $z = z_0$. At the same time, the ionic potential decays monotonically between two valleys. Therefore, the ionic motion towards the right side is similar to the classical transition driven by the large external force. Comparing Fig. 4.4(b) and Fig. 4.4(c), the ionic potential evolves significantly as the position of ion changes. Since the external field varies slowly during this short time window, the major change is due to the local charging potential as the ion moves.

For the ion to move from one valley to the other, it needs to overcome the potential barrier between two valleys. In Fig. 4.4(b) where the local maximum of $V(z)$ near $z = 0$ exceeds the total energy of the ion, the ion moves by the slow, tunneling process. We define the tunneling

region to be the area within valley positions $|z| < z_0$, bounded by the positions at which $E_{ion} = V(z)$ is reached. Figure. 4.4(d) shows the tunneling region as a function of time. The upper branch and lower branch represent the boundary on the right and left side of the tunneling region, respectively. The tunneling region gradually reduces in the first 100 fs. The merge of two branches at the cyan vertical line indicates the elimination of tunneling region. This is also the time when the fast motion is initiated as shown in Fig. 4.4(a). Therefore, the elimination of tunneling region leads to the onset of rapid motion during polarization switching.

Combining Fig. 4.4(a-d), we summarize the switching process in a three-step model: 1) Initially, the motion of the ion is slow due to the presence of a tunneling region, which acts as a barrier for the polarization to be reversed. During this process, the wave function moves to opposite valley via quantum tunneling, but remains predominantly confined to the initial position. 2) The tunneling region diminishes as the ion gradually shifts to the center. At a tipping point where the tunneling region vanishes, the ion shifts with a much faster speed than the first step. 3) In the absence of the tunneling region, the switching of ion to the opposite side is driven by the large external force that moves the ion towards the potential minimum. During this process, the ion gains substantial kinetic energy.

4.4.2 A simple model for tunneling time

The study in Sec. 4.4.1 shows that the instantaneous switching of polarization is prevented by the tunneling region. To provide an estimate of tunneling time required to reach the onset of fast motion, we begin by identifying a critical ionic position where the tunneling ends. Assuming a constant external field is used, the only time dependence in the system Hamiltonian in Eq. (4.8) is present in the charging potential. In Appendix. A, we show that the total energy of the ion $E_{ion} = \langle\phi|\hat{H}|\phi\rangle$ is conserved when the charging potential is of the form $\Delta V(z) = -2Q\langle z\rangle z + Q\langle z\rangle^2$.

Defining the unit-cell dipole due to ionic displacement $d \equiv \langle z\rangle$, the full potential at a given d is

$$V_d(z) = U_{DW}(z) - Q_e z E - 2Qd\, z + Qd^2 \ , \tag{4.20}$$

where d determines the charging potential in the third term and introduces a constant shift to the total potential in the fourth term. The height of the potential barrier between two valleys, denoted as E_{barr}, is defined as the maximum value of the potential $V_d(z)$ within the range $|\langle z\rangle| < z_0$. Without charging or electric field, the maximum barrier potential is obtained at $z = 0$. When charging and electric field are added, there is a small shift to the barrier position. Ignoring that small shift from $z = 0$, the barrier height can be approximated by $E_{barr} = V_d(z = 0) = Qd^2$. Given a constant ionic energy E_{ion}, we define a threshold position d_{th} at which the total energy

equals potential barrier $E_{ion} = Qd^2$, which gives

$$d_{th} = \pm\sqrt{\frac{E_{ion}}{Q}} \, . \tag{4.21}$$

When the ion is positioned within the threshold boundaries on either side $|\langle z\rangle| < |d_{th}|$, the maximum potential is lower than ionic energy $E_{barr} < E_{ion}$. In this scenario, the ion does not encounter a tunneling region. On the other hand, if the ion is located further away from the center $|\langle z\rangle| > |d_{th}|$, the ion moves to the opposite valley via tunneling.

To illustrate the threshold position where tunneling is ended, we show an example of the polarization switching similar to Sec. 4.4.1 but using a constant electric field, so that the total ionic energy is conserved. Figure 4.5(a) shows the ionic density (color-coded background) under a constant field of $E = 20$ MV/cm (red line). The field is switched on at $t = 0$ and moves the ion in the positive direction. Figure 4.5(b) shows the kinetic energy $E_k = \langle\phi| - \frac{\hbar^2}{2m}\frac{\partial^2}{\partial z^2}|\phi\rangle$, potential energy $V = \langle\phi|V_d(z)|\phi\rangle$, and the total energy of the ion $E_{ion} = E_k + V$ as a function of time. The energy is computed relative to the center of the double-potential $U_{DW}(z = 0)$ without charging or pump field. After the pump field is switched on $t > 0$, the kinetic energy and potential energy change oppositely, and the total energy E_{ion} is constant. Figure 4.5(c) shows ionic potentials at selected times indicated by the vertical lines in Fig. 4.5(a-b). The horizontal dashed line indicates the total energy E_{ion}. At $t = 40$ fs when the ionic reaches $\langle z\rangle = d_1$ (black vertical line), the potential $V_{d_1}(z)$ (black dashed line) has its local maximum larger than E_{ion} near $z = 0$, with the gray area indicating the tunneling region. When the ion moves to $\langle z\rangle = d_2$ (vertical red line), the local maximum of $V_{d2}(z)$ (red line) near $z = 0$ coincides with E_{ion}, indicating the removal of tunneling region. In this case, the threshold position d_{th} is reached at $d_2 = -0.48z_0$.

During the switching of ionic position from the left to the right, a quantity that defines the switching efficiency is the probability of finding the ion on the right side. This probability, denoted as R, is defined as

$$R \equiv \int_0^{z_{max}} dz \; |\phi(z)|^2 \, , \tag{4.22}$$

where z_{max} is the boundary position on the positive side. As the ion shifts from left to right, it increases from $R = 0$ to $R = 1$. While the ionic density can be broadly distributed between two valleys during the switching, it peaks near the valley positions $z = \pm z_0$ as the potential reaches local minima. As an estimate of the ionic mean position, we approximate it by an average of the valley positions on two sides, weighted by the probability of finding the ion on two sides $d = z_R R + z_L(1 - R)$, where $z_{L(R)}$ is the position of the left (right) valley. From this, we get a

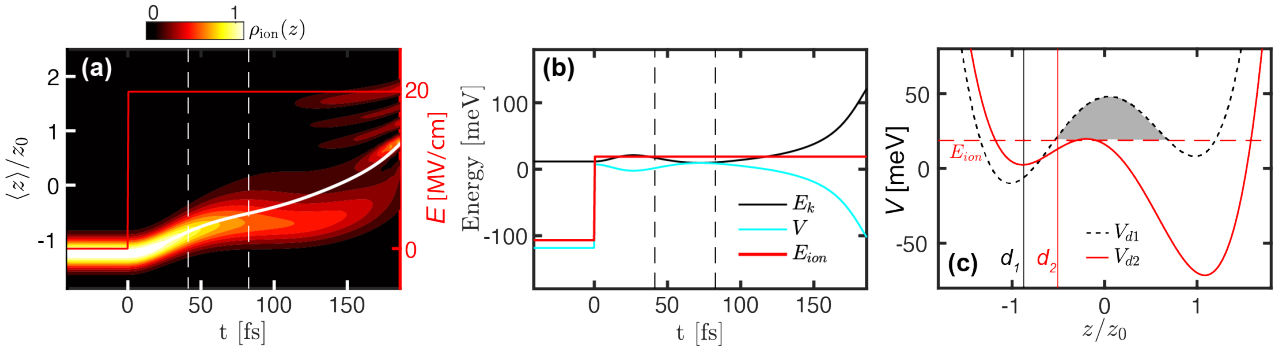


Figure 4.5: **A simple model for the tunneling threshold.** a) Ionic density (color-coded background) under a constant electric field (red line) turned on at $t = 0$. (b) Kinetic energy E_k, potential energy V, and the total energy of the ion $E_{ion} = E_k + V$ as a function of time. The vertical lines in (a-b) indicate the selected times at which the ionic potentials $V_d(z)$ are shown in (c). The average position of the ion d_1, d_2 are indicated by vertical lines. The horizontal dashed line indicates E_{ion} that is kept constant at $t > 0$.

linear relation

$$R = \frac{d - z_L}{z_R - z_L} \,, \tag{4.23}$$

which expresses R as a function of the ionic mean position d. Figure 4.6 shows R as a function of d/z_0 from full computations during the initial switching. When the ion is located in the left valley $d = -z_0$, the increase in R is negligible when d increases. This is due to the minute leakage of the wave function towards the right side. As the position shifts to $d > -0.7z_0$, the increase in R with d enters the linear regime. The vertical line indicates the threshold position d_{th} where the tunneling region becomes vanishing. We compare the full results with the simple model of Eq. (4.23), indicated by the red dashed line. The valley positions are chosen to be $z_L = -0.7z_0$ and $z_R = z_0$ to take into account the asymmetry in the ionic potential when there is a strong field. The linear model approximates the full results well near d_{th}. The threshold probability, denoted as R_{th}, is defined to be the value of R when $d = d_{th}$ is reached. According to the linear model, this threshold probability is calculated to be $R_{th} = 13\%$.

The rate at which the probability on the right side changes, denoted as $\frac{dR}{dt}$, is determined by the probability current $j(z,t)$ via

$$\frac{dR}{dt} = j(0,t) - j(z_{max},t) \,, \tag{4.24}$$

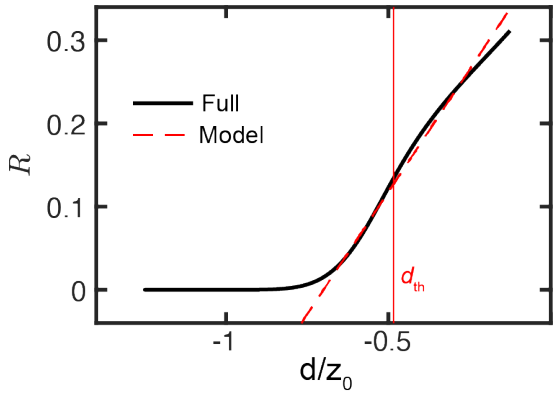


Figure 4.6: Probability of wave function on the right side R as function of d/z_0. The solid line shows R from full results, and the red dashed line shows the linear model. The vertical line indicates the threshold ionic position d_{th} for which the tunneling is removed.

where

$$j(z,t) = \frac{\hbar}{m}\mathrm{Im}[\phi^* \frac{\partial}{\partial z}\phi] \ . \tag{4.25}$$

Because the wave function is vanishing at the boundary $\phi(z_{max}) = 0$, we have $j(z_{max}, t) = 0$. This implies that $\frac{dR}{dt}$ is governed by the probability flow passing through the center $j(z = 0)$. To obtain the tunneling time to reach the threshold probability R_{th} discussed above, we quantify $j(z,t)$ during the tunneling. As $j(z,t)$ has a unit of 1/time, we define a scaled probability current

$$\Delta R_j(z,t) = j(z,t)\ \Delta t \ , \tag{4.26}$$

which is the change of R over a specific time interval Δt. We choose this time interval to be $\Delta t = 100$ fs, which is the typical time scale for the polarization switching to take place.

Figure 4.7(a) shows ΔR_j during the tunneling at selected ionic positions $\langle z \rangle = -0.7 z_0$ (black line), $\langle z \rangle = -0.6 z_0$ (red line), and $\langle z \rangle = -0.5 z_0$ (cyan line). As the ion moves towards the positive direction, the peak of ΔR_j also moves in the same direction. The distribution of ΔR_j gets broader in the meantime. Figure. 4.7(b) shows the magnitude of ΔR_j at the center between two valleys $z = 0$. It is nearly vanishing for the first 50 fs, but starts to rise significantly afterwards. We quantify the average probability current in $0 < t < 100$ fs to be $\Delta \bar{R}_j = 0.18$, which states that R increases 18% in a time interval of $\Delta t = 100$ fs. Given the threshold probability $R_{th} = 13\%$ as discussed above, the tunneling time is estimated to be $T_{tnl} = \frac{R_{th}\Delta t}{\Delta \bar{R}_j} = 72$ fs. As the major transition does not occur before tunneling has ended, this tunneling time is an important measure of the delay of ionic response to an applied field.

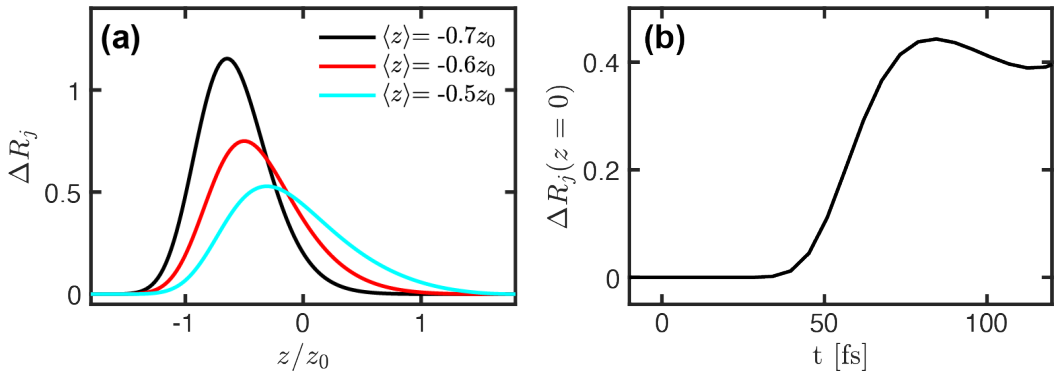


Figure 4.7: **Probability current during tunneling.** (a) Scaled probability current $\Delta R_j = j\Delta t$ at selected ionic positions $\langle z\rangle = -0.7z_0$ (black line), $\langle z\rangle = -0.6z_0$ (red line), and $\langle z\rangle = -0.5z_0$ (cyan line), during a time interval of $\Delta t = 100$ fs. (b) Magnitude of the scaled probability current ΔR_j at the center of two valleys ($z = 0$).

4.4.3 Classical avalanche time

In Sec. 4.4.1, we demonstrated that, once the tunneling region is removed, the fast transition of ion to the opposite valley occurs in the presence of a large difference in the ionic potential between two sides. This avalanche process aligns with classical mechanics, where a particle moves towards the potential minimum with a gain of its kinetic energy. To further explore the factors influencing the switching speed, we compare the full dynamics with classical motion predictions described by $\frac{\partial^2 z}{\partial t^2} = \frac{1}{m}F(z)$, where $F(z)$ is the force on a classical particle of mass m. For simplicity, we assume that the ionic potential is static in classical calculation.

Figure 4.8(a) shows the wave function $|\phi|^2$ (shaded area) and the potential (red line) at the onset of classical avalanche. The wave function $|\phi|^2$ is centered on the left side, with its mean position indicated by the vertical line. The potential is lower on the right side. In classical calculation, we approximate the wave function by a particle released at $z = -0.3z_0$ at $t = 0$, as indicated by the light blue sphere. An initial velocity in the positive direction $v = 1.1 \times 10^{-2}$ Å/fs is assumed, based on the full results. Figure 4.8(b) shows the average position from full results (shaded area) and classical dynamics (blue line), with their positions at $t = 0$ aligned. In both computations, the transition to the positive valley $\langle z\rangle = z_0$ is realized in 120 fs. We define the traveling time from the onset of classical transition to the valley on the opposite side to be the classical avalanche time, quantified to be $T_{class} = 120$ fs in this calculation. Figure 4.8(c) shows the average velocity $v = \frac{d\langle z\rangle}{dt}$ from full results (shaded area) and the classical velocity (blue line). While there are discrepancies between two calculations, the maximum switching speed close to $v = 5 \times 10^{-3}$ Å/fs is obtained in both results. Therefore, we conclude that the switching speed during classical avalanche is determined by the ionic potential.

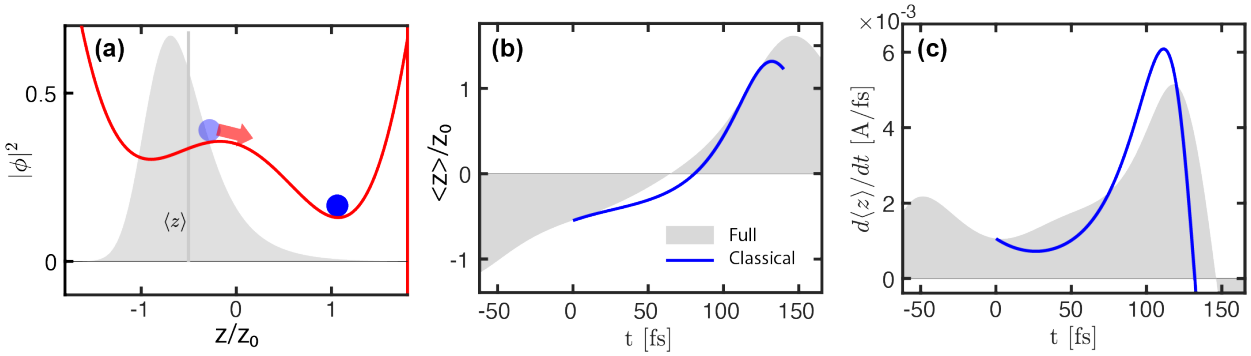


Figure 4.8: **Classical avalanche time.** (a) Ionic wave function $|\phi|^2$ (shaded area) and the potential (red line) at the onset of classical transition. In classical model, we assume a particle is released at $z = -0.3z_0$ (light blue sphere) with a small initial velocity to the right side. Due to the lower potential on the right side, it moves to the potential minimum (dark blue sphere). (b) Average position and (c) velocity from full computation (shaded areas), compared to classical dynamics (blue lines). The position of the particle in classical model is shifted to full results at $t = 0$.

In summary, during polarization switching, the ionic motion involves a tunneling stage and a classical transition. We identify a threshold position d_{th} when the tunneling ends, at which the probability of finding the ion on the opposite side R_{th} is quantified. The tunneling rate is analyzed via the probability current, from which we obtain the tunneling time $T_{tnl} = 72$ fs. After the tunneling step, the ionic motion can be approximated by classical mechanics. We quantify the classical avalanche time for an ion to move from the threshold d_{th} to the opposite valley, which is about $T_{class} = 120$ fs. Including both the tunneling time and classical avalanche time, the natural switching time is about T_{flip} =200 fs. It is important to note that the precise switching time can be affected by materials parameters including the ionic potential, mass, and lattice structures. Our discussions here provide a rough time scale for the natural switching.

4.5 THz control of polarization switching

Building upon the fundamental switching mechanism outlined in Sec. 4.4, we aim for exploring the potential of manipulating the switching process using light fields. The interaction between lightwave and ferroelectrics is a potential route towards ultrafast control of switching. As the natural switching time is on the order of the duration of THz pulses, we start with low-frequency THz field as the excitation source. The ionic motion is computed with few-cycle THz pulses. Additionally, we analyze the impact on the switching efficiency when we vary the duration of the light pulse. This provides an estimate of the frequency limit of the control source. In the end,

we present preliminary results of experiment–theory comparison for the polarization switching in ScAlN ferroelectric materials excited by a THz field.

4.5.1 Multiple switchings with THz pulses

To explore the possibility of ferroelectrics switching using THz fields, we start with few-cycle THz pulses as the excitation sources. The frequency of the THz field is set at $\nu = 0.2$ THz, with a half-cycle duration much longer than natural switching time to ensure complete switching. The strength of peak field is $E = 30$ MV/cm. We assume the relaxation time to be τ_{rlx} =80 fs. Figure 4.9(a-c) shows the ionic density along z direction under THz pulses (blue shaded area) of the duration of 0.75 cycles, one cycle, and two cycles. For the 0.75-cycle pump pulse, the ion switches to the positive side near $t = 0$ within the main peak of THz pulse. After that, it oscillates back slightly during the negative cycle of the THz pulse, and relaxes to the switched position. As the duration increases to one cycle, an extra switching is seen after the main THz peak, which brings the ion back to its initial position. Further increasing the duration to two cycles, switching is initiated at earlier time and multiple switchings are observed following the change of direction of the THz pulse. In this case, a total of five switchings occur within a few picoseconds.

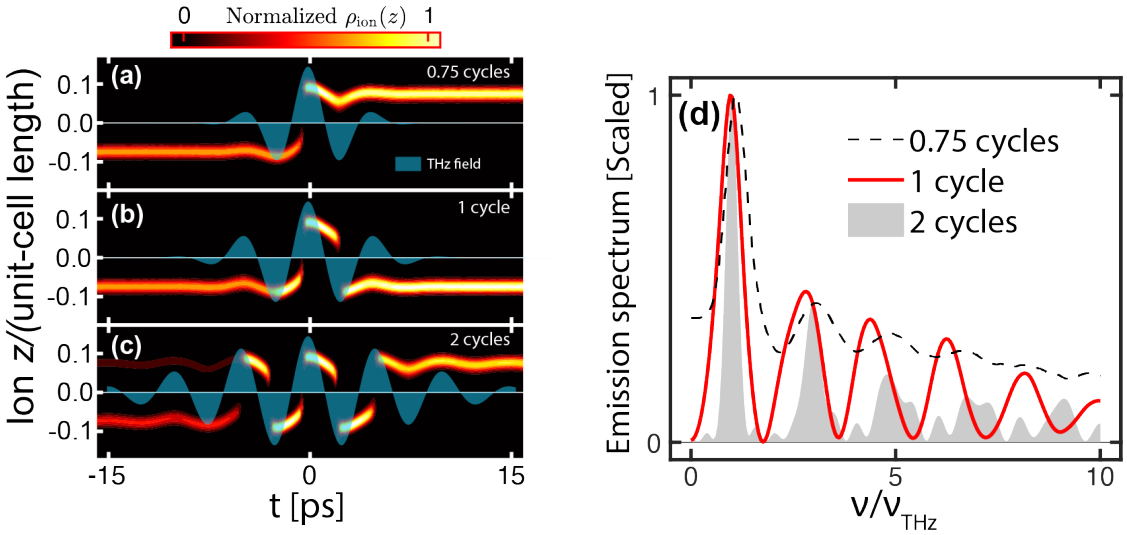


Figure 4.9: **Ultrafast switching driven by THz field.** (a-c) Color-coded plot of ionic density driven by THz field with durations of (a) 0.75 cycles, (b) one cycle, and (c) two cycles at the frequency of $\nu = 0.2$ THz. The blue shaded areas indicate the THz field. (d) Emission spectra of polarization switching under pump field of the durations of 0.75 cycles (black dashed line), one cycle (red solid line), and two cycles (gray shaded area).

It is interesting that the ionic motion does not follow sinusoidal changes in the pump pulse,

but the transition occurs on a much faster time scale. This indicates strong nonliearities in the switching process. We compute the emission field due to polarization switching $E(t) \propto -\frac{\partial P}{\partial t}$. Figure. 4.9(d) compares the emission spectra $|E(\omega)|^2$ for the polarization switching shown in Fig. 4.9(a-c). The spectra are normalized to their peaks near the pump frequency ν_{THz}. From all three pump durations, strong high-harmonic peaks are shown. For the 0.75-cycle pump pulse, the emission spectrum (black dashed line) shows broad peaks especially at $\nu/\nu_{THz} > 5$. With the single-cycle pump pulse, four distinct peaks above the fundamental frequency are observed (red line). The intensity of the third-order harmonic peak reaches 40% of the fundamental peak, and the intensities of higher-order peaks decay slowly. For the excitation with a two-cycle pump pulse, more high-harmonic peaks are observed (shaded area) with linewidths narrower than those from the single-cycle pump. This demonstrates the potential of extreme high-harmonic generation from ferroelectric polarization switching.

4.5.2 Effect of pump duration on switching efficiency

During the THz excitation of ferroelectrics, the polarization direction follows the THz field. If the THz pulse frequency increases, we also expect the polarization switching frequency to increase. However, with higher frequencies, the duration of a half cycle gets shorter, which means there is less time for the polarization to switch. The natural switching time discussed in Sec. 4.4 sets a limit on the pulse duration required for an effective polarization switching. To test this, we compute polarization switching under a unipolar, Gaussian light pulse of varying durations. We use a unipolar pulse to ensure that the ion is driven in one direction, thereby eliminating the influence of opposing electric fields on the switching direction. The peak field is fixed at $E = 25$ MV/cm, and the relaxation time is set as τ_{rlx} =160 fs. For the initial state on the left side, we quantify the switching efficiency as the probability on the right side R.

Figure 4.10(a) shows the maximum R during the pump pulse (black line) and the final R after the pump pulse (red line) as a function of the ratio between pump duration and the natural switching time τ/T_{flip}. Overall, the switching efficiency increases with pump duration. For short pump durations ($\tau/T_{flip} < 0.3$), the switching efficiency increases with τ rapidly. The rate of R increase then gets slowed down, where the final R becomes lower than the maximal R as shown in the shaded area. In this region, the switching is partially reversed after the pump. For $\tau/T_{flip} > 3$, the flip becomes irreversible and R saturates near one. We define the onset of switching to be $R = 0.5$ (horizontal line). The final switching efficiency reaches the $R = 0.5$ when $\tau = T_{flip}$, verifying the pump duration longer than natural flip time is needed for switching.

To investigate the reason of the reversible switching in $0.3T_{flip} < \tau < 3T_{flip}$, we perform an energy analysis in the following. Neglecting the external field, the asymmetry in the ionic

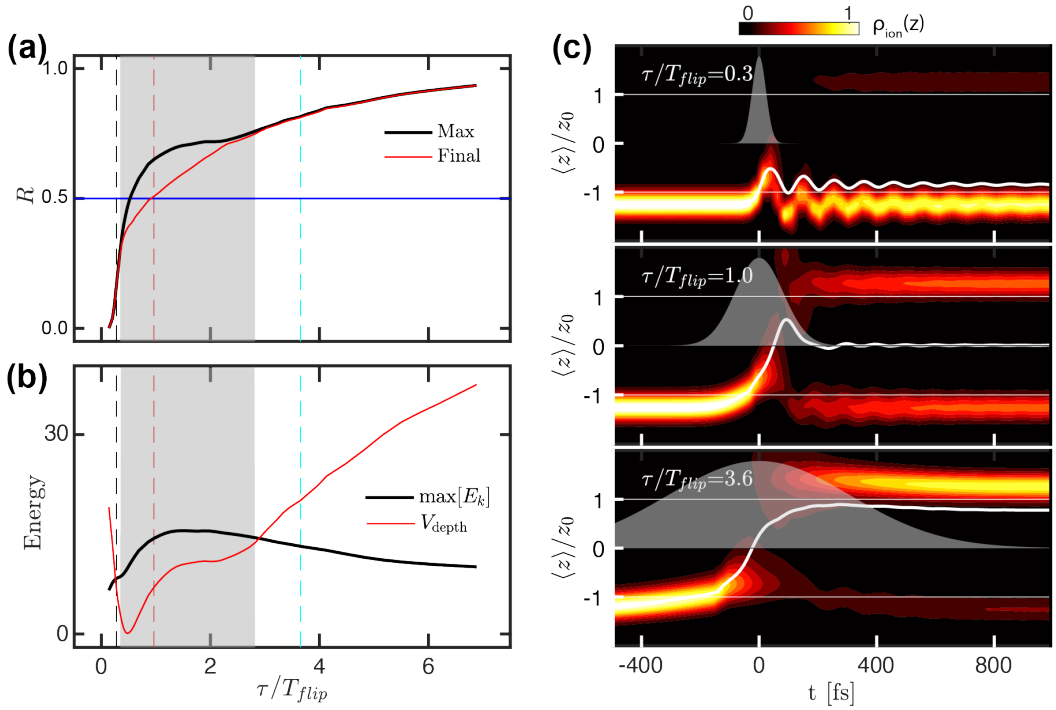


Figure 4.10: **Effect of pump duration on switching efficiency.** (a) The maximum R during the pump pulse (black line) and the final R after the pump (red line) as a function of τ/T_{flip}. The shaded area indicate the regime where the flip is reversible. (b) The maximal E_k during the excitation (black line) compared to the potential depth $V_{\rm depth}$ for the ion to move to the center. (c) Color-coded plot of ionic density for selected cases $\tau/T_{flip} = 0.3$ (top frame), 1.0 (middle frame), and 3.6 (bottom frame). The white line shows the average ionic position, and shaded area shows the pump field.

potential on two sides comes from the charging potential $\Delta V(z) = -2Q\langle z\rangle z$. We define a potential depth $V_{\rm depth}$ as the difference in $\Delta V(z)$ between the position where the ion is maximally switched, $z = \langle z\rangle_{max}$, and the center between two valleys $z = 0$

$$V_{\rm depth} = 2Q\langle z\rangle^2_{max} \,. \tag{4.27}$$

This provides an estimate of the excess kinetic energy needed for the ion to move from $\langle z\rangle_{max}$ to the center. Figure 4.10(b) compares $V_{\rm depth}$ with the maximal kinetic energy obtained during the switching. It shows that the kinetic energy exceeds the potential depth $E_k > V_{\rm depth}$ in the reversible region, but the opposite is true in the initial growth and the final saturation regions. Therefore, the reversed motion is caused by the excess kinetic energy that moves the ion back towards the center.

The vertical dashed lines in Fig. 4.10(a-b) indicate the selected cases where the wave functions

are shown in Fig. 4.10(c), for $\tau/T_{flip} = 0.3,\ 1.0,\ 3.6$ in the top, middle and bottom frames. The white solid line shows the average position $\langle z\rangle/z_0$, and the shaded area shows the pump field. For $\tau/T_{flip} = 0.3$, the wave function moves towards the positive side near $t = 0$, but immediately moves back as the field vanishes. In this case, there is no transition since the pump duration is much shorter than natural switching time. For $\tau/T_{flip} = 1$, the displacement of ion during the pump is longer compared to that in the top frame. The maximal position reaches the positive side $\langle z\rangle_{max} > 0$ near the end of the pump field, after which the reverse motion occurs. The final state is equally distributed on two sides. For $\tau/T_{flip} = 3.6$, the ionic position reaches the valley at $\langle z\rangle = z_0$ during the pump field, reaching a switching efficiency $R = 80\%$.

The dependence of R on pump duration is also expected to change with ionic relaxation, as the ionic distribution is largely affected by its energy. To quantify this, we computed switchign efficiency R after the pump pulse for different relaxation time τ_{rlx}. Figure 4.11 shows R as a function of τ/T_{flip} for different relaxation time τ_{rlx}, expressed in ratios to the natural flip time T_{flip}. The initial increase of R with pump duration becomes faster with a shorter τ_{rlx}. For $\tau_{rlx} = 0.4T_{flip}$, an efficiency of switching $R = 80\%$ is reached at $\tau = 1.2T_{flip}$, which is significantly reduced from $\tau = 4.1T_{flip}$ needed with a longer relaxation time $\tau_{rlx} = 1.6T_{flip}$. For selected relaxation time $\tau_{rlx} = 0.4T_{flip},\ 0.8T_{flip}$, and $1.6T_{flip}$, the threshold pump duration to reach $R = 80\%$ are $\tau = 4.1T_{flip}, 3.5T_{flip}$, and $1.2T_{flip}$. Based on the T_{flip} discussed in Sec. 4.4, these pulse durations correspond to THz frequencies ν =0.6 THz, 0.7 THz, and 2.0 THz, respectively. Therefore, the maximum frequency of the control source for an effective polarization switching is influenced by both the natural switching time and the relaxation time.

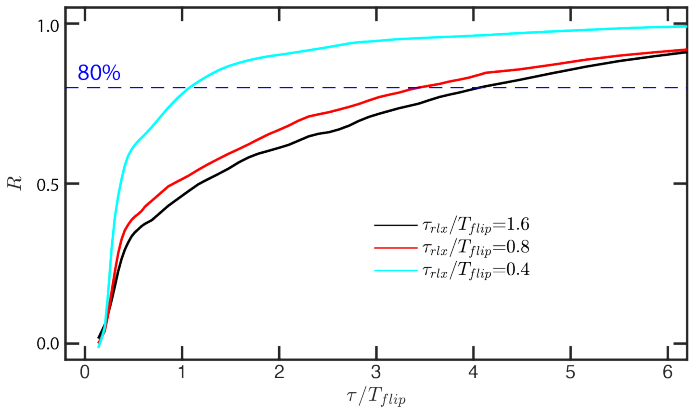


Figure 4.11: Switching efficiency R as a function of τ/T_{flip}, for selected ratios between relaxation time and the flip time τ_{rlx}/T_{flip}=1.6 (black line), 0.8 (red line), and 0.4 (cyan line).

4.5.3 Experiment–theory comparison of ultrafast switching

As a preliminary study of the switching speed, our collaborators (Rupert Huber) performed near-field experiments to probe the polarization switching. The experiments were performed on $Sc_{0.1}Al_{0.9}N$ ferroelectric samples (Zetian Mi), with a control sample of silicon that is not ferroelectric. After being excited by the 1.5-cycle THz pulse at the frequency of $\nu = 1$ THz, the total field is collected from a small area near the sample using a near-field tip. In this way, the changes induced by polarization switching are detected. Figure 4.12(a-b) show experimental data of the normalized THz fields at different pump powers. For $Sc_{0.1}Al_{0.9}N$ sample [Fig. 4.12(a)], the shape of the THz field is unchanged as pump power increases from 17.5 W (black line) to 35.0 W (blue line). However, the relative heights of peaks at $t > 0.5$ ps are reduced when pump power reaches 70.0 W (red line). This reduction of field strength is not observed in the control sample of silicon [Fig. 4.12(b)], where the shape of total field is unchanged at pump powers from 17.5 W to 70.0 W.

We perform theory computations accordingly using weak field and strong field excitations to study the effect of polarization switching. The threshold field for switching is $E = 22$ MV/cm in our system. We compute the total field $E_T = E_{in} + C\ E_R$ including the incident field E_{in} and the emission field E_R due to polarization switching. The emission field contribution is amplified by a factor C to take into account the reduced area being collected and thus the amplification of the emission field. We choose an enhancement factor $C = 6 \times 10^3$ to produce sizable changes as detected in experiments. The total field E_T is averaged over the finite pump spot assuming parabolic pump profile $E(r) = E_0 \left(1 - \left(\frac{r}{L}\right)^2\right)$ where E_0 is the peak field at the center of the spot, and L is the radius of pump spot. The averaging is computed including the central region where $r < 0.8L$.

Figure 4.12(c) shows the normalized field when the pump strength is below the switching threshold ($E_0 = 15$ MV/cm, shaded area), compared to the results under high pump field above the threshold ($E_0 = 30$ MV/cm, red line). The field is normalized at $t = -0.5$ ps before polarization switching occurs. At high pump field when switching occurs, the relative heights of the peaks at $t = 0$ and $t = 0.5$ ps are reduced. These can be correlated with the ionic motion shown in Fig. 4.12(d). The ionic density is shown in color-coded background and mean position is shown in the white line. The pump field is indicated by the shaded area. Polarization switching is observed at the highest peak of the pump field and the dip after it, synchronizing with the shape changes in E_T shown in Fig. 4.12(c). While further investigations are needed to analyze the details of experimental measurements, the shape changes in the electric field that occurs on the sub-picosecond time scale are signatures of ultrafast ferroelectrics switching in $Sc_{0.1}Al_{0.9}N$ samples.

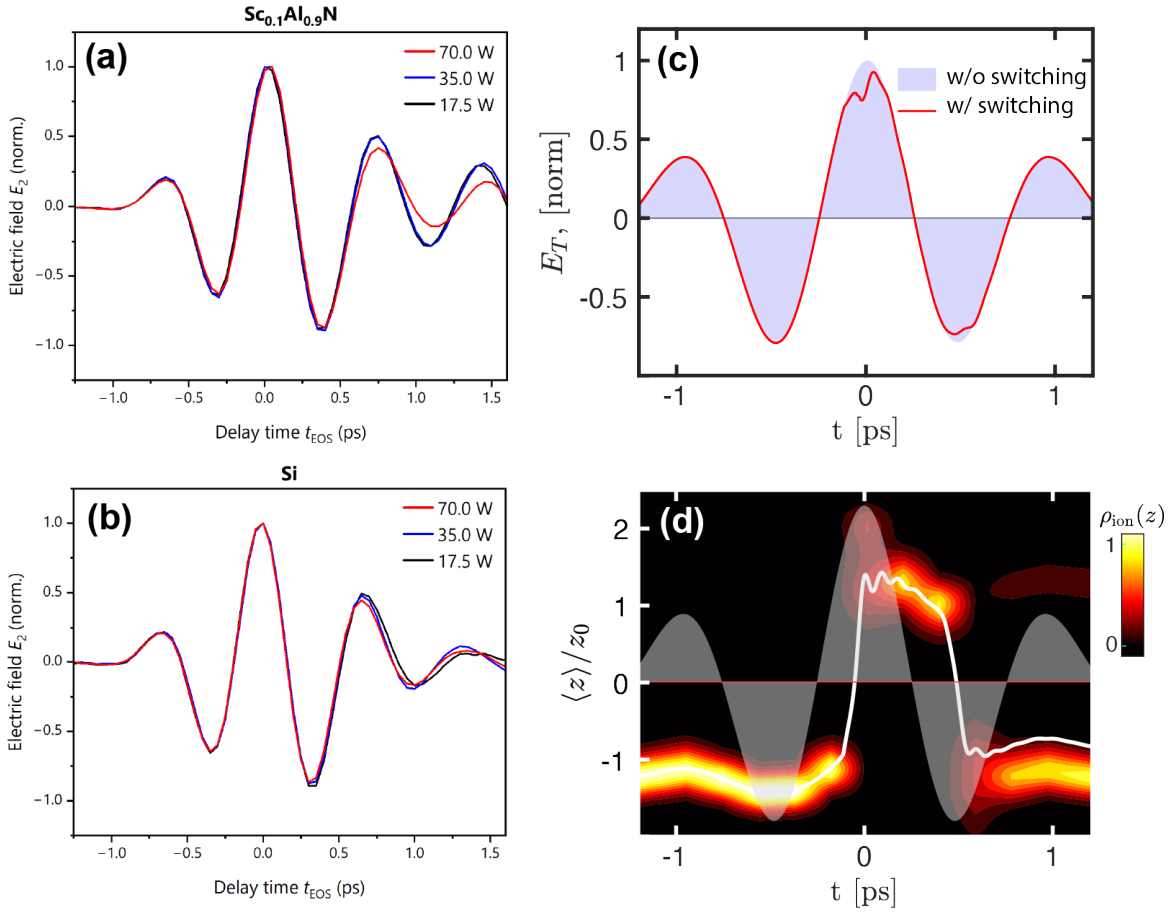


Figure 4.12: **Experiment–theory comparison of ultrafast switching.** Normalized THz fields from (a) ferroelectric $Sc_{0.1}Al_{0.9}N$ and (b) a control sample of silicon at pump power of 17.5 W (black line), 35.0 W (blue line), and 70.0 W (red line). (c) Computed field without (shaded area) and with (red line) polarization switching. The field strengths are scaled to be the same at t=-0.5ps before switching occurs. (d) Ionic density (color-coded background) and mean position (white line) under strong excitations. The gray shaded area indicates the THz pump field.

4.6 Conclusion and outlook

In conclusion, we presented a microscopic theory for the switching of ferroelectric polarization that includes the effects of local charging and phonon relaxation. Our calculation highlights the importance of many-body Coulomb interactions in the switching process. The switching mechanism is identified by a three-step process including the initial tunneling stage, the tipping point where the tunneling region is eliminated, and a classical avalanche. The current analysis, based on preliminary estimations of ionic potentials, predicts sub-picosecond natural switching time. To determine a more accurate switching time, additional information will be needed from *ab ini-*

tio calculations about the ionic potential and lattice structures. Furthermore, the theory we have discussed so far considers the motion of a single ion within the unit cell. As the actual structural changes are likely to involve different types of ions, extending the current theory to multiple ions can shed light on how the interactions among multiple ions influence the polarization switching.

In addition, we explored the control of polarization switching using few-cycle THz pulses. Excited by the THz field at the frequency of $\nu = 0.2$ THz, ultrafast switching of polarization is predicted, accompanied by strong high-harmonic generation. To increase the frequency of polarization switching with higher-frequency pulses, we need to take into account both the natural switching time and the relaxation time. Finally, as a preliminary study, we presented an experimental–theory comparison of the polarization field in ScAlN ferroelectric materials, showing evidence of sub-picosecond switching time. Future studies are needed to verify the details in these switching processes, such as the limit of ionic switching frequencies, effect of pump field, and verification of high-harmonic generation. These investigations will deepen our understanding of the polarization switching in novel nitrides and explore ways utilize them for high-speed electronics and memories.

CHAPTER 5

Coherent-Phonon Oscillations in Quantum Heterostructures

5.1 Introduction

In quantum optics theory [35, 59], a coherent state $|\alpha\rangle$ is defined as the eigenstate of the annihilation operator $\hat{a}|\alpha\rangle = \alpha|\alpha\rangle$ and can be constructed from a superposition of Fock states $|n\rangle$ via $|\alpha\rangle = \sum_{n=0}^{\infty} \frac{\alpha^n}{\sqrt{n!}} e^{-\frac{|\alpha|^2}{2}} |n\rangle$. Coherent state is also a displaced vacuum state $|\alpha\rangle = \hat{D}(\alpha)|0\rangle$ under the displacement operator $\hat{D}(\alpha) = e^{\alpha a^\dagger - \alpha^* a}$. Similarly, coherent phonon is condensed matter corresponds to the average lattice displacement under non-equilibrium conditions [33, 34]. In this case, coherent phonon amplitude, defined as the expectation value of phonon annihilation operator $D = \langle \hat{D} \rangle$, indicates the magnitude of lattice displacement. Coherent phonons have been detected in various systems including bulk GaN [28], carbon nanotudes [29], semiconductor quantum dots [30], and van der Waals materials [31, 32]. The most common way for generating coherent phonons is to excite the crystal ultrfast using femtosecond pump pulses, after which the oscillations in time domain are detected using pump-probe techniques. [28, 30, 31] Apart from direct observations of the structural changes in the time domain, coherent phonons enable the generation of novel quantum phases such as enhanced superconductivity [60] and ultrafast ferroelectric polarization switching [53].

From the fundamental point of view, the dynamics of coherent phonons reveals the underlying principles of electron–phonon interactions and carrier dynamics. Here, we study the microscopic mechanism of coherent phonon generation in quantum heterostructures and its effects on photoluminescence (PL) spectra. We start with an introduction to coherent phonons and our method to compute PL based on semiconductor luminescence equations (SLEs). Then, we focus on a specific system: transition metal dichalcogenides (TMDCs) heterobilayers. While this system has been demonstrated to realize charge separation on the ultrafast time scales [9], the mechanism of this charge transfer is not well understood. This is particularly intriguing in van der Waals heterostructures where charge transfer is expected to be slow due to the weak interactions be-

tween different layers. We explore different mechanisms in the charge transfer that can lead to coherent-phonon oscillations. Our results demonstrate the potential of using the spectroscopic features of coherent phonons as a means to detect charge dynamics in quantum heterostructures.

5.2 Dynamics of coherent phonon amplitude

To study the mechanism for the generation of coherent phonons, we start with the general phonon Hamiltonian including free phonon energies and electron–phonon interactions [35]

$$H_{\rm ph} = \sum_{j,\mathbf{p}} \hbar\Omega_{j,\mathbf{p}} \hat{D}^\dagger_{j,\mathbf{p}} \hat{D}_{j,\mathbf{p}} + \sum_{\lambda,\mathbf{k},j,\mathbf{p}} G^\lambda_{j,\mathbf{p}}\, a^\dagger_{\lambda,\mathbf{k}} a_{\lambda,\mathbf{k}+\mathbf{p}} \left(\hat{D}_{j,-\mathbf{p}} + \hat{D}^\dagger_{j,\mathbf{p}}\right) \ , \tag{5.1}$$

where $\hbar\Omega_{j,\mathbf{p}}$ is the phonon energy at phonon branch j and wavevector $\mathbf{p}$, $\hat{D}^{(\dagger)}_{j,\mathbf{p}}$ is the phonon annihilation (creation) operator, $a^{(\dagger)}_{\lambda,\mathbf{k}}$ is the electron annihilation (creation) operator at band λ and wavevector $\mathbf{k}$, and $G^\lambda_{j,\mathbf{p}}$ is the electron-phonon matrix element. For simplicity, we consider a single phonon branch and omit the branch index j in the following. From Eq. (5.1), coherent phonon amplitude, denoted as $D_\mathbf{p} = \langle \hat{D}_\mathbf{p} \rangle$, has the density-like source $\langle a^\dagger_{\lambda,\mathbf{k}} a_{\lambda,\mathbf{k}+\mathbf{p}} \rangle$ in its Heisenberg equation of motion. Under the homogeneous condition, only diagonal terms are nonvanishing and thus coherent phonon amplitude is nonvanishing for $\mathbf{p} = 0$ only. In the following, we discuss $D_{\mathbf{p}=0}$, and omit the subscript. Also, we focus on optical phonons which have a finite energy at $\mathbf{p} = 0$. From Eq. (5.1), the dynamics of coherent phonon amplitude reads [35]

$$i\hbar \frac{\partial}{\partial t} D = \left(\hbar\Omega - i\gamma_D\right) D + \sum_\lambda G^\lambda \sum_\mathbf{k} \langle a^\dagger_{\lambda,\mathbf{k}} a_{\lambda,\mathbf{k}} \rangle \ , \tag{5.2}$$

where a phenomenological dephasing constant γ_D is added to describe the decay of phonon coherence from higher-order correlations. In Eq. (5.2), the source to D includes carrier densities $\langle a^\dagger_{\lambda,\mathbf{k}} a_{\lambda,\mathbf{k}} \rangle$ from all bands. In the electron–hole picture [35], the carrier distributions for electrons and holes are defined as

$$f^{e,n}_\mathbf{k} \equiv \langle a^\dagger_{c,n,\mathbf{k}} a_{c,n,\mathbf{k}} \rangle, \quad f^{h,n}_\mathbf{k} \equiv 1 - \langle a^\dagger_{v,n,\mathbf{k}} a_{v,n,\mathbf{k}} \rangle, \tag{5.3}$$

where n is the subband index. Inserting these into Eq. (5.2) , we get

$$i\hbar \frac{\partial}{\partial t} D = \left(\hbar\Omega - i\gamma_D\right) D + \sum_n \left(G^{c,n} N^{e,n} - G^{v,n} N^{h,n}\right) \ , \tag{5.4}$$

where $N^{\lambda,n} = \sum_\mathbf{k} f^{\lambda,n}_\mathbf{k}$ is the total density within a subband. The last term of Eq. (5.4) should formally contain a $\sum_\mathbf{k} 1$ contribution from the completely filled valance band, but it is typically

included in band structures and thus excluded from phonon dynamics.

In this Chapter, we study which types of charge transfer can generate coherent phonons in quantum heterostructures. As can be directly seen from Eq. (5.4), both electrons and holes enter the source to induce coherent phonon amplitude. In many situations, $G^{e,n}$ and $G^{h,n}$ reach similar values within a single material, especially for longitudinal optical phonons. As a result, when charge neutrality $N^{e,n} = N^{h,n}$ is reached among each subband, the source to coherent phonon amplitude is negligible. However, this scenario changes when electrons and holes are separated into different materials. In this situation, phonons in each layer interact with one type of carriers only. As the strengths of electron–phonon coupling are different in different materials, the source to coherent phonon amplitude can be significant. This makes quantum heterostructures a promising platform for generating coherent phonon amplitude.

5.3 Theoretical methods for photoluminescence

The most common way to detect coherent-phonon oscillations in solids is using pump-probe techniques where transient reflection or transmission is measured. [28, 30, 31] Here, we present another way to detect coherent phonons through the analysis of photoluminescence (PL) spectra of the material. Theoretically, this can be described more simply than the dynamics in pump-probe processes, while fully incorporating the essence of coherent phonon effects. The theoretical method to compute PL for semiconductor heterostructures is based on semiconductor luminescence equations (SLEs) [35]. We briefly introduce the key quantities in SLEs here and more details can be found in Ref. [35]. Microscopically, PL is defined by photon-assisted polarization $\Pi_{\mathbf{k},\mathbf{q},q_z} = \Delta\langle B^{\dagger}_{\mathbf{q},q_z} a^{\dagger}_{v,\mathbf{k}-\mathbf{q}} a_{c,\mathbf{k}}\rangle$, where $B^{\dagger}_{\mathbf{q},q_z}$ is the photon creation operator at in-plane wavevector $\mathbf{q}$ and out-of-plane wavevector q_z for general two-dimensional materials, and $a^{(\dagger)}_{\lambda,\mathbf{k}}$ is the electron annihilation (creation) operator at electron band λ and wavevector $\mathbf{k}$. Photon-assisted polarization is a doublet that describes the correlation of photon and optical polarization of the semiconductor.

Including the effects of coherent phonons that follows from Eq. (5.1), SLEs for photon-assisted

polarization $\Pi_{\mathbf{k},\mathbf{q},q_z}$, photon number $\Delta\langle B^{\dagger}_{\mathbf{q},q_z} B_{\mathbf{q},q_z}\rangle$, and coherent phonon amplitude D read

$$
\begin{aligned}
i\hbar\frac{\partial}{\partial t}\Pi_{\mathbf{k},\mathbf{q},q_z} &= \left(\tilde{E}^{c}_{\mathbf{k}} - \tilde{E}^{v}_{\mathbf{k}-\mathbf{q}} - \hbar\omega_{\mathbf{q},q_z} + 2\left(G^{c}_{0} - G^{v}_{0}\right)\mathrm{Re}[D]\right)\Pi_{\mathbf{k},\mathbf{q},q_z} \\
&\quad - \left(1 - f^{e}_{\mathbf{k}} - f^{h}_{\mathbf{k}-\mathbf{q}}\right)\sum_{\mathbf{k}'} V_{\mathbf{k},\mathbf{k}'}\Pi_{\mathbf{k}',\mathbf{q},q_z} + i\mathcal{F}_{\mathbf{q},q_z} S_{\mathbf{k},\mathbf{q}} + T_{\mathbf{k},\mathbf{q},q_z} \ , \qquad (5.5)
\end{aligned}
$$

$$
\hbar\frac{\partial}{\partial t}\Delta\langle B^{\dagger}_{\mathbf{q},q_z} B_{\mathbf{q},q_z}\rangle = 2\mathrm{Re}\left[\sum_{\mathbf{k}}\left(\mathcal{F}_{\mathbf{q},q_z}\right)^{*}\Pi_{\mathbf{k},\mathbf{q},q_z}\right] \ , \qquad (5.6)
$$

$$
i\hbar\frac{\partial}{\partial t}D = \left(\hbar\Omega - i\gamma_{D}\right)D + \sum_{n}\left(G^{c,n}N^{e,n} - G^{v,n}N^{h,n}\right) \ , \qquad (5.7)
$$

where $\tilde{E}^{\lambda}_{\mathbf{k}}$ is the renormalized band energy for electrons $\lambda = c$ and holes $\lambda = v$, $\hbar\omega_{\mathbf{q},q_z}$ is the photon energy, $V_{\mathbf{k},vk'}$ is the Coulomb matrix element, $\mathcal{F}_{\mathbf{q},q_z}$ is the light–matter coupling constant, and $T_{\mathbf{k},\mathbf{q},q_z}$ is the triplet dephasing. Also, $S_{\mathbf{k},\mathbf{q}} = f^{e}_{\mathbf{k}} f^{h}_{\mathbf{k}-\mathbf{q}} + \sum_{\mathbf{k}'} c_{X}^{\mathbf{q},\mathbf{k}-\mathbf{q},\mathbf{k}'}$ is the spontaneous-emission source including free carriers $f^{e}_{\mathbf{k}} f^{h}_{\mathbf{k}-\mathbf{q}}$ and exciton correlations $c_{X}^{\mathbf{q},\mathbf{k},\mathbf{k}'}$. The stimulated emission source is neglected. Equation (5.6) is photon flux driven by photon-assisted polarization. Here, we compute photon number along the perpendicular direction to the two-dimensional materials $\mathbf{q} = 0$. The triplet term is included via a phenomenological dephasing constant $T_{\mathbf{k},\mathbf{q},q_z} = -i\gamma\Pi_{\mathbf{k},\mathbf{q},q_z}$. Equation (5.5) shows that the coherent phonon amplitude modulates the electronic band gap, when $G^{c}_{0} \neq G^{v}_{0}$ is satisfied. As the coherent phonon amplitude oscillates at phonon frequency [Eq. (5.7)], the change in band gap also oscillates at phonon energy. This oscillating band gap creates sidebands at integer multiples of phonon energy near the zero-phonon line (ZPL). In the following, we compute for the TMDC heterobilayers to evaluate under which condition it is possible to detect these phonon sidebands.

5.4 Coherent phonon sidebands in TMDC heterobilayers

When monolayers of WSe_2 and $MoSe_2$ are stacked together, they form type-II band alignment where the conduction band minimum and valance band minimum are located in different materials. [8] Upon optical excitation in the WSe_2 monolayer, the electrons relax to $MoSe_2$ monolayer due to the lower conduction band energy. The time scale for this process is within 100 fs. [9, 10] In addition, experiments [61] have demonstrated that this ultrathin heterostructure is capable of achieving exceptionally high carrier densities. The large carrier density together with ultrafast separation is expected to create a massive source to coherent-phonon oscillations. In this section, we explore different types of charge-transfer dynamics that can lead to coherent-phonon oscillations in $MoSe_2/WSe_2$ heterobilayers.

5.4.1 Ultrafast charging

As is seen from Eq. (5.7), coherent phonon amplitude oscillates at phonon frequency Ω before its stead state is reached. To analyze the excitation condition needed to generate coherent phonons, we consider a simple model where a single type of charge carriers (either electrons or holes) are excited in the material. Also, the interaction between charge carriers and lattice vibrations in this material is defined by an effective constant G^{eff}. Specifically, we describe the carrier density $N(t)$ using a smooth ramp function

$$N(t) = \frac{N_0}{2}\left[1 + \text{erf}(\frac{t}{\tau})\right] \ , \tag{5.8}$$

where τ is the switching time of the carrier density, and N_0 is the total carrier density. In this case, coherent phonon dynamics can be solved analytically, yielding

$$D(t) = \frac{G^{\text{eff}} N_0}{2\hbar\Upsilon}\left[e^{-i\Upsilon t}\Delta D(t) - D_{\text{shift}}(t)\right] \ , \tag{5.9}$$

where $\Upsilon \equiv \Omega - i\gamma_D/\hbar$ is renormalized oscillation frequency, $\Delta D(t) = e^{-\frac{\Upsilon^2\tau^2}{4}}\left[1 + \text{erf}(\frac{t}{\tau} - \frac{i\Upsilon\tau}{2})\right]$ is the oscillation amplitude, and $D_{\text{shift}}(t) = 1 + \text{erf}(\frac{t}{\tau})$ is a slowly varying shift. As the typical decay time for coherent phonon amplitude is in the range of tens of picoseconds [28–30], which is significantly longer than the duration of phonon oscillation cycle, $\gamma_D \ll \Omega$ is assumed in our analysis. At $t \gg \tau$, the relative amplitude of coherent-phonon oscillation, defined as

$$A_{\text{osc}} = \left|\frac{\Delta D}{D_{\text{shift}}}\right| \ , \tag{5.10}$$

decays exponentially as $A_{\text{osc}} = e^{-\frac{\Omega^2\tau^2}{4}}$. This shows that the oscillation amplitude decays rapidly as the switching time τ increases.

Figure. 5.1 shows the relative oscillation amplitude A_{osc} as a function of the ratio between the switching time τ and the phonon period $T = \frac{2\pi}{\Omega}$. For a short switching time in $\tau < 0.1\ T$, the relative oscillation amplitude approaches one. As τ increases from $\tau = 0.1T$ to $\tau = T$, the oscillation amplitude decreases sharply, reaching $A_{\text{osc}} < 10^{-4}$ at $\tau/T = 1$. For the switching time significantly longer than phonon period $\tau \gg T$, the oscillation amplitude is negligible. This is due to the adiabatic following of the lattice structure with the new equilibrium position when the perturbation is slow enough. Therefore, coherent-phonon oscillations are created only when charge switching time is shorter than phonon period.

In TMDCs, the optical phonon energy is about 40 meV, corresponding to a period of $T = 100$ fs. Based on the analysis above, it is expected that carrier density needs to be switched

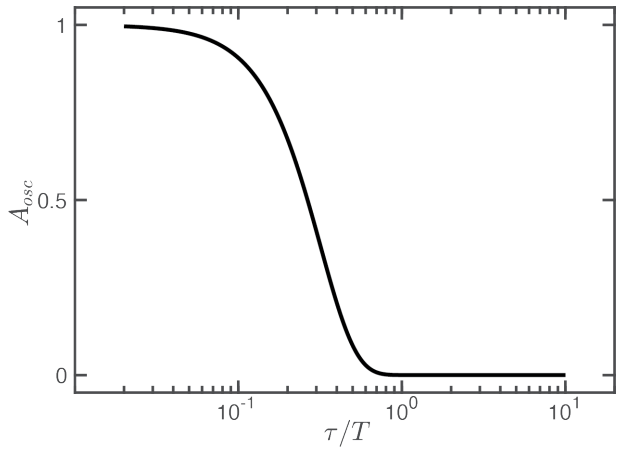


Figure 5.1: Relative oscillation amplitude A_{osc} of coherent phonons as a function of the ratio between charge switch time τ and phonon period T.

on within 100 fs to induce coherent phonons. We compute for $MoSe_2$/WSe_2 heterobilayers under femtosecond optical excitations. Figure. 5.2(a) shows a schematic of the heterobilayers, where the yellow region and blue region represent $MoSe_2$ monolayer and WSe_2 monolayer, respectively. As a reduced model, we include one valance band from the WSe_2 monolayer and two conduction bands, one from each material. The wave functions are approximated in Gaussian basis $\phi_{\pm}(z) = Ne^{-\frac{(z\mp s/2)^2}{\Delta z^2}}$ centered on two sides $z = \pm\frac{s}{2}$ with a separation of $s = 7$Å. Here, N is a normalization constant, and Δz is the width of carrier confinement chosen to be $\Delta z = 5$ Å. The lowest electronic state [light yellow area in Fig. 5.2(a)] is a simple Gaussian centered on the left. For the excited state [light blue area in Fig. 5.2(a)], a linear combination $\phi(z) = \phi_{-}(z) + c\phi_{+}(z)$ is used to approximate the wave function, where the constant c is chosen to ensure its orthogonality with the ground state. We compute for optical excitations at 250 meV above the 1s-exciton energy of WSe_2 monolayer. Due to the extended electronic wave functions, the dipole matrix element for the interlayer excitation is nonvanishing and electrons are excited to the $MoSe_2$ monolayer as well. We assume all the excited holes remain in WSe_2 monolayer. This creates immediate local charging with excess electrons in $MoSe_2$ monolayer and holes in WSe_2 monolayer.

We compute for different pump durations τ and adjust pump field strengths so that the total carrier density is the same for different pump durations. Figure 5.2(b) shows the increase in electron density in the $MoSe_2$ monolayer with pump durations $\tau = 10,\ 40,\ 100$ fs. The total electron density reaches $N = 3 \times 10^{12}$ cm^{-2} after the pump pulse. The electrons in the $MoSe_2$ monolayer interact with phonons in this material, without compensation from the contribution of holes. Based on electron–phonon matrix elements (data from Matthias Florian), we compute the coherent phonon amplitude for optical phonon and its changes to the band energies in the

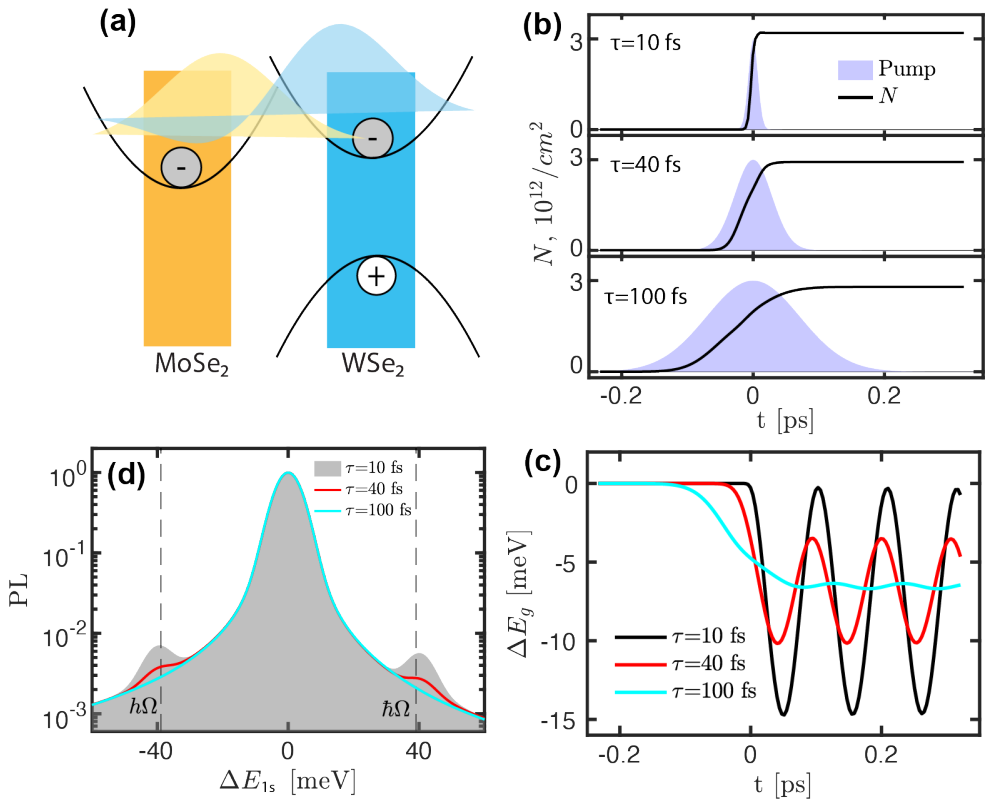


Figure 5.2: **Coherent phonon sidebands in $MoSe_2$/WSe_2 heterobilayers with ultrafast charging.** (a) Schematic of $MoSe_2$/WSe_2 heterobilayers, including the lowest conduction band in each material and a single valance band from WSe_2 monolayer. The electron wave functions for two conduction bands are shown in shaded areas. (b) Electron density in $MoSe_2$ monolayer (black lines) with pump durations τ=10 fs (top row), 40 fs (middle row), and 100 fs (bottom row). (c) Band gap oscillations and (d) PL near 1s-exciton energy with different pump durations.

$MoSe_2$ monolayer. Fig. 5.2(c) shows the change in band gap, denoted as ΔE_g, at different pump durations. As pump duration increases from $\tau = 10$ fs to $\tau = 40$ fs, the oscillation amplitude of the band gap decreases from 7.1 meV to 3.5 meV. Further increasing pump duration to $\tau = 100$ fs reduces gap oscillation to negligible levels. This is consistent with the analytics discussed above that the coherent-phonon oscillation is only generated when the carrier switching time is shorter than the phonon oscillation cycle.

Figure 5.2(d) shows computed PL spectra for the interlayer exciton at different pump durations. We include only free carriers in the spontaneous emission source for simplicity. The dephasing of photon-assisted polarization is set to be $\gamma = 2$ meV. In addition, we include an inhomogeneous broadening of 5 meV. For pump durations $\tau = 10$ fs and $\tau = 40$ fs, sidebands at the phonon energy $\hbar\Omega$ on both sides (vertical dashed lines) of the main peak are visible. The intensities of these sidebands decrease as pump duration increases. For the duration increases to $\tau = 100$ fs,

there is only ZPL at 1s-exciton energy. Therefore, sidebands occur at optical phonon energy on both sides of the resonance and are visible when the local charging is created on a shorter time scale than the phonon oscillation cycle.

5.4.2 Long-lived carrier oscillations

In Sec. 5.4.1, we explored coherent phonons generated by a rapid increase in carrier density, where this density is approximated by a smooth ramp. While such a gradual increase in carrier density is typical in the excitation of a single material, the dynamics of carrier densities in heterostructures tend to be more complex. Here, we examine a scenario where a small amount of carriers oscillate between two different materials. This scenario is a conceptual model designed to mimic the way carrier density oscillations resemble lattice vibrations. Specifically, we approximate the electron density within one layer of the heterostructure using

$$N(t) = N_0 \left[\frac{1}{2} \left(1 + \mathrm{erf}(\frac{t}{\tau}) \right) + r\ e^{-\frac{t^2}{\tau^2}} \cos(\omega t) \right] , \tag{5.11}$$

where the second tern describes carrier oscillation with a relative amplitude r with respect to total carrier density. We assume this oscillation term follows a Gaussian envelope with the duration τ, which is defined by pump duration. The resulting coherent phonon amplitude has the same form as Eq. (5.9) except that the oscillating term is replaced by

$$\Delta D(t) = -i\ r\sqrt{\pi}\ \Omega\tau e^{-\frac{\tau^2(\omega+\Omega)^2}{4}} \left(1 + e^{\Omega\omega\tau^2} \right) , \tag{5.12}$$

when pump duration $\tau \gg \frac{1}{\Omega}$. For resonant oscillations $\omega = \Omega$, the relative amplitude of coherent phonon as defined in Eq. (5.10) becomes

$$A_{\mathrm{osc}} = \frac{r\ \sqrt{\pi}\Omega\tau}{2} , \tag{5.13}$$

showing a linear increase in the oscillation amplitude with the pump duration τ.

Figure 5.3 shows the amplitude of coherent-phonon oscillation A_{osci} as a functionn of pump duration τ. The amplitude of carrier density oscillation is set to $r = 10^{-5}$ (black line), $r = 10^{-4}$ (red line), and $r = 10^{-3}$ (cyan line). In the case where $r = 10^{-5}$ (black line), the oscillations of coherent phonons are negligible. At $r = 10^{-4}$ (red line), the amplitude of phonon oscillation reaches a vlaue $A_{\mathrm{osc}} = 0.16$ at $\tau = 30$ ps. When the value of r is increased to 10^{-3}, there is a significant rise in the amplitude of coherent-phonon oscillations. In this case, the amplitude of these oscillations reaches $A_{\mathrm{osc}} > 1$ when $\tau > 20$ ps. This time scale is much longer than the typical phonon oscillation cycle ($T < 1$ ps). Our analysis shows that when $r > 10^{-4}$, the

oscillations in charge carriers can induce oscillations in coherent phonons. Furthermore, the magnitude of these coherent-phonon oscillations increases with pump duration. This process can be driven over a time scale that is significantly longer than the cycle typically associated with optical phonons.

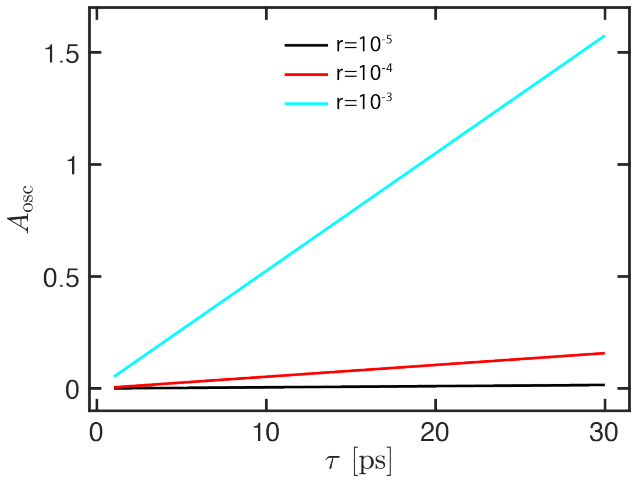


Figure 5.3: Amplitude of coherent-phonon oscillations as a function of pump duration τ, at selected ratios $r = 10^{-5}$ (black line), $r = 10^{-4}$ (red line), $r = 10^{-3}$ (cyan line) representing the fraction of total carrier density that oscillates at phonon frequency.

In the following, we demonstrate the effects of carrier oscillation in $MoSe_2/WSe_2$ heterobilayers. The microscopic mechanism of charge transfer is not discussed here as it is beyond the focus of this study. Instead, we approximate the carrier density $N(t)$ in the $MoSe_2$ monolayer using harmonic-oscillator model

$$\frac{\partial^2}{\partial t^2}N = -\Omega^2 N - \gamma\frac{\partial}{\partial t}N + \frac{\partial}{\partial t}S\,, \tag{5.14}$$

where the characteristic frequency ise set to be phonon frequency Ω, γ is the phenomenological dephasing, and S is the driving source of carrier density. Specifically, we use $S(t) = \frac{1}{e^{-\frac{t}{\tau}}+1} + r_g\ e^{-\frac{t^2}{\tau^2}}\cos(\Omega t)$ where the first term is a smooth ramp as an effective model for optical excitation with pump duration τ, and the second term oscillates at phonon frequency with a relative amplitude $r_g \ll 1$. We refer this second term as phonon-coupled oscillations in the following. The duration of the pump pulse τ is chosen to be significantly longer than phonon period to eliminate the effects from ultrafast charging as discussed in Sec. 5.4.1.

Figure 5.4(a) shows the electron density in the $MoSe_2$ monolayer without ($r_g = 0$, shaded area) and with ($r_g = 10^{-5}$, red solid line) phonon-coupled oscillations, during a pump pulse which reaches its peak at $t = 0$. As the difference between carrier densities in these two cases

is small, we also plot the amplitude of carrier oscillation relative to the total carrier density in the red dashed line. This amplitude reaches a maximum value of $A_{\rm osc} = 5 \times 10^{-3}$ at $t = 0$. Figure 5.4(b) shows the corresponding coherent-phonon oscillations, manifested as the change in band gap. The amplitude of band gap oscillation reaches a few meV as carrier density reaches $N^e = 10^{12}$ cm^{-2}. The inset in Fig. 5.4(b) is a zoomed-in plot of ΔE_g near $t = 20$ ps indicated in blue shaded area in the main frame, showing ΔE_g oscillating periodically at the phonon cycle of 100 fs. This change in band gap vanishes when the phonon-coupled oscillation is switched off ($r_g = 0$, black line).

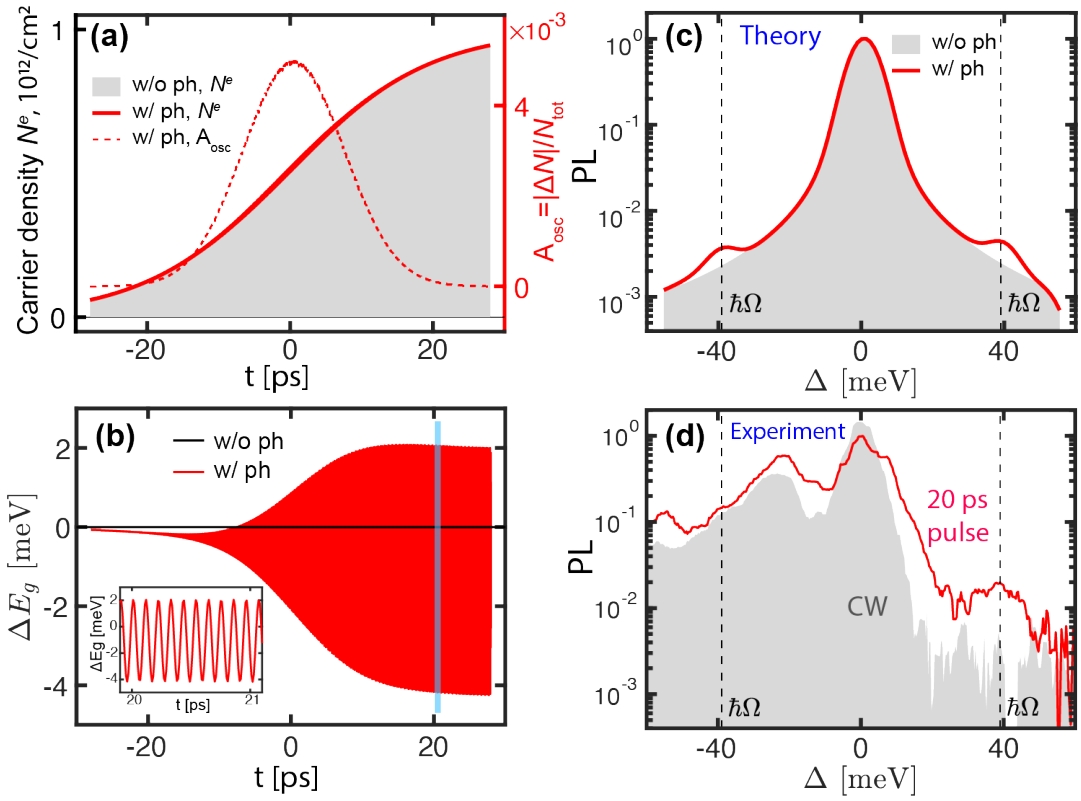


Figure 5.4: **Coherent phonon sidebands induced by phonon-coupled carrier oscillations.** (a) Carrier density N^e in the $MoSe_2$ monolayer without (shaded area) and with (red solid line) phonon-coupled carrier oscillations. The red dashed line shows the amplitude of the oscillations in carrier density relative to total density. (b) Change in band gap without (black line) and with (red line) phonons. The inset shows a zoomed-in plot in the time window indicated by blue area in the main frame. (c) Computed PL near 1s-exciton energy without (shaded area) and with (red line) phonon-coupled oscillations. The vertical dashed lines indicate phonon energies relative to ZPL. (d) Experimental data of PL in $MoSe_2/WSe_2$ heterobilayers under the excitation by a continuous-wave laser (black line) and a 20 ps pump pulse (red line).

Figure 5.4(c) shows the corresponding PL spectra of $MoSe_2/WSe_2$ heterobilayers near the 1s-

exciton energy. We assume a constant dephasing $\gamma = 1$ meV and include 5 meV inhomogenous broadening. Compared to a single peak at 1s energy without phonon-coupled oscillations (shaded area), sidebands emerge on both sides of the main peak when phonons are included (red line). The amplitude of sidebands relative to the main peak reaches 4×10^{-3}. Figure 5.4(d) shows preliminary experimental data (Parag Deotare) of the PL in $WSe_2/MoSe_2$ heterobilayers excited by a continuous-wave laser (shaded area) and a 20 ps pump pulse (red line). The bilayer has a twist angle of 54° and the measurement is done at the temperature of $T = 4$ K. The side peak on the low-energy side at $\Delta = -20$ meV is due to phonon-assisted emission from the indirect exciton [11]. On the high-energy side, a sideband at $\Delta = 40$ meV emerges when excited by the 20 ps pump pulse but is negligible under continuous-wave excitation. As the energy of this sideband is close to optical phonon energy, our computation shows the possibility of coherent sidebands as a result of carrier oscillations between the bilayers. While further investigations are needed to confirm the origin of this sideband, our theory prediction shows the possibility of coherent phonon driven by long-lived carrier oscillations. Further, as the generation of coherent phonons is directly connected to charge-transfer dynamics, these spectroscopic features of coherent phonons hold the potential for monitoring charge-transfer dynamics in quantum heterostructures.

5.5 Conclusion and outlook

In conclusion, we presented the mechanism of coherent-phonon oscillations and the corresponding phonon sidebands in photoluminescence (PL) of semiconductors. Compared to bulk materials, this phenomenon can be more readily observed in heterostructures due to the presence of local charging. Specifically, we explored which type of charge-transfer dynamics in heterostructures can produce coherent-phonon oscillations. Our studies reveal that coherent phonons can be generated in two scenarios: 1) ultrafast charging that occurs on the times scales shorter than phonon oscillation cycles; and 2) long-lived oscillations in carrier density where the oscillation frequency occurs at optical phonon frequency. As a result of coherent-phonon oscillations, the band gap is modulated at the phonon frequency, which leads to phonon sidebands in PL spectra.

We demonstrated the effects of coherent phonons in type–II aligned $MoSe_2/WSe_2$ heterobilayers. In the first scenario where carrier density is described by a smooth ramp, sidebands are generated only if the charge switching time is shorter than 100 fs. In the second scenario where a small fraction of charge carriers oscillate at phonon frequency, sidebands can be generated with pump pulses of the durations of tens of picoseconds. Further work is needed to confirm coherent phonon sidebands in experiments. This includes examining the effect of various factors such as the strength, duration, and frequency of the pump pulses. As coherent phonons exhibit unique spectral features, they can be valuable for observing and understanding charge-transfer processes

in quantum heterostructures.

CHAPTER 6

Hyperspectral Absorption of Semiconductor Monolayer Crystals

This Chapter is mainly adapted from Q. Wen, Y. Wu, P. Wang, D. Laleyan, D. Bayerl, E. Kioupakis, Z. Mi, and M. Kira, *Hyperspectral absorption of semiconductor monolayer crystals*, Appl. Phys. Lett. **116**, 181103 (2020).

6.1 Introduction

Semiconductors that can absorb light across the entire solar spectrum are highly sought after for applications in photodetectors, solar cells, and artificial photosynthesis. Equally important is the efficient charge-carrier separation to reach high photon-to-electron conversion efficiency. In this regard, nanostructures are particularly advantageous due to their capabilities for carrier transport at the nanoscale. Atomically thin III-nitrides, an emerging class of quantum materials with direct band gap tunable via adjusting thicknesses and materials compositions, is a promising candidate. Here, we focus on hyperspectral absorption that we quantify to be 50% or more over spectral range covering several eV.

In semiconductors, light absorption creates electrons to the conduction band and holes (vacancies) to the valence band. The Coulomb attraction can bind them into excitons, with the 1s exciton having the lowest energy. After their optical excitation, coherent 1s excitons decay radiatively via light–matter coupling or non-radiatively via disorder-, Coulomb-, and phonon-interaction induced dephasing γ. The radiative decay $\Gamma \propto 1/(a_B)^2$ is inversely proportional to exciton radius a_B squared for effectively two-dimensional excitons.[62] Generally, the ratio of γ and Γ defines the strength of the excitonic absorption, and the maximum absorption is detected when γ and Γ are equal[62]. The specific material determines Γ and it often is too small to realize strong-absorption condition $\gamma = \Gamma$ although γ can be tuned with either the temperature or electron–hole density. Since Γ increases with shrinking confinement, $\Gamma \to \gamma$ is easiest to reach at the limit of

a single atomic layer, monolayer, which already is standard for transition metal dichalcogenides (TMDCs)[63]. Indeed, an hBN-encapsulated TMDC monolayer has been demonstrated to produce radiative-limited linewidth of few meV.[64–66] Nearly 100% [67, 68] excitonic absorption has been measured for $MoSe_2$ monolayer with a mirror next to monolayer, but only close to a 2 meV-wide absorption peak, far from being hyperspectral. We have recently predicted[69] and demonstrated[70, 71] a new class of room-temperature quantum materials – GaN monolayers that exhibit exciton binding comparable to TMDCs while being the only known materials whose energy band edges straddle water redox potentials. This makes nitride monolayers an exciting candidate for efficient solar-fuel generation.

We present strategies to extend high-absorption bandwidth from few meV to 2 eV based on TMDC and III-nitride monolayers as well as GaAs quantum wells to cover a broad range of design possibilities. We will introduce monolayer arrays that consists of *different* monolayers separated by barriers with thickness L [Fig. 1(a)] and position the structure in front of a mirror.

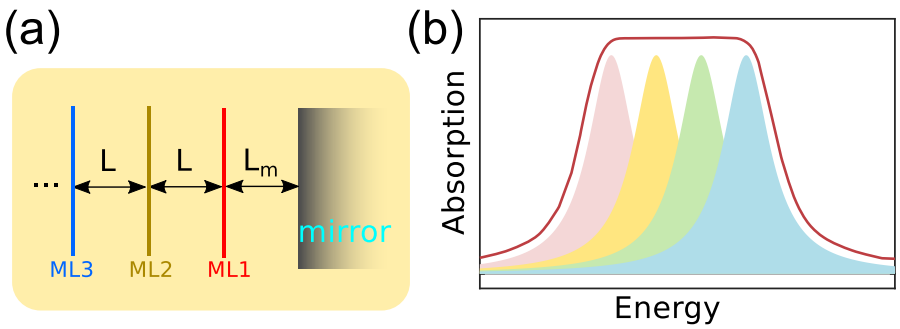


Figure 6.1: (a) Color-chirped monolayer (ML) array near a mirror. The barriers between monolayers have a thickness L, and a mirror is distance L_m away from the first monolayer. (b) MLs color chirped to have *different* excitonic resonances, producing a broadband absorption.

By changing the exciton energy of each monolayer to be partially overlapping, we expect to increase the bandwidth of the collective absorption as illustrated in Fig. 1(b). Since this involves a changing exciton energy with position, we call this approach as color chirping. Our results suggest that the excitonic absorption can be combined with multilayer-enhanced continuum absorption to produce hyperspectral absorption without the need to compromise the ideal photovoltage.

6.2 Many-body theory for linear absorption in semiconductors

We fully describe may-body aspects of monolayers with the semiconductor Bloch equations systematically coupled to the Maxwell equations, following the discussion in Ref. [62, 72]. Since the sunlight is weak in terms of semiconductor nonlinearities, it is sufficient to analyze the linear response defined by a dimensionless susceptibility $\xi(\omega)$. That defines the absolute absorption of light, $\alpha(\omega) = 2\text{Im}[\xi(\omega)]/|1 - i\xi(\omega)|^2$, for a free-standing monolayer[62]. The properties of 1s-exciton absorption alone can be understood from its linear susceptibility [62]

$$\xi_{1s}(\omega) = \frac{\Gamma_{1s}}{E_{1s} - \hbar\omega - i\gamma(\omega)} \ , \tag{6.1}$$

where Γ_{1s} defines the radiative decay of 1s excitons having energy $E_{1s} = \hbar\omega_{1s}$. The full many-body description introduces Coulomb- and phonon-interaction induced dephasing $\gamma(\omega)$ that eventually depends on exciton state and light frequency.[62] At the 1s resonance $\omega = \omega_{1s}$, the linear susceptibility reduces to $\xi(\omega_{1s}) = i\Gamma_{1s}/\gamma \equiv i/r$, which yields 50% peak absorption at $\gamma = \Gamma_{1s}$, following[62] from $\alpha_{\text{peak}} = \frac{2\gamma\Gamma_{1s}}{(\gamma+\Gamma_{1s})^2} = \frac{2r}{(1+r)^2}$ for a general ratio r of non-radiative and radiative dephasing. The 1s energy defines a wavelength λ_{1s}, and adding a mirror at $\lambda_{1s}/4$ distance from the monolayer doubles the radiative decay $\Gamma_{\text{eff}} = 2\Gamma$, halves $r = \gamma/\Gamma_{\text{eff}}$, and doubles $\alpha_{\text{peak}} = \frac{4r}{(1+r)^2}$ peaking at 100% for $\gamma = \Gamma_{\text{eff}}$, as measured recently[67, 68].

Since Coulombic enhancement of light–matter interaction is weak for excitonic continuum states, their radiative coupling is equally weak. The corresponding ratio $r_{\text{cont}} \equiv \text{Re}[i/\xi(\omega_{\text{cont}})] \propto 1/\alpha(\omega_{\text{cont}})$ is large producing only a weak continuum absorption $\alpha(\omega_{\text{cont}})$, evaluated at $\hbar\omega_{\text{cont}}$ matching the energy of the continuum states. In typical semiconductors, $\xi(\omega_{\text{cont}})$ and thus a single layer $\alpha(\omega_{\text{cont}})$ is one-to-two orders of magnitude smaller than for 1s. However, it is well known that radiative coupling among multiple quantum wells strongly modifies the absorption[73, 74] through significantly altered effective r. Additionally, radiative coupling among multiple quantum wells can produce new spectral resonances [75] not describable by the Beer's law.

6.3 Artificial studies of multilayer absorption

We first analyze multiple monolayers, all positioned at the same location, $\lambda_{1s}/4$ spacing away from a mirror. This artificial study approximates[74] monolayer arrays with inter-monolayer spacing much smaller than the resonance wavelength $L \ll \lambda_{1s}$. Our system has an exciton binding energy $E_B = 267$ meV and radiative coupling $\Gamma_{1s} = 0.9$ meV matching a typical TMDC monolayer [64–66, 76]. The total dephasing is the sum of Coulomb- and phonon-scattering in-

duced dephasing, and we analyze a realistic case with $\gamma_{1s} = 2$ meV and $\gamma_{\lambda\neq 1s} = 4\gamma_{1s}$, due to the diffusive nature Coulomb scattering[77]. We also add $\gamma = \gamma_\lambda + 10$ meV due to room-temperature phonons[78]. Figure 6.2(a) shows the absorption spectra of 1 (shaded area), 10 (black line) and 120 (red line) TMDC-type monolayers as function of photon detuning $\Delta \equiv \hbar\omega - E_{1s}$ with respect to the 1s energy E_{1s}. We see that while the absorption near the 1s energy increases from 1 to 10 monolayers, it significantly drops for 120 monolayers. At the same time, the continuum absorption increases to reach nearly perfect absorption over a broadband.

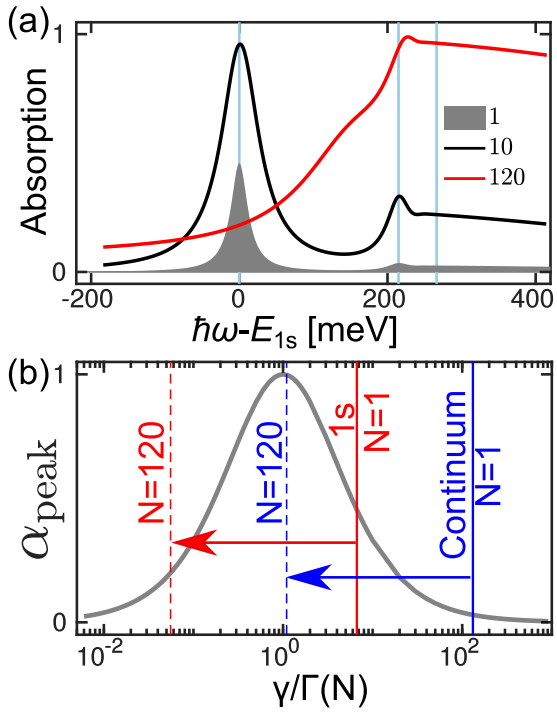


Figure 6.2: (a) Absorption of N=1, 10, 120 TMDC-type monolayers at $\lambda_{1s}/4$ distance from a mirror. Blue vertical lines mark the 1s, 2s, and continuum energies. (b) Absorption peak as a function of $r(N) = \gamma/\Gamma(N)$.

As discussed above, the 1s and continuum absorption have a very different radiative Γ_λ and thus $r_\lambda = \gamma/\Gamma_\lambda$ that defines the corresponding peak absorption $\alpha_{\rm peak}$. Having N monolayers at the same position increases $\Gamma_\lambda(N) = \Gamma_\lambda N$ linearly as function of N while a more general monolayer spacing introduces additional coupling effects analyzed later in Figs. 3–4. The pure $\Gamma_\lambda(N)$ effects always decrease r_λ for increasing N, which produces $r(N) = \frac{\gamma}{N\Gamma_\lambda} = \frac{r(1)}{N} \propto \frac{1}{N}$ such that we can determine the peak absorption from an effective $\alpha_{\rm peak}$ vs. $r(N) = \gamma/\Gamma(N)$ curve shown in Fig. 2(b). As discussed after Eq. (6.1), perfect absorption emerges at $r(N) = 1$

implying that a system having

$$N_D \equiv r(1) = \frac{\text{Non-radiative decay}}{\text{Radiative decay @ } N=1} \tag{6.2}$$

monolayers produces perfect absorption. Our TMDC example has $r_{1s}(1) = 6.7$ and $r_{\text{cont}}(1) = 125$, yielding a high $\alpha_{\text{peak}} = 0.45$ (red solid line) and low $\alpha_{\text{peak}} = 0.03$ (blue solid line) for the $1s$ and continuum states, respectively. Since $r(N)$ decreases with increasing N, both cases can be brought toward the perfect absorption by increasing N towards $N_D = r(1)$. However, if N is increased further, the absorption starts to droop, producing a significant decrease in absorption as N is elevated further. For this system, we find the droop-point N_D=6.7 for the $1s$ resonance and N_D=125 for the continuum states. These numbers explain why $1s$ absorption in Fig. 6.2(a) increases from N=1 to N=10 and then droops for the N=120 whereas continuum absorption continuously improves all the way to N=120.

6.4 Strategy towards hyperspectral absorbers

Reaching hyperspectral absorption through $1s$ absorption is limited because while $1s$ absorption is strong, it remains spectrally narrow and droops faster for elevated N. At the same time, continuum absorption intrinsically covers a broad spectral range and its absorption level can be increased continuously up to a very large N, to eventually reach hyperspectral absorption. As a further advantage, light absorption to continuum states creates unbound electron–hole pairs which can be directly harvested as free charges, unlike excitons created by the $1s$ absorption [77]. Since excitons do not participate in currents, they must be dissociated into free carriers before useful for solar-cell or photo-detection applications, which adds a new design complication. We therefore conclude that hyperspectral absorption can and should be optimized with respect to continuum absorption.

Since the continuum-absorption-based (CAB) hyperspectral absorbers typically need a large N, it is unlikely that the total thickness can be made much smaller than λ. This inevitably introduces coupling effects beyond modifying only $\Gamma_\lambda(N)$. To identify the effect of nontrivial coupling effects on CAB absorbers, we compare N=120 monolayer absorption when they are positioned at L=0, L=10 nm, and L=$\lambda_{1s}/2$ spacing in Fig. 3(a), 3(b), and 3(c), respectively. While setting L=0 eliminates nontrivial coupling effects, it is not experimentally feasible, except as a limiting case having L much smaller than the wavelength. Materials parameters are the same as the TMDC-type monolayers studied in Fig. 6.2. The shaded areas show the absorption from all states. We see that while a $1s$ droop appears for L=0, the $1s$ absorption becomes large and extended-band for L=10 nm and splits for L=$\lambda_{1s}/2$. The $1s$ droop for L=0 results from the too strong radiative

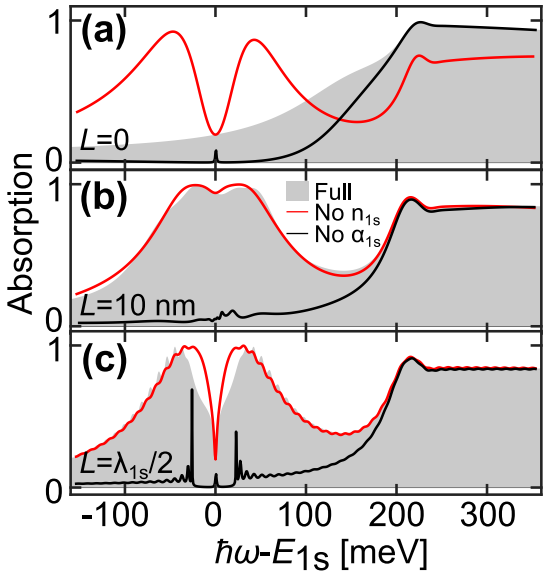


Figure 6.3: Absorption spectra of N=120 identical monolayers positioned at (a) L=0, (b) L=10 nm and (c) L=$\lambda_{1s}/2$ spacing. For each case, the absorption from full states (shaded area) is compared to that without $n_{1s} \equiv \mathrm{Re}[\xi_{1s}]$ (red line) or without $\alpha_{1s} \equiv \mathrm{Im}[\xi_{1s}]$ (black line).

coupling among *all* monolayers as discussed above, which is also true for L=$\lambda_{1s}/2$ at $\hbar\omega$=E_{1s} where all monolayers are coupled in phase. For L=10 nm spacing, the radiative coupling changes it nature because most monolayers couple out of phase and in-phase monolayers form a subset of N. This reduces the number of optimally coupled monolayers and the droop. These phase aspects split the 1s resonance into 90 meV-wide miniband for L=10 nm, although this is not enough to extend high absorption all the way to the continuum, above detuning $\Delta \equiv \hbar\omega - E_{1s} > 267$ meV. At the same time, the continuum absorption itself remains high in all three cases.

To quantify the effect of 1s state on continuum absorption, we compute absorption without the 1s refractive-index $n_{1s} \equiv \mathrm{Re}[\xi_{1s}]$ (red line) or without the 1s absorption $\alpha_{1s} \equiv \mathrm{Im}[\xi_{1s}]$ (black line) contributions in the total ξ, shown in Fig. 6.3. For L=0, the n_{1s} is essential for reaching nearly perfect absorption in continuum because the absorption without n_{1s} (red line) is 15% lower than the full absorption (shaded area) while eliminating only the α_{1s} (black line) reproduces the actual continuum absorption. To explain this unexpected 1s contribution to the continuum absorption, we analyze Eq. (6.1) further. Since ξ_{1s} contributes nonresonantly to continuum frequencies as $\xi_{1s} \propto -\frac{1}{\Delta + i\gamma_{1s}}$, $n_{1s} \equiv \mathrm{Re}[\xi_{1s}]$ contribution is Δ/γ_{1s} times larger than $\alpha_{1s} \equiv \mathrm{Im}[\xi_{1s}]$. As we have $\Delta/\gamma_{1s} = 22$ at $\Delta = 267$ meV, the n_{1s} part dominates the 1s contribution for the continuum. At the same time, negative $n_{1s} \propto -\frac{1}{\Delta}$ means that the 1s state reduces the total refractive index n_{cont} at the continuum, further enhanced by the monolayer number N. Since the actual radiative coupling has a $\Gamma_{\mathrm{eff}} \propto 1/n_{\mathrm{cont}}$ dependence[62], reducing n_{cont} by n_{1s} *increases* continuum's radiative coupling, which explains the enhanced continuum absorption for L=0. When the monolayer

spacing L becomes sufficient, the out-of-phase coupling tends to average out the n_{1s} contributions. Indeed, n_{1s} has very little effect on the continuum part for L=10 nm and L=$\lambda_{1s}/2$ spacing.

These results identify a straightforward strategy to realize hyperspectral absorption, from 1s to continuum: we combine the N-enhancement of radiative coupling for continuum states with color-chirping [Fig. 1(b)] to improve the bandwidth of 1s absorption. Here, we consider color-chirped crystals where the 1s energy of each monolayer changes by about $\Delta E_{1s} = 2\,\Gamma_{1s}$ with respect to the previous one. The crystal itself is positioned $\lambda_{1s}/4$ away from a mirror to enhance absorption further. To cover the design possibilities for different materials, we compute TMDC, nitride, and GaAs representing strong to weak Coulomb interaction. The TMDC parameters are chosen as in Figs. 2–3. We choose a typical GaAs quantum well having 8 nm thickness, 10 meV binding energy, and $\Gamma_{1s} = 25\,\mu$eV [75], as well as nitride monolayers having 200 meV binding energy[69–71] and $\Gamma_{1s} = 0.16$ meV.

With these materials, our designs lead to color-chirped structures with ΔE_{1s} =2, 0.4, 0.05 meV for TMDC, nitride and GaAs-based crystals, respectively. The TMDC crystals have 4 nm thick hBN spacers between each layer. The nitride crystal has 2 nm spacers since 8 monolayers of AlN barrier is sufficient to form the confinement [69]. The GaAs crystals have 20 nm spacers to accommodate reasonably thick quantum wells. To quantify hyperspectral absorption, we determine an average absorption

$$\bar{\alpha} = \frac{1}{E_{\rm hyper}} \int_{E_{1s}}^{E_{1s}+E_{\rm hyper}} dE\; \alpha(E)\;, \tag{6.3}$$

over a hyperspectral energy window defined by $E_{\rm hyper}$. For all cases, we use $E_{\rm hyper} = 2$ eV above the lowest 1s absorption resonance. Fig. 4(a) shows $\bar{\alpha}$ for TMDC (red line), GaAs (black line), and nitride (blue line) crystals as function of N. For all cases, $\bar{\alpha}$ increases monotonically as function of N. Onset to above 80% (50%) $\bar{\alpha}$ is reached at N=120 (60), 240 (100) and 700 (300) for TMDC, GaAs and nitride-based crystals, respectively.

We notice that absorption per monolayer, $\bar{\alpha}/N$, is weakest for nitrides and strongest for TMDCs. This order might be unexpected by comparing the relative strengths of Γ_{1s} of these materials [Γ_{1s}(GaAs) $\ll$ Γ_{1s}(GaN)]. However, while nitrides have a much stronger Coulomb enhancement for the 1s state than GaAs, it becomes weaker for the continuum state. As a result, we find the continuum droop points N_D=290, 560, and 1670 for TMDC, GaAs, and nitride crystal, respectively. Although nitrides require a large N to reach hyperspectral absorbers, they can be tightly packed with a small L due to large barrier provided, e.g. by AlN spacers. With the used example, $\bar{\alpha} = 80\%\,(50\%)$ is reached with 1.5 (0.7) μm thick nitride crystals compared to 0.6 (0.35) μm TMDC and 6.7 (2.8) μm GaAs crystals, respectively. Since trivial reflection from a sample surface can be eliminated with broadband antireflection coating[79], we have assumed

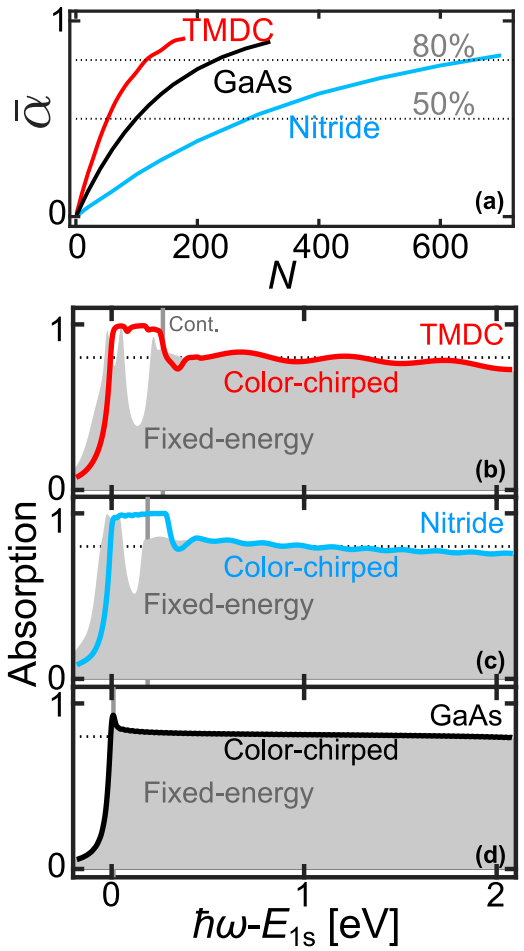


Figure 6.4: (a) Average absorption within 2 eV bandwidth as a function of N. Absorption spectrum of (b) N=120 TMDC monolayers, (c) N=700 nitride monolayers and (d) N=240 GaAs quantum wells, color-chirped (solid line) vs fixed-energy (shaded area) structures.

perfect antireflection coating and have verified that a simple single-layer coating reduces $\bar{\alpha}$ only by 2% for monolayer crystals. At the same time, we have on purpose included continuum absorption of only two bands and expect that these thicknesses are an overestimate because continuum absorption from additional bands should lower the thickness threshold for hyperspectral absorption.

Figures 6.4(b), 6.4(c) and 6.4(d) show the absolute absorption spectrum for TMDC, nitride, and GaAs crystals, respectively. Each case compares color-chirped (solid line) and fixed-energy (shaded area) monolayers to assign the benefits of color-chirping. For TMDC and nitride, color-chirping creates an extended $1s$ flatband and reduces the droop. For GaAs structures, the $1s$ absorption is smaller due to weaker Coulomb and resembles more continuum absorption than for TMDCs and nitrides. These results show that color chirping is only needed for systems with a strong Γ_{1s} whereas CAB-effects yield hyperspectral absorbers for all materials. For the artificial

photosynthesis applications, one can grow a p-type doping gradient[80, 81] to create a built-in electric field that can yield an efficient charge carrier extraction along the lateral dimension of each monolayer. As such, relatively high photovoltage can be maintained for photo-generated charge carriers in each monolayer.

6.5 Conclusion and outlook

In conclusion, we identified a clear design strategy to realize hypersepctral absorption with semiconductor monolayers. By color-chirping the 1*s* resonances, strong and peaked exciton resonances can be converted into a broad flatband absorption. When combined with continuum-absorption based optimization, monolayer crystals can reach high absorption bandwidth of several eV. In III-nitride-based systems, color-chirping can be realized with In and Al alloys to essentially cover the spectral range of sunlight. Our analysis shows that such quantum structures could be two orders of magnitude thinner than those used in existing solar-fuel applications, which should significantly improve the total photon-to-electron conversion efficiency.

Further studies on charge transport properties within monolayer crystals can shed light on the heterostructural design that optimizes the carrier collection efficiency. Additionally, the growing variety of two-dimensional materials, such as van der Waals materials, nitrides, and oxides, offers extensive flexibility in the design of artificial crystals. Extending our theory approaches to study various properties such as ferroelectricity, piezoelectricity, and optical nonlinearities in these stacked quantum materials can be an exciting research direction in the field of quantum materials. Experimentally, future work is needed in the fabrication of artificial crystals beyond a few layers with controlled thickness and large homogeneity. Combining both theory and experimental research efforts on the development artificial crystals is important to the advancement of next-generation quantum devices.

CHAPTER 7

Excitons in Monolayer Hexagonal Boron Nitride

7.1 Introduction

Hexagonal boron nitride (hBN) is a van der Waals material with the band gap in the deep UV range. Even though hBN has a simple crystal structure, the basic property of bulk hBN being an indirect-gap material was only confirmed in recent years [82, 83]. It is intriguing that bulk hBN, despite being an indirect-gap material, exhibits significantly stronger emission compared to the direct-gap AlN [84]. In the limit of a single atomic layer, monolayer (ML) hBN is predicted to have an exciton binding energy of 2 eV [85, 86], an order of magnitude larger than that for transition metal dichalcogenides [7]. Apart from its strong exciton binding, ML hBN exhibits degenerate excitons and distinct optical selection rules that are not found in typical quantum materials. [86] While these nontrivial aspects have been identified through first-principles calculations, there is still a need for a more intuitive understanding of these excitonic properties. One of the challenges in interpreting the *ab initio* data is the random phases in the electronic wave function at different crystal momenta, which makes the symmetry information not easily accessible.

In this Chapter, we analyze the symmetry of excitons in ML hBN and compute its natural linewidth. Based on the Bethe-Salpeter equation (BSE) calculations performed by Woncheol Lee, I introduce an exciton gauge to remove the phase randomness in exciton wave functions and Coulomb matrix elements. This is a crucial step in unveiling the symmetries of excitons. Our results show the importance of complex-valued Coulomb matrix elements and exciton wave functions in obtaining degenerate excitons in ML hBN. In addition, we compute the natural linewidth of ML hBN using semiconductor Bloch equations with electron–phonon interaction included at the microscopic level. Our prediction for the natural linewidth provides an estimate of the absorption linewidth that can be obtained in high-quality samples.

7.2 Excitons in ML hBN

Monolayer hBN has unique excitonic properties, one of which is the degeneracy in excitonic states. [85] Here, we focus on the degeneracy of the 1s excitons. According to first-principles calculations (Woncheol Lee), 1s excitons in ML hBN are degenerate with an exciton binding energy of approximately 2 eV in the ML surrounded by air. The fundamental reason for this degeneracy is not fully understood. The random variation in the phase of the excitonic wave function across different crystal momenta obscures the underlying symmetry of the wave function, which is crucial for understanding the degeneracy in exciton states. In this section, we introduce an exciton gauge to analyze the complex-valued excitonic wave functions, aiming to eliminate the phase randomness typically obtained in *ab initio* calculations.

7.2.1 Symmetry of degenerate excitons

The electronic band energy of ML hBN resembles a double-well energy profile, with equal gap at K and K' valleys. Typically, from the double-well potential, one would expect a symmetric ground state and an antisymmetric excited state. However, the exciton results from Bethe-Salpeter equation (done by Woncheol Lee) show degenerate 1s excitons - the binding energy of the lowest two states in ML hBN are the same $E_{1s} = 1.9$ eV, with a numerical difference less than 170 neV. Figure 7.1(a-b) depicts the absolute value of 1s-exciton wave functions for the ground state $|\phi_1|$ and the first excited state $|\phi_2|$. They both peak at K and K' valleys, with the tail extending significantly along the $K - M$ direction. For the excited state, the amplitude of its wave function $|\phi_2|$ reaches 14% the relative height compared to its peak value at K and K'. This is unlike a typical antisymmetric state where a node is expected at the center between two valleys.

To gain a deeper understanding of exciton symmetry, we analyze the phase of exciton wave function apart from its absolute values. As *ab initio* calculations typically carry random phases from the electronic single-particle wave functions, the exciton wave function also has random phases. It is important to note that the random phase as function of $\mathbf{k}$ is the same for different exciton states [see Appendix B.2 for details]. Based on this, the relative phase between two excitonic states λ, ν can be identified using

$$\theta_{\lambda,\nu} = \frac{1}{i} \ln\left(\frac{(\phi_\lambda)^* \phi_\nu}{|\phi_\lambda \phi_\nu|} \right) . \tag{7.1}$$

Figure 7.1(c) shows cosine of the relative phase between two degenerate 1s-exciton states. Near the K and K' valley, small variations are observed in the phase as function of $\mathbf{k}$. However, there is a phase difference of π between K and K' valleys, shown in the opposite signs of $\cos(\theta_{1,2})$ at

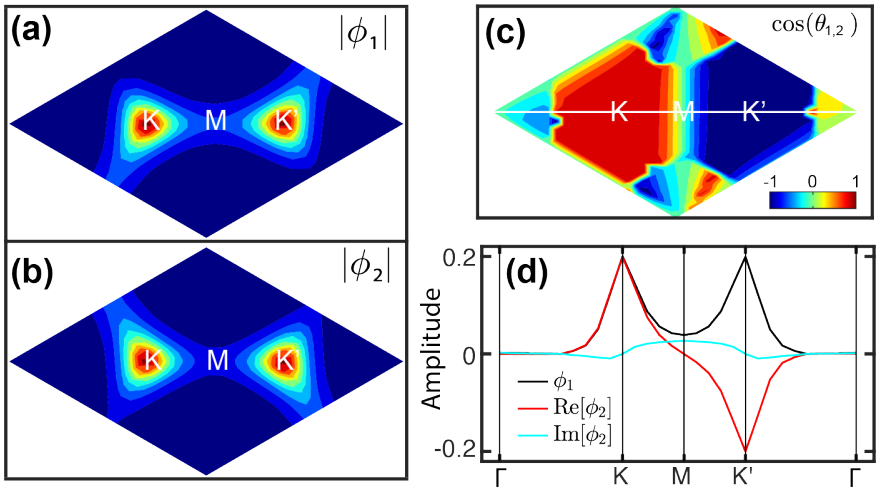


Figure 7.1: **Wave functions for the 1s exciton in ML hBN.** (a-b) Absolute value of exciton wave functions for the degenerate 1s states obtained from GW and BSE calculations (Woncheol Lee). (c) The relative phase $\theta_{1,2}$ of the excited state $\lambda = 2$ with respect to ground state $\lambda = 1$. (d) Phase-smoothed exciton wave functions under exciton gauge along the high-symmetry line.

two valleys. The phases are smooth across most areas in the Brillouin zone, with the exception of the edges where band crossings occur.

To obtain exciton wave functions with smoothed phase, we apply an exciton gauge [details in Appendix B.2] to process the data from BSE. In the exciton gauge, the ground-state wave function ϕ_1 is assumed to have a vanishing phase. This is based on the fact that the ground state has the lowest energy and thus is expected to have the minimal variation in the phase of its wave function. In the following, we denote $\tilde{\phi}_\lambda$ to be phase-smoothed wave function under the exciton gauge. For the ground state 1s exciton, we have

$$\tilde{\phi}_{\lambda=1}(\mathbf{k}) = |\phi_{\lambda=1}(\mathbf{k})| \ . \tag{7.2}$$

Adding the relative phase identified in Eq. (7.1) to the first excited state $\lambda = 2$, we obtain

$$\tilde{\phi}_{\lambda=2}(\mathbf{k}) = |\phi_{\lambda=2}(\mathbf{k})| e^{i\theta_{1,2}} \ . \tag{7.3}$$

Figure 7.1(d) shows the phase-smoothed wave functions for the degenerate 1s excitons along the high-symmetry line. The ground state (black line) is indeed symmetric around the center at M point. For the excited state ϕ_2, the real part (red line) is antisymmetric with a node at $\mathbf{k} = M$. In the meantime, the imaginary part of ϕ_2 (cyan line) shows a finite value at $\mathbf{k} = M$. This leakage in the wave function at the M point, which is shown in the imaginary part of the exciton wave

function, lifts the anti-symmetry of the excited state. Therefore, the nonvanishing wave function ϕ_2 in the middle between K and K' valleys is due to the imaginary part of its exciton wave function.

7.2.2 Phase in Coulomb matrix elements

In the simplest form, Coulomb matrix element of two-dimensional semiconductors is real-valued with its magnitude decaying in momentum space via $V_{\mathbf{k},\mathbf{k}'} \propto \frac{1}{|\mathbf{k}-\mathbf{k}'|}$. However, the presence of nontrivial phases in the excitonic wave functions, as discussed in Sec. 7.2.1, implies that the Coulomb matrix elements in ML hBN are more complicated than this model. To analyze the phase in Coulomb matrix elements, we start with DFT-computed Coulomb matrix elements (data from Woncheol Lee), and remove the random phases using the exciton gauge. Specifically, the phase-smoothed Coulomb matrix elements, denoted as $\tilde{V}_{\mathbf{k},\mathbf{k}'}$, are connected to DFT-computed matrix elements via

$$\tilde{V}_{\mathbf{k},\mathbf{k}'} = V^{\mathrm{DFT}}_{\mathbf{k},\mathbf{k}'} e^{i(\Delta\phi_{\mathbf{k}'} - \Delta\phi_{\mathbf{k}})} , \tag{7.4}$$

where the phase factor is identified from

$$\Delta\phi_{\mathbf{k}} = \frac{1}{i} \ln\left(\frac{\phi_{\lambda=1}(\mathbf{k})}{|\phi_{\lambda=1}(\mathbf{k})|} \right) . \tag{7.5}$$

Figure (7.2)(a-b) shows cosine and sine of the phases $\theta_{\mathbf{k},\mathbf{k}'}$ in the Coulomb matrix elements $\tilde{V}_{\mathbf{k},\mathbf{k}'}$. We fix the first index at one valley $\mathbf{k} = K$, and plot phase variations as a function of $\mathbf{k}'$. In the vicinity of K valley, the value of $\cos(\theta_{\mathbf{k},\mathbf{k}'})$ is approximately one, indicating only small variations in the phase of Coulomb matrix elements. However, near K' valley, a three-fold symmetry pattern emerges in both $\cos(\theta_{\mathbf{k},\mathbf{k}'})$ and $\sin(\theta_{\mathbf{k},\mathbf{k}'})$. This pattern signifies that the phase undergoes a rotation of $2\pi/3$ within each section of this area. Therefore, Coulomb matrix elements exhibit minimal phase variations when considering a single valley. However, they display more significant phase variations when electronic states from different valleys are taken into account.

7.2.3 A reduced model for the phase in Coulomb matrix elements

Due to strong Coulomb interactions in ML hBN, electronic states from different valleys are strongly coupled. Thus, in the studies of ML hBN, the entire Brillouin zone needs to be considered. This poses a challenge to theoretical studies as Coulomb matrix elements between electronic states from different valleys are not described by the simple model, as is discussed in Sec. 7.2.2. In this section, we introduce a reduced model to approximate the phase of Coulomb matrix el-

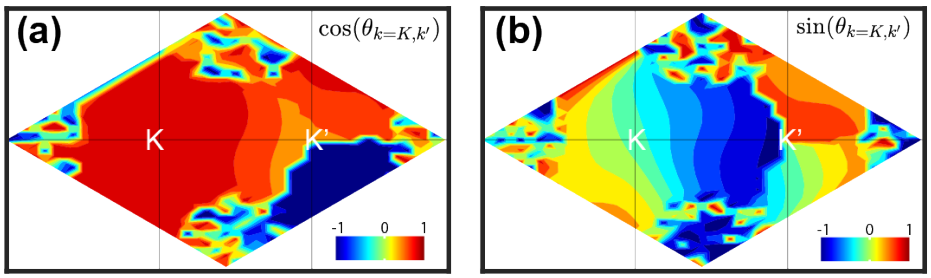


Figure 7.2: **Phase in Coulomb matrix elements under exciton gauge.** (a) Cosine and (b) sine of the phase $\theta_{\mathbf{k},\mathbf{k}'}$ in the Coulomb matrix elements with $\mathbf{k} = K$.

ements. Using this model, we solve excitons in ML hBN using SBE and compare them with the results from BSE (Woncheol Lee).

Since the 1s-exciton wave functions are centered at K and K' valleys, we develop a reduced model for the phase in Coulomb matrix elements based on Gaussian functions centered at K and K' valleys. Specifically, we assume the phase of the form

$$\theta_{\mathbf{k},\mathbf{k}'} = \phi \left[e^{-\frac{|\mathbf{k}-K|^2}{\Delta^2}} e^{-\frac{|\mathbf{k}'-K'|^2}{\Delta^2}} - e^{-\frac{|\mathbf{k}-K'|^2}{\Delta^2}} e^{-\frac{|\mathbf{k}'-K|^2}{\Delta^2}} \right] , \tag{7.6}$$

where ϕ is a prefactor determining the strength of phase difference, and Δ is the width of Gaussian function. This form ensures $\theta_{\mathbf{k},\mathbf{k}'} = -\theta_{\mathbf{k}',\mathbf{k}}$ and thus hermiticity of Coulomb matrix elements. We select the width $\Delta^2 = \frac{l^2}{-\ln\left(\frac{\pi}{\phi}\right)}$ where $l = |K - M|$ is the distance between K and M points such that a phase difference of π between K and M is maintained.

Figure 7.3(a) shows energies of the ground state ($\lambda = 1$, black solid line) and the first excited state ($\lambda = 2$, black dashed line) computed from SBEs, with the phases of Coulomb matrix elements given in Eq. (7.6). As the parameter ϕ is scanned between $\phi = 2.5\pi$ and $\phi = 3.5\pi$, the exciton energies are tunable in a range of 50 meV, showing the impact of the phase in Coulomb matrix elements on exciton energies. At $\phi = 3\pi$, the energy splitting between these two excitonic states reaches a minimum of $\Delta E = 9$ meV. This splitting is negligible compared to the large exciton binding energy of 2 eV in ML hBN. Thus, this reduced phase model effectively produces excitons that are nearly degenerate.

Figure 7.3(b-d) show exciton wave functions for the two lowest excitons along the high-symmetry line. The prefactor in the Gaussian model is chosen to be $\phi = 3.1\ \pi$, indicated by the red line in Fig. 7.3(a). Comparing to the wave functions from BSE results (shaded areas), the reduced model of Coulomb matrix elements computed via SBEs (red lines) predicts the shape of the exciton functions well. The magnitude of the imaginary part of the wave function $\mathrm{Im}[\phi_2]$ at M point computed from the reduced model also agrees with full results. Figure 7.3(e) shows the

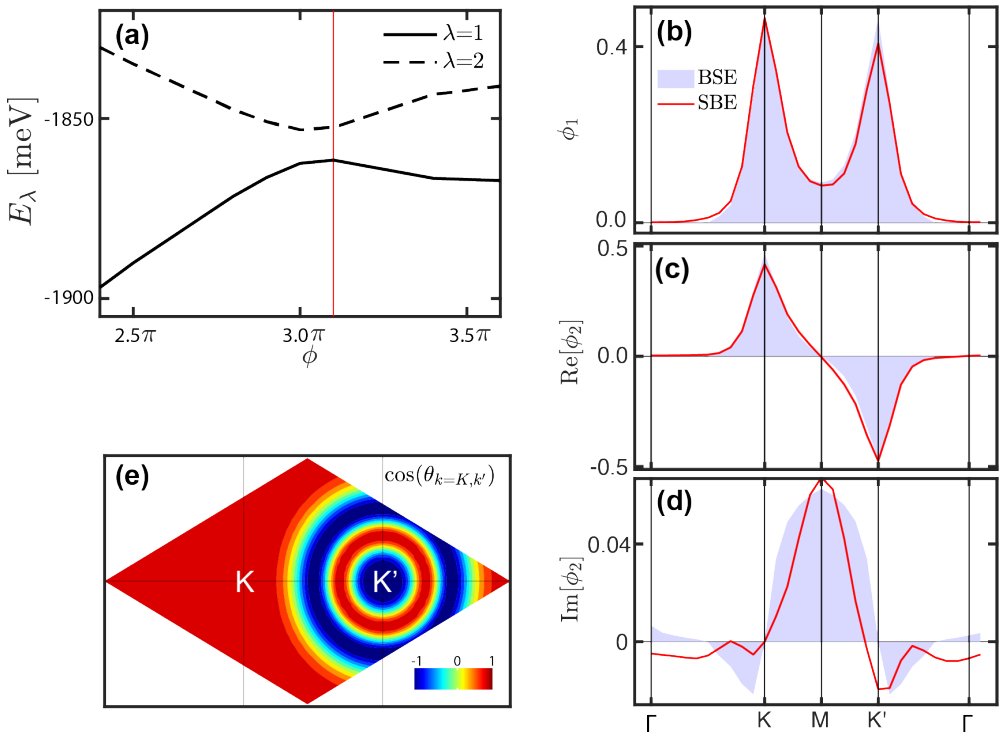


Figure 7.3: **A reduced model for the in Coulomb matrix elements.** (a) Exciton energies of the ground state ($\lambda = 1$, black solid line) and the first excited state ($\lambda = 2$, black dashed line) computed with the Gaussian model. The vertical line indicates the selected parameter for which the wave functions of two lowest excitons are shown in (b-d), comparing results from BSE and that from the reduced model in SBE. (e) Cosine of the phase in Coulomb matrix elements in the reduced model.

cosine of the phase $\theta_{\mathbf{k},\mathbf{k}'}$ in Coulomb matrix elements at $\mathbf{k} = K$. The variation in the phase is negligible near K valley but becomes significant near K' valley. In this case, a phase difference of 1.1π between K and K' points is obtained. Our calculation demonstrate the importance of complex-valued Coulomb matrix elements on exciton energies and wave functions. Future work is needed to understand the underlying reason for the complex-valued Coulomb matrix elements in ML hBN.

7.3 Natural linewidth of ML hBN

In general, the absorption linewidth of semiconductor is affected by several factors, including the radiative coupling, Coulomb and phonon interactions, and inhomogeneous broadening due to defects and variations in the thickness and composition. Currently, the experimentally measured linewidth of ML hBN is about 40 meV. [87] This linewidth is significantly larger than that expected

from the radiative linewidth alone. Therefore, a theory prediction for the natural linewidth including radiative coupling and dephasing is needed. In this section, we start with an overview of the microscopic theory for the absorption of semiconductors with phonons. Then, we compute absorption linewidth of ML hBN at different temperatures.

7.3.1 Elliott formula for absorption with phonons

In SBEs, the Heisenberg equation of motion for optical polarization $P_{\mathbf{k}}$ is [35]

$$i\hbar\frac{\partial}{\partial t}P_{\mathbf{k}} = \tilde{E}^{eh}_{\mathbf{k}}P_{\mathbf{k}} - (1 - f^{e}_{\mathbf{k}} - f^{h}_{\mathbf{k}})\Omega_{\mathbf{k}} + \Gamma^{\text{coul}}_{\mathbf{k}} + \Gamma^{\text{ph}}_{\mathbf{k}} \,, \tag{7.7}$$

where Coulomb and phonon dephasing are introduced via doublet terms $\Gamma^{\text{coul}}_{\mathbf{k}}$ and $\Gamma^{\text{ph}}_{\mathbf{k}}$. Here, we specifically look into phonon doublets $\Gamma^{\text{ph}}_{\mathbf{k}}$, and treat Coulomb doublets via constant dephasing $\Gamma^{\text{coul}}_{\mathbf{k}} = -i\gamma P_{\mathbf{k}}$. At room temperature, phonon broadening is primarily caused by acoustic phonons due to its small energies compared to the thermal energy. For simplicity, we assume the electron–phonon matrix elements for conduction band and valance band differ by a sign flip $G^{c}_{\mathbf{q}} = -G^{v}_{\mathbf{q}}$. To simplify the notation, we denote $G_{\mathbf{q}} = G^{c}_{\mathbf{q}}$ with the superscript omitted in the following. This is a good approximation for hBN as *ab-initio* results (from Woncheol Lee) shows similar magnitude of $|G_c|$ and $|G_v|$ for acoustic phonons. As the exciton–phonon interaction involves compensation between electrons from conduction band and valance band [88], including a sign flip between them provides an upper-bound estimate of the phonon effects.

Microscopically, phonon dephasing is defined via phonon-assisted polarization [89]

$$\Xi^{v,c}_{\mathbf{k},\mathbf{q}} \equiv (G_{\mathbf{q}})^{*}\,\Delta\langle D^{\dagger}_{\mathbf{q}}\, a^{\dagger}_{v,\mathbf{k}-\mathbf{q}_h}a_{c,\mathbf{k}+\mathbf{q}_e}\rangle \,, \tag{7.8}$$

$$\tilde{\Xi}^{c,v}_{\mathbf{k},\mathbf{q}} \equiv G_{\mathbf{q}}\left[\Delta\langle D^{\dagger}_{\mathbf{q}}\, a^{\dagger}_{c,\mathbf{k}-\mathbf{q}_e}a_{v,\mathbf{k}+\mathbf{q}_h}\rangle\right]^{*} \,, \tag{7.9}$$

where $D^{\dagger}_{\mathbf{q}}$ is the phonon creation operator at wavevector $\mathbf{q}$. At the crystal momentum $\mathbf{k}$, the phonon doublets includes phonons across a wide range of wavevector $\mathbf{q}$ via [89]

$$\Gamma^{\text{ph}}_{\mathbf{k}} = \sum_{\mathbf{q}}\left[\Xi^{v,c}_{\mathbf{k}+\mathbf{q}_h,\mathbf{q}} + \Xi^{v,c}_{\mathbf{k}-\mathbf{q}_e,\mathbf{q}} + \tilde{\Xi}^{c,v}_{\mathbf{k}-\mathbf{q}_h,\mathbf{q}} + \tilde{\Xi}^{c,v}_{\mathbf{k}+\mathbf{q}_e,\mathbf{q}}\right] \,. \tag{7.10}$$

The steady-state solution to $P_{\mathbf{k}}$ can be solved in exciton basis [see Appendix C] , which leads to

Elliott formula for absorption with phonons

$$\chi(\omega) = \frac{|d_{vc}|^2}{\epsilon_0} \sum_{\lambda} \frac{|\phi_\lambda^R(r=0)|^2}{E_\lambda - i\gamma - \hbar\omega - z_\lambda^-(\omega) - z_\lambda^+(\omega)} \ , \tag{7.11}$$

$$z_\lambda^\pm(\omega) = \sum_{\mathbf{q}} \frac{(n_\mathbf{q} + \frac{1}{2} \pm \frac{1}{2})|G_\mathbf{q}^{\lambda,\lambda}|^2}{E_\lambda + E_\mathbf{q} \pm \hbar\Omega_\mathbf{q} - i\gamma_T - \hbar\omega} \ . \tag{7.12}$$

Equation (7.12) includes phonon emission $z_\lambda^+(\omega)$ and phonon absorption $z_\lambda^-(\omega)$ terms, where $n_\mathbf{q}$ is phonon occupation, and $G_\mathbf{q}^{\lambda,\lambda'}$ is exciton–phonon matrix element between two exciton states λ, λ' [88]

$$G_\mathbf{q}^{\lambda,\lambda'} = \sum_{\mathbf{k}} \left[\phi_\lambda^L(\mathbf{k})\right]^* \left[G_\mathbf{q}^c \phi_{\lambda'}^R(\mathbf{k} - \mathbf{q}_h) - G_\mathbf{q}^v \ \phi_{\lambda'}^R(\mathbf{k} + \mathbf{q}_e)\right] \ . \tag{7.13}$$

The minus sign indicates the compensation of interaction between electron–phonon $G_\mathbf{q}^c$ and hole–phonon $G_\mathbf{q}^v$, and $\phi_\lambda^{L,(R)}(\mathbf{k})$ is left- (right)-handed exciton wave function. Due to phonon emission processes that is proportional to $(1 + n_\mathbf{q})$, phonon effects are nonvanishing even at zero temperature. We use a constant dephasing γ_T to approximate triplet terms.

7.3.2 Natural linewidth of ML hBN

We apply Elliott formula in Eq. (7.11) to calculate the absorption linewidth of ML hBN. The data for radiative coupling $\Gamma_{1s} = 1.4$ meV and phonon matrix elements are provided by Woncheol Lee. Among three acoustic phonon branches, the longitudinal acoustic (LA) and transverse acoustic (TA) phonons are found to be coupled to electrons. The magnitudes of phonon coupling strength are similar for both the conduction band and valence bands. We use constant G obtained by averaging DFT electron–phonon matrix elements $G_\mathbf{q}^c$ along $\Gamma - K$ direction. The corresponding matrix elements for valance band is chosen to be $G^v = -G^c$ to assess the maximum phonon interaction. The Coulomb dephasing is assumed to be same as radiative linewidth $\gamma = \Gamma_{1s}$, which is typically a lower-bound limit and can be achieved in samples with high quality. We use effective-mass approximation to compute exciton–phonon matrix elements. The effective masses are fit from DFT band structures and averaged along $K - \Gamma$ and $K - M$ directions $m_e = 0.58m_0, \ m_h = 0.53m_0$. We compute for the ML hBN with an exciton binding energy of $E_{1s} = 700$ meV, which is a predicted value when the ML is placed on graphene layers [87]. We assume phonon occupation follows Bose-Einstein distribution $n_\mathbf{q} = \frac{1}{e^{\hbar\Omega/(k_B T)} - 1}$. Also, it is important to note that the triplet dephasing in Eq. (7.12) needs to be treated carefully. The constant γ_T is a reduced model to describe triplet dephasing to phonon doublets. From the general structures of cluster expansion [35], the triplet dephasing has to be larger than doublet dephasing to produce

consistent results. In the following, we choose $\gamma_T = 2\max[\mathrm{Im}[z(\omega)]]$ in the calculation of phonon linewidth.

Figure 7.4(a) shows imaginary part of linear susceptibility near 1s resonance, comparing the absorption without phonon interaction (shaded area) and with phonons (solid lines). As temperature increases from $T = 12$ K to $T = 300$ K, the peak in $\mathrm{Im}[\chi]$ is redshifted with a significantly reduced peak height and an increased broadening. From Eq. (7.11), the peak shift and broadening are connected to real and imaginary part of $z^{\pm}_{\lambda}$, respectively. Figure 7.4(b-c) show the spectra of $z(\omega) = z^{-}(\omega) + z^{+}(\omega)$. As different phonon wavevectors $\mathbf{q}$ are included, the spectra of $z(\omega)$ is highly asymmetric. As temperature increases, the magnitude of $\mathrm{Im}[z]$ at $\Delta = 0$ increases from 3 meV at T=12 K to 22 meV at T=300 K. In addition, Fig. (7.4)(c) shows $\mathrm{Re}[z] > 0$ near 1s resonance, which explains the red shift in exciton energy.

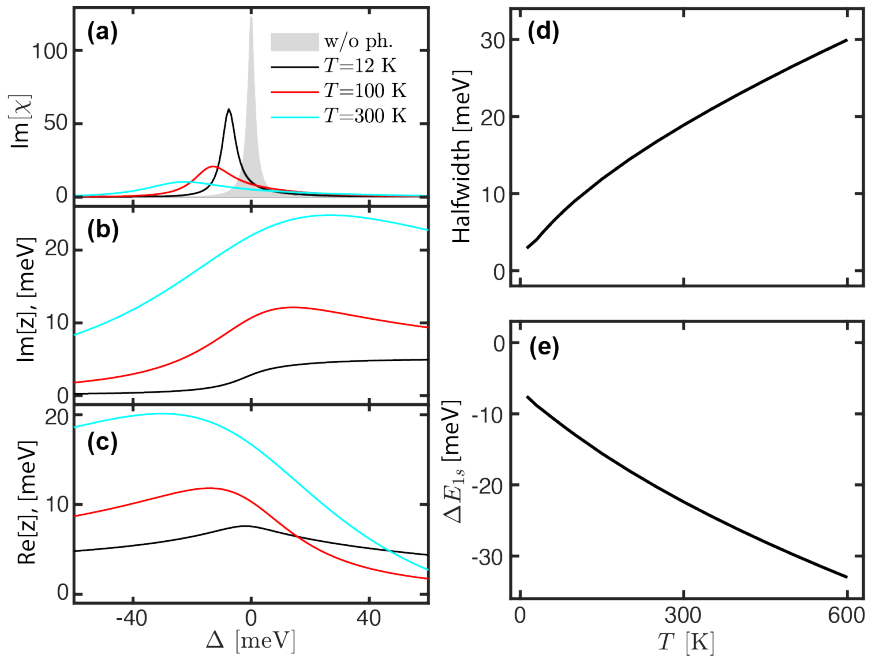


Figure 7.4: **Absorption linewidth and energy shift with phonons.** (a) Imaginary part of linear susceptibility near 1s-exciton energy without phonon (shaded area) and with phonon at $T = 12$ K (black line), 100 K (red line), and 300 K(cyan line). (b) Imaginary part and (c) real part of $z(\omega) = z^{+}(\omega) + z^{-}(\omega)$ using the same color scheme as (a). (d) Halfwidth and (e) energy shift of 1s exciton as a function of temperature.

Figure 7.4(d,e) show the halfwidth and energy shift of 1s exciton ΔE_{1s} as a function of temperature from $T = 12$ K to $T = 600$ K. At $T = 0$, including phonon coupling induces broadening and peak shift due to phonon emission processes. The halfwidth increases sublinearly from 3 meV at $T = 12$ K to 19 meV at $T = 300$ K. This is close to the linewidth predicted for ML $MoSe_2$ [90]. The 1s-exciton energy is shifted by $\Delta E_{1s} = -7$ meV at $T = 12$ K to $\Delta_{1s} = -22$ meV

at $T = 300$ K. The analysis here provides an estimate of natural linewidth of ML hBN that can be achieved when inhomogeneous broadening is negligible. As the low-temperature linewidth computed here is much smaller than that has been realized in experiments [87], our predictions indicates a need for the improvements in growth techniques to reduce inhomogeneous broadening.

7.4 Conclusion and outlook

In conclusion, we examined exciton symmetries in ML hBN by introducing an exciton gauge which eliminates phase randomness in the exciton wave function across different momenta. Our studies reveal the crucial role of the imaginary part of the wave function in creating exciton degeneracy. Additionally, we studied how complex-valued Coulomb matrix elements affect excitonic states by introducing a reduced model for the phase of Coulomb matrix elements. Our calculations demonstrate that by scanning various phase parameters in Coulomb matrix elements, the energies and wave functions of excitons change significantly. This shows the importance of the phase in Coulomb matrix elements in exciton calculations. The importance of complex-valued Coulomb matrix elements identified here motivates further investigations regarding the lattice symmetry and phase of the wave functions.

In addition, we computed the natural linewidth of ML hBN using semiconductor Bloch equations. The halfwidth in the absorption of ML hBN is estimated to be 20 meV at room temperature and a few meV at low temperatures. While this calculation is based on a simple model of band structure and Coulomb matrix elements, the linewidth predicted in our theory provides an approximation of the linewidth that can be attained in samples of high quality. Further studies including full band structures and more systematic Coulomb and phonon matrix elements can provide a more precise value of the natural linewidth than what we have obtained here.

CHAPTER 8

Conclusion

In this Thesis, I have discussed the phenomenon of local charging and its effects on charge-transfer dynamics in quantum semiconductors. In the framework semiconductor Bloch equations (SBEs), I have presented a novel approach that includes local charging effects together with other many-body interactions to accurately compute the motion of charge carriers in semiconductor heterostructures. This approach is then extended to describe the ionic motion during polarization switching in ferroelectric semiconductors. Furthermore, I have explored how the local charging in heterostructures can induce coherent lattice vibrations, which further modify electronic states and produce phonon sidebands in optical spectra. The remaining parts of this Thesis present the absorption of stacked monolayer crystals and degenerate excitons in monolayer hexagonal boron nitrides. Some of the key results from our theoretical computations are summarized in the following, together with implications for future work on quantum materials and quantum technologies.

We have developed an efficient scheme to compute the motion of charge carriers in quantum-well heterostructures, where local charging effects due to electron–hole separation are included. In a type–II aligned quantum-well heterostructure, electrons and holes are excited to opposite sides of the interface when excited by an optical pump resonant at the lowest, spatially indirect state. This spatial separation of electrons and holes creates a charging potential that alters the electronic energies of charge carriers. As a result, electrons and holes accelerate towards the interface to counterbalance the charging. This charging-to-charge-neutral switching gives rise to a unipolar pulse characterized by an electric field that is markedly stronger in one direction than the other. The generation of such unipolar pulses is particularly important for lightwave electronics, where an ultrafast light pulse is applied to control the electron motion within its subcycle. The dominant electric field along one direction enables precise, unidirectional control of quantum state, which holds the potential to beat decoherence in solids and allow room-temperature quantum information processing. The underlying mechanism of these unipolar pulses, as unveiled in our studies, provides guidance on the heterostructure engineering and on the excitation conditions to adjust the pulse shape that is needed for specific experiments. Additionally, the

theoretical approach we have developed is applicable to a wide range of heterostructures where local charging occurs. Extending our approach to more intricate systems, for example, stacked two-dimensional crystals, could enhance insights on charge-transfer dynamics in these systems.

Following our first local charging results, we have extended the charging theory to describe the ionic motion in semiconductor ferroelectric materials. We solve the time-dependent Schrödinger equation for the ionic wave function including many-body Coulomb and phonon interactions. We find that the ultrafast ferroelectric polarization switching at sub-picosecond timescale is enabled by local charging that acts as a positive feedback to the ionic motion. This observation highlights the importance of many-body Coulomb interactions in the switching process. It also sheds light on the key strategies for further quantum materials engineering to enhance the switching speed. For example, tuning the lattice structure and reducing the dielectric constant are potential ways to amplify Coulomb interactions, which could increase the switching speed for high-speed electronics and memories. In addition, this intrinsic switching process illuminates pathways for THz lightwave-driven polarization switching. This could pave the way to developing ferroelectric memories from the present GHz range towards the next-generation THz range. Currently, our theory describes the motion of a single ion within the unit cell, while the remaining charge carriers are reduced to a uniform background. However, the real structural changes that happen during polarization switching are likely more intricate and involve various types of charge carriers. To get a clearer understanding of the switching process, future work could consider the individual motion of different types of ions as well as electrons. This study should offer a more comprehensive picture of the many-body interactions during the switching process.

Apart from its effect on charge-transfer dynamics, we have also discussed how local charging can induce coherent-phonon oscillations in quantum heterostructures. In traditional bulk materials, carrier–phonon interactions from electrons and holes often compensate one another. Semiconductor heterostructure that features separated electrons and holes in different materials display strong phonon effects without this compensation, making it an interesting platform to observe strong coherent-phonon oscillations. We demonstrate the generation of coherent-phonon oscillations in transition metal dichalcogenide heterobilayers. We explore two different charge-transfer mechanisms that can lead to coherent-phonon oscillations: 1) ultrafast charge transfer that occurs faster than phonon oscillation cycles; and 2) long-lived oscillations in charge carriers that occur at the frequency optical phonon. In addition, we discuss how the coherent phonons modulate electronic states, resulting in phonon sidebands in the photoluminescence spectra. The sidebands produced by coherent phonons are indicative not only of lattice vibrations but also serve as markers for charge transfer within the heterostructures. This makes them a potential tool for probing the motion of electrons at the interface of quantum heterostructures. Future research will be needed to confirm the generation of coherent phonons and to establish a clear link

between these spectroscopic features and carrier dynamics within quantum heterostructures.

As a final point, stacking different quantum materials presents a promising method for developing novel functionalities. This is particularly interesting for two-dimensional materials due to their reduced thickness, strong interactions with light, strong excitons at room temperature, and rich interface physics. Aiming at developing ultrabroadband absorbers based on two-dimensional materials, we have outlined the design principles for stacking nitride monolayers to reach nearly perfect absorption over several eV. This is achieved by combining strong, peaked excitonic resonances with the intrinsically broad continuum absorption, leading to hyperspectral absorption that also generates free carriers for efficient collection. This study underscores the critical role of collective coupling in monolayer crystals for enhancing the absorption capabilities. Looking ahead, the creation of artificial crystals presents an exciting frontier in quantum research. The research into combining various properties such as radiative coupling, optical nonlinearity, ferroelectricity, and quantum entanglement in these artificial crystals could lead to breakthroughs in quantum sensing and quantum computing. To effectively design these novel structures, further theoretical studies are essential. These studies should broaden the scope of collective coupling, going beyond the absorption properties and exploring additional functionalities.

APPENDIX A

Energy Conservation with Dynamic Charging

Typically, the total energy of the wave function $E = \langle\phi|\hat{H}|\phi\rangle$ is conserved when the Hamiltonian is static. Here, as the local charging potential has an explicit time dependence, we need to evaluate the energy conservation carefully. We assume the external field to be static so that the time dependence only appears in the charging potential. From Eq. (4.5), the dynamic charging potential is of the form

$$\Delta V(z,t) = -2Q\langle z\rangle z + Q\langle z^2\rangle \ , \tag{A.1}$$

where we simplify the notation by using z for the scaled length $\bar{z}$ in Eq. (4.5). The first term is a linear potential that varies with the position of ion, and the second term adds a constant shift to the potential. As this constant shift does not affect the ionic motion, we neglect the second term for simplicity. The linear potential $\Delta V(z,t) = -2Q\langle z\rangle z$ alone however, does not conserve the energy, as will be shown in the following. To compensate the change in total energy, we add to it a new constant term so that the charging potential becomes

$$\Delta V(z,t) = -2Q\langle z\rangle z + Q\langle z\rangle^2 \ . \tag{A.2}$$

With this charging potential, the time derivative of the total energy becomes

$$\begin{aligned}
\frac{d}{dt}E &= \frac{d}{dt}\langle\phi|\hat{H}|\phi\rangle \\
&= \langle\frac{\partial}{\partial t}\phi|\hat{H}|\phi\rangle + \langle\phi|\frac{\partial}{\partial t}\hat{H}|\phi\rangle + \langle\phi|\hat{H}|\frac{\partial}{\partial t}\phi\rangle \\
&= \frac{i}{\hbar}\langle\phi|\hat{H}\hat{H}|\phi\rangle + \langle\phi|\frac{\partial}{\partial t}\hat{H}|\phi\rangle - \frac{i}{\hbar}\langle\phi|\hat{H}\hat{H}|\phi\rangle \ ,
\end{aligned} \tag{A.3}$$

after inserting the Schrödinger equation $\frac{\partial}{\partial t}\phi = -\frac{i\hat{H}}{\hbar}\phi$ and its complex conjugate. The third line in Eq. (A.3) shows that the first term and the third term are canceled, leaving only the second

term. Given the charging potential in Eq. (A.2), the second term becomes

$$\langle\phi|\frac{\partial}{\partial t}\hat{H}|\phi\rangle = \langle\phi| - 2Q\langle\dot{z}\rangle z + 2Q\langle z\rangle\langle\dot{z}\rangle|\phi\rangle = 0 \ , \tag{A.4}$$

after we denote the average velocity $\langle\dot{z}\rangle = \frac{\partial}{\partial t}\langle z\rangle$. Therefore, the total energy is conserved with the dynamic charging potential in Eq. (A.2).

APPENDIX B

Wannier Equation with General Coulomb

B.1 Wannier equation

Including single-particle energies and Coulomb interaction on the Hartree-Fock level, the Heisenberg equation of motion for optical polarization $P_{\mathbf{k},\mathbf{k}'} = \langle a^\dagger_{v,\mathbf{k}} a_{c,\mathbf{k}'} \rangle$ in a two-band system reads

$$\begin{aligned} i\hbar\frac{\partial}{\partial t}P_{\mathbf{k},\mathbf{k}'} = &\left[E^c_{\mathbf{k}'} - E^v_{\mathbf{k}} - \sum_{\mathbf{l}} \left(V^{v,v,v,v}_{\mathbf{k},\mathbf{l},\mathbf{k},\mathbf{l}}\right)^* f^h_{\mathbf{l}} - \sum_{\mathbf{l}} V^{c,c,c,c}_{\mathbf{k}',\mathbf{l},\mathbf{k}',\mathbf{l}} f^e_{\mathbf{l}}\right] P_{\mathbf{k},\mathbf{k}'} \\ &- \left(1 - f^h_{\mathbf{k}}\right) \sum_{\mathbf{l}} V^{c,v,v,c}_{\mathbf{k}',\mathbf{l}+\mathbf{k},\mathbf{k},\mathbf{k}'+\mathbf{l}} P_{\mathbf{k}+\mathbf{l},\mathbf{k}'+\mathbf{l}} + f^e_{\mathbf{k}'} \sum_{\mathbf{l}} \left(V^{v,c,c,v}_{\mathbf{k},\mathbf{l}+\mathbf{k}',\mathbf{k}',\mathbf{k}+\mathbf{l}}\right)^* P_{\mathbf{k}+\mathbf{l},\mathbf{k}'+\mathbf{l}} \,, \end{aligned} \tag{B.1}$$

where we assume density terms are diagonal $P^{\lambda,\lambda}_{\mathbf{k},\mathbf{k}'} = P^{\lambda,\lambda}_{\mathbf{k}} \delta_{\mathbf{k},\mathbf{k}'}$. In Eq. (B.1), Coulomb matrix elements are connected to single-particle wave functions $\phi_{\lambda,\mathbf{k}}(\mathbf{r})$ in the general form [35]

$$V^{\lambda,\nu,\nu',\lambda'}_{\mathbf{k},\mathbf{p},\mathbf{p}',\mathbf{k}'} = \int d^3r \int d^3r' \left[\phi_{\lambda,\mathbf{k}}(\mathbf{r})\, \phi_{\nu,\mathbf{p}}(\mathbf{r}')\right]^* V(\mathbf{r}-\mathbf{r}') \phi_{\nu',\mathbf{p}'}(\mathbf{r}') \phi_{\lambda',\mathbf{k}'}(\mathbf{r}) \,. \tag{B.2}$$

Following Eq. (B.1), the eigenstates of the homogeneous part can be solved

$$\begin{aligned} \tilde{E}_{\mathbf{k},\mathbf{k}'}\, \phi_\lambda(\mathbf{k},\mathbf{k}') - &\left(1 - f^h_{\mathbf{k}}\right) \sum_{\mathbf{l}} V^{c,v,v,c}_{\mathbf{k}',\mathbf{l}+\mathbf{k},\mathbf{k},\mathbf{k}'+\mathbf{l}} \phi_\lambda(\mathbf{k}+\mathbf{l},\mathbf{k}'+\mathbf{l}) \\ &+ f^e_{\mathbf{k}'} \sum_{\mathbf{l}} \left(V^{v,c,c,v}_{\mathbf{k},\mathbf{l}+\mathbf{k}',\mathbf{k}',\mathbf{k}+\mathbf{l}}\right)^* \phi_\lambda(\mathbf{k}+\mathbf{l},\mathbf{k}'+\mathbf{l}) = E_\lambda\, \phi_\lambda(\mathbf{k},\mathbf{k}') \,, \end{aligned} \tag{B.3}$$

where $\tilde{E}_{\mathbf{k},\mathbf{k}'} = E^c_{\mathbf{k}'} - E^v_{\mathbf{k}} - \sum_{\mathbf{l}} \left(V^{v,v,v,v}_{\mathbf{k},\mathbf{l},\mathbf{k},\mathbf{l}}\right)^* f^h_{\mathbf{l}} - \sum_{\mathbf{l}} V^{c,c,c,c}_{\mathbf{k}',\mathbf{l},\mathbf{k}',\mathbf{l}} f^e_{\mathbf{l}}$ is renormalized band energy. For simplicity, we consider vanishing carrier densities $f^{e(h)}_{\mathbf{k}} = 0$ in the following. Defining polarization with a center-of-mass momentum $\mathbf{Q}$

$$P_{\mathbf{k},\mathbf{k}+\mathbf{Q}} \equiv \langle a^\dagger_{v,\mathbf{k}} a_{c,\mathbf{k}+\mathbf{Q}} \rangle \,, \tag{B.4}$$

and introducing the notation $\phi_{\lambda,\mathbf{Q}}(\mathbf{k}) \equiv \phi_\lambda(\mathbf{k}, \mathbf{k}+\mathbf{Q})$, Eq. (B.3) becomes

$$\left(E^c_{\mathbf{k}+\mathbf{Q}} - E^v_{\mathbf{k}}\right)\phi_{\lambda,\mathbf{Q}}(\mathbf{k}) - \sum_{\mathbf{k}'} V^{c,v,v,c}_{\mathbf{k}+\mathbf{Q},\mathbf{k}',\mathbf{k},\mathbf{k}'+\mathbf{Q}}\ \phi_{\lambda,\mathbf{Q}}(\mathbf{k}') = E_{\lambda,\mathbf{Q}}\ \phi_{\lambda,\mathbf{Q}}(\mathbf{k})\ . \tag{B.5}$$

This is the Wannier equation with general Coulomb matrix elements.

B.2 Random phase removal with exciton gauge

We consider excitons with center-of-mass momentum $\mathbf{Q} = 0$ in this section. We simplify the notation by denoting Coulomb matrix elements $V^{c,v}_{\mathbf{k},\mathbf{k}'} = V^{c,v,v,c}_{\mathbf{k},\mathbf{k}',\mathbf{k},\mathbf{k}'}$ and neglecting $\mathbf{Q}$ index in the exciton wave function. The Wannier equation following from Eq. (B.5) is

$$\left(E^c_{\mathbf{k}} - E^v_{\mathbf{k}}\right)\phi_\lambda(\mathbf{k}) - \sum_{\mathbf{k}'} V^{c,v}_{\mathbf{k},\mathbf{k}'}\ \phi_\lambda(\mathbf{k}') = E_\lambda\ \phi_\lambda(\mathbf{k})\ . \tag{B.6}$$

In general, Coulomb matrix elements $V^{c,v}_{\mathbf{k},\mathbf{k}'}$ can be complex valued. In typical *ab initio* calculations, the electron wave function has random phase $\phi_{\lambda,\mathbf{k}}(\mathbf{r}) = \tilde{\phi}_{\lambda,\mathbf{k}}(\mathbf{r})e^{i\theta_{\lambda,\mathbf{k}}}$, where a tilde is used to denote a quantity having a smooth phase. This random phase $\theta_{\lambda,\mathbf{k}}$ in the electron wave function is carried over to Coulomb matrix elements, yielding

$$V^{c,v}_{\mathbf{k},\mathbf{k}'} = \tilde{V}^{c,v}_{\mathbf{k},\mathbf{k}'}e^{i(\Delta\theta_{\mathbf{k}}-\Delta\theta_{\mathbf{k}'})}\ , \tag{B.7}$$

$$\Delta\theta_{\mathbf{k}} \equiv \theta_{v,\mathbf{k}} - \theta_{c,\mathbf{k}}\ . \tag{B.8}$$

Equation (B.8) shows that only the relative phase between conduction band and valance band is relevant. Further, from Eq. (B.6), it is straightforwards to see that including phases $e^{i(\Delta\theta_{\mathbf{k}}-\Delta\theta_{\mathbf{k}'})}$ to Coulomb matrix elements will impose an extra phase to exciton wave functions

$$\phi_\lambda(\mathbf{k}) = \tilde{\phi}_\lambda(\mathbf{k})e^{i\Delta\theta_{\mathbf{k}}}\ . \tag{B.9}$$

However, as this phase $\Delta\theta_{\mathbf{k}}$ is same for all exciton states λ, the relative phase between wave functions of different excitonic states does not carry this randomness.

In the exciton gauge, we assume the wave function of the ground-state exciton has a vanishing phase

$$\tilde{\phi}_{\lambda=1}(\mathbf{k}) = |\phi_{\lambda=1}(\mathbf{k})|\ . \tag{B.10}$$

This is based on the fact that the ground state has the lowest energy and thus is expected to produce minimal phase variations. Then, the relative phases between conduction band and valance

band can be identified from Eq. (B.9)

$$\Delta\theta_{\mathbf{k}} = \frac{1}{i}\ \ln \frac{\phi_{\lambda=1}(\mathbf{k})}{|\phi_{\lambda=1}(\mathbf{k})|}. \tag{B.11}$$

Based on this, we compute phase-fixed Coulomb matrix elements in the exciton gauge

$$\tilde{V}^{c,v}_{\mathbf{k},\mathbf{k}'} = V^{c,v}_{\mathbf{k},\mathbf{k}'} e^{i(\Delta\theta_{\mathbf{k}'} - \Delta\theta_{\mathbf{k}})}\ , \tag{B.12}$$

which is a smooth function of $\mathbf{k}$ and $\mathbf{k}'$. The generalizations to finite center-of-mass momentum $\mathbf{Q}$ and multiband systems are straightforward.

APPENDIX C

Elliott Formula for Absorption with Phonon

We start with equation of motion for optical polarization [35]

$$i\hbar\frac{\partial}{\partial t}P^{vc}_{\mathbf{k}} = \tilde{E}_{\mathbf{k}}P_{\mathbf{k}} - (1 - f^{e}_{\mathbf{k}} - f^{h}_{\mathbf{k}})\left(d_{vc}E(t) + \sum_{\mathbf{k}'} V_{\mathbf{k},\mathbf{k}'}P_{\mathbf{k}'}\right) + \Gamma^{\text{coul}}_{\mathbf{k}} + \Gamma^{\text{ph}}_{\mathbf{k}} \ , \tag{C.1}$$

where $\tilde{E}_{\mathbf{k}}$ is renormalized band energy, $f^{e(h)}_{\mathbf{k}}$ is electron (hole) density, d_{vc} is dipole matrix elements, $E(t)$ is optical field, and $\Gamma^{\text{coul}}_{\mathbf{k}}, \Gamma^{\text{ph}}_{\mathbf{k}}$ are doublets from Coulomb and phonon interactions. The microscopic form of phonon dephasing is defined via phonon-assisted polarization [89]

$$\Gamma^{\text{ph}}_{\mathbf{k}} = \sum_{\mathbf{q}}\left[\Xi^{v,c}_{\mathbf{k}+\mathbf{q}_h,\mathbf{q}} + \Xi^{v,c}_{\mathbf{k}-\mathbf{q}_e,\mathbf{q}} + \tilde{\Xi}^{c,v}_{\mathbf{k}-\mathbf{q}_h,\mathbf{q}} + \tilde{\Xi}^{c,v}_{\mathbf{k}+\mathbf{q}_e,\mathbf{q}}\right] \ , \tag{C.2}$$

$$\Xi^{v,c}_{\mathbf{k},\mathbf{q}} \equiv (G_{\mathbf{q}})^{*}\,\Delta\langle D^{\dagger}_{\mathbf{q}}\, a^{\dagger}_{v,\mathbf{k}-\mathbf{q}_h}a_{c,\mathbf{k}+\mathbf{q}_e}\rangle \ , \tag{C.3}$$

$$\tilde{\Xi}^{c,v}_{\mathbf{k},\mathbf{q}} \equiv G_{\mathbf{q}}\left[\Delta\langle D^{\dagger}_{\mathbf{q}}\, a^{\dagger}_{c,\mathbf{k}-\mathbf{q}_e}a_{v,\mathbf{k}+\mathbf{q}_h}\rangle\right]^{*} \ , \tag{C.4}$$

where $D^{\dagger}_{\mathbf{q}}$ is phonon creation operator, and $G_{\mathbf{q}}$ is electron–phonon matrix elements. We assume the electron–phonon matrix elements from conduction and valance band differ by a sign flip only $G^{c}_{\mathbf{q}} = -G^{v}_{\mathbf{q}}$ for simplicity and denote $G_{\mathbf{q}} = G^{c}_{\mathbf{q}}$.

The equations of motion for phonon-assisted polarizations are [89]

$$\begin{aligned} i\hbar\frac{\partial}{\partial t}\Xi^{v,c}_{\mathbf{k},\mathbf{q}} &= \left[\tilde{E}^{c}_{\mathbf{k}+\mathbf{q}_e} - \tilde{E}^{v}_{\mathbf{k}-\mathbf{q}_h} - \hbar\Omega_{\mathbf{q}} - i\gamma^{v,c}_{T}\right]\Xi^{v,c}_{\mathbf{k},\mathbf{q}} - (1 - f^{e}_{\mathbf{k}+\mathbf{q}_e} - f^{h}_{\mathbf{k}-\mathbf{q}_h})\sum_{\mathbf{k}'} V_{\mathbf{k}-\mathbf{k}'}\Xi^{v,c}_{\mathbf{k}',\mathbf{q}} \\ &\quad + |G_{\mathbf{q}}|^{2}\left[(f^{e}_{\mathbf{k}+\mathbf{q}_e} + n_{\mathbf{q}})P^{vc}_{\mathbf{k}-\mathbf{q}_h} + (f^{h}_{\mathbf{k}-\mathbf{q}_h} + n_{\mathbf{q}})P^{vc}_{\mathbf{k}+\mathbf{q}_e}\right] \ , \end{aligned} \tag{C.5}$$

$$\begin{aligned} i\hbar\frac{\partial}{\partial t}\tilde{\Xi}^{c,v}_{\mathbf{k},\mathbf{q}} &= \left[\tilde{E}^{c}_{\mathbf{k}-\mathbf{q}_e} - \tilde{E}^{v}_{\mathbf{k}+\mathbf{q}_h} + \hbar\Omega_{\mathbf{q}} - i\gamma^{c,v}_{T}\right]\tilde{\Xi}^{c,v}_{\mathbf{k},\mathbf{q}} - (1 - f^{e}_{\mathbf{k}-\mathbf{q}_e} - f^{h}_{\mathbf{k}+\mathbf{q}_h})\sum_{\mathbf{k}'} V_{\mathbf{k}-\mathbf{k}'}\tilde{\Xi}^{c,v}_{\mathbf{k}',\mathbf{q}} \\ &\quad + |G_{\mathbf{q}}|^{2}\left[(1 - f^{e}_{\mathbf{k}-\mathbf{q}_e} + n_{\mathbf{q}})P^{vc}_{\mathbf{k}+\mathbf{q}_h} + (1 - f^{h}_{\mathbf{k}+\mathbf{q}_h} + n_{\mathbf{q}})P^{vc}_{\mathbf{k}-\mathbf{q}_e}\right] \ , \end{aligned} \tag{C.6}$$

where $\hbar\Omega_{\mathbf{q}}$ is phonon energy at wavevector $\mathbf{q}$, and $n_{\mathbf{q}}$ is phonon occupation that is assumed to be Bose-Einstein distribution. A constant dephasing γ_T is used for triplet correlations. The coupling

to other phonon correlations, photon–phonon correlations and carrier correlations have been ignored. In the following, we assume parabolic bands, and neglect carrier density in the source terms of Equations (C.5) and (C.6). Diagonalizing the homogeneous part of Equations (C.1), (C.5) and (C.6) using exciton basis, we obtain

$$i\hbar\frac{\partial}{\partial t}P_\lambda = (E_\lambda - i\gamma)P_\lambda - d_{vc}\phi^R_\lambda(r=0)\mathcal{E}(t) + \Gamma_\lambda \ , \tag{C.7}$$

$$i\hbar\frac{\partial}{\partial t}\Xi^{vc}_{\lambda,\mathbf{q}} = \left[E_\lambda + \frac{\hbar^2\mathbf{q}^2}{2M} - \hbar\Omega_\mathbf{q} - i\gamma_T\right]\Xi^{vc}_{\lambda,\mathbf{q}} + n_\mathbf{q}|G_\mathbf{q}|^2\sum_{\lambda'}F^{\lambda,\lambda'}_\mathbf{q}P_{\lambda'} \ , \tag{C.8}$$

$$i\hbar\frac{\partial}{\partial t}\tilde{\Xi}^{cv}_{\lambda,\mathbf{q}} = \left[E_\lambda + \frac{\hbar^2\mathbf{q}^2}{2M} + \hbar\Omega_\mathbf{q} - i\gamma_T\right]\tilde{\Xi}^{cv}_{\lambda,\mathbf{q}} + (1+n_\mathbf{q})|G_\mathbf{q}|^2\sum_{\lambda'}F^{\lambda,\lambda'}_{-\mathbf{q}}P_{\lambda'} \ , \tag{C.9}$$

where a form factor of is defined

$$F^{\lambda,\lambda'}_\mathbf{q} = \sum_\mathbf{k}\left[\phi^L_\lambda(\mathbf{k})\right]^*\left[\phi^R_{\lambda'}(\mathbf{k}-\mathbf{q}_h) + \phi^R_{\lambda'}(\mathbf{k}+\mathbf{q}_e)\right] \ . \tag{C.10}$$

Applying Fourier transform to Equations (C.7) to (C.9), we get

$$\begin{aligned}\Gamma_\lambda(\omega) &= \sum_\mathbf{k}\frac{1}{\mathcal{L}}\left[\phi^L_\lambda(\mathbf{k})\right]^*\sum_\mathbf{q}\sum_{\lambda'}\mathcal{L}\Big(\Xi^{v,c}_{\lambda',\mathbf{q}}(\omega)\left[\phi^R_{\lambda'}(\mathbf{k}+\mathbf{q}_h) + \phi^R_{\lambda'}(\mathbf{k}-\mathbf{q}_e)\right] \\ &\quad + \tilde{\Xi}^{c,v}_{\lambda',\mathbf{q}}(\omega)\left[\phi^R_{\lambda'}(\mathbf{k}-\mathbf{q}_h) + \phi^R_{\lambda'}(\mathbf{k}+\mathbf{q}_e)\right]\Big) \\ &= -\sum_{\lambda',\lambda''}\sum_\mathbf{q}\left[\frac{n_q|G_\mathbf{q}|^2F^{\lambda,\lambda'}_{-\mathbf{q}}F^{\lambda',\lambda''}_\mathbf{q}}{E_{\lambda'} + \frac{\hbar^2q^2}{2M} - \hbar\Omega_\mathbf{q} - i\gamma_T - \hbar\omega} + \frac{(1+n_q)|G_\mathbf{q}|^2F^{\lambda,\lambda'}_\mathbf{q}F^{\lambda',\lambda''}_{-\mathbf{q}}}{E_{\lambda'} + \frac{\hbar^2q^2}{2M} + \hbar\Omega_\mathbf{q} - i\gamma_T - \hbar\omega}\right]P_{\lambda''}(\omega) \ .\end{aligned} \tag{C.11}$$

Including only intra-exciton coupling, the Elliott formula for absorption is

$$\chi(\omega) = \frac{|d_{vc}|^2}{\epsilon_0}\sum_\lambda\frac{|\phi^R_\lambda(r=0)|^2}{E_\lambda - i\gamma - \hbar\omega - z^-_\lambda(\omega) - z^+_\lambda(\omega)} \ , \tag{C.12}$$

$$z^\pm_\lambda(\omega) = \sum_\mathbf{q}\frac{(n_\mathbf{q} + \frac{1}{2} \pm \frac{1}{2})|G^{\lambda,\lambda}_\mathbf{q}|^2}{E_\lambda + E_\mathbf{q} \pm \hbar\Omega_\mathbf{q} - i\gamma_T - \hbar\omega} \ , \tag{C.13}$$

where $z^{-(+)}_\lambda(\omega)$ involves phonon absorption (emission) processes, and $G^{\lambda,\lambda}_\mathbf{q}$ is exciton–phonon matrix elements

$$G^{\lambda,\lambda'}_\mathbf{q} = \sum_\mathbf{k}\left[\phi^L_\lambda(\mathbf{k})\right]^*\left[G^c_\mathbf{q}\phi^R_{\lambda'}(\mathbf{k}-\mathbf{q}_h) - G^v_\mathbf{q}\,\phi^R_{\lambda'}(\mathbf{k}+\mathbf{q}_e)\right] \ , \tag{C.14}$$

which is defined from left- (right-) handed exciton wave functions $\phi^{L(R)}_\lambda(\mathbf{k})$ and electron–phonon

matrix elements in conduction (valence) bands $G_{\mathbf{q}}^{c(v)}$.

APPENDIX D

Author's Contributions

The first project of my doctoral studies involved exploring the absorption properties of stacked monolayer crystals. This concept was partly driven by the theory predictions of large exciton binding energy in gallium nitride monolayer (Emmanouil Kioupakis) and recent breakthroughs in the growth of single-layer nitrides (Zetian Mi). My advisor, Mackillo Kira, discussed with me about the interesting idea of layering multiple monolayers to create a hyperspectral absorber. Based on semiconductor Bloch equations (SBEs) [35] and earlier work on multi-quantum-well systems [73], I wrote the code to compute absorption and tested various heterostructure designs. Initially, we encountered a challenge that the bandwidth of excitonic absorption was restrictively narrow. Then, my advisor inspired me to investigate the effects of continuum states. We found that absorption from continuum states could be significantly enhanced through radiative coupling, reaching a level comparable to excitonic absorption when a large number of monolayers are stacked. This was the key step in designing hyperspectral absorbers. This work was published in Q. Wen, Y. Wu, P. Wang, D. Laleyan, D. Bayerl, E. Kioupakis, Z. Mi, and M. Kira, *Hyperspectral absorption of semiconductor monolayer crystals*, Appl. Phys. Lett. **116**, 181103 (2020).

In 2018, I began exploring the theory of coherent phonons with Alexander Steinhoff and Matthias Florian, under the guidance of my advisor. This research was a collaborative effort with the group of Xiaoyang Zhu (Columbia University), who detected multiple sidebands in the $WSe_2/MoSe_2$ heterobilayers. In 2019, another set of experiments was done in the group of Parag Deotare, showing an intriguing sideband that occurred at the optical phonon energy. To investigate the origin of these sidebands, I computed charge-transfer dynamics in $WSe_2/MoSe_2$ heterobilayers using SBEs and investigated different possibilities for generating coherent phonons in this structure. During my analysis, my advisor shed light on the significant role of local charging effects, which were often overlooked in previous studies. Starting with an earlier work from Ada Bäumner [39], I applied the charging theory to the $WSe_2/MoSe_2$ heterobilayers to investigate how local charging affects electron dynamics. My calculations showed that local charging altered the electronic energies significantly which could lead to massive charge redistribution.

I then applied these insights from the studies of $WSe_2/MoSe_2$ heterobilayers to the charge-transfer dynamics in a double-quantum-well system. This research was in collaboration with the group of Rupert Huber (University of Regensburg), who observed unipolar pulses from GaAs-type double quantum wells, though the cause of these pulses was unknown. Guided by my advisor about theory development, I generalized the method from Ref. [39] to include multiple subbands in heterostructures. This allowed a self-consistent calculation of the charge distribution, which was the key aspect to precisely describe the carrier motion. I analyzed experimental data with the help from my advisor. Our theory prediction of the pulse shape aligned with experimental results. This study was published in C. Meineke, M. Prager, J. Hayes, Q. Wen, L. Z. Kastner, D. Schuh, K. Fritsch, O. Pronin, M. Stein, F. Schäfer, S. Chatterjee, M. Kira, R. Huber, and D. Bougeard, *Scalable high-repetition-rate sub-half-cycle terahertz pulses from spatially indirect interband transitions*, Light Sci. Appl. **11**, 1-8 (2022). In this paper, I contributed to the theory section as a co-author. The detailed theoretical approaches and perspectives to improve the pulse shape will be presented in a second paper Q. Wen, C. Meineke, R. Huber, and M. Kira, *Unipolar pulse generation from heterostructure charging dynamics.* (In preparation.)

In 2023, I began to work on a project to investigate the microscopic mechanism behind polarization switching in ferroelectrics. Guided by my advisor in theoretical derivations and computational schemes, I wrote the code to compute polarization switching described by the time-dependent Schrödinger equation. This analysis revealed the natural switching time, which I then related to a classical model to enhance the understanding. Collaborating with the group of Zetian Mi, who synthesized ScAlN ferroelectric sample, and the group of Rupert Huber, who conducted terahertz excitation experiments on these samples, we are now preparing a manuscript for the paper Q. Wen, Z. Mi, R. Huber, and M. Kira, *Terahertz switching in III-nitride ferroelectrics.* (In preparation.)

Bibliography

[1] Charles Kittel, *Introduction to Solid State Physics*, 8th ed. (Wiley).

[2] H. Haug and S. W. Koch, *Quantum Theory of the Optical and Electronic Properties of Semiconductors* (WORLD SCIENTIFIC).

[3] P. Yu and M. Cardona, *Fundamentals of Semiconductors* (Springer).

[4] K. S. Novoselov, A. K. Geim, S. V. Morozov, D. Jiang, Y. Zhang, S. V. Dubonos, I. V. Grigorieva, and A. A. Firsov, "Electric Field Effect in Atomically Thin Carbon Films", Science **306**, 666–669.

[5] K. F. Mak, C. Lee, J. Hone, J. Shan, and T. F. Heinz, "Atomically Thin MoS 2 : A New Direct-Gap Semiconductor", Physical Review Letters **105**, 136805.

[6] D. Bayerl, S. Islam, C. M. Jones, V. Protasenko, D. Jena, and E. Kioupakis, "Deep ultraviolet emission from ultra-thin GaN/AlN heterostructures", Applied Physics Letters **109**, 241102.

[7] M. Florian, M. Hartmann, A. Steinhoff, J. Klein, A. W. Holleitner, J. J. Finley, T. O. Wehling, M. Kaniber, and C. Gies, "The Dielectric Impact of Layer Distances on Exciton and Trion Binding Energies in van der Waals Heterostructures", Nano Letters **18**, 2725–2732.

[8] Y. Jiang, S. Chen, W. Zheng, B. Zheng, and A. Pan, "Interlayer exciton formation, relaxation, and transport in TMD van der Waals heterostructures", Light: Science & Applications **10**, 72.

[9] X. Hong, J. Kim, S.-F. Shi, Y. Zhang, C. Jin, Y. Sun, S. Tongay, J. Wu, Y. Zhang, and F. Wang, "Ultrafast charge transfer in atomically thin MoS2/WS2 heterostructures", Nature Nanotechnology **9**, 682–686.

[10] C. Jin, E. Y. Ma, O. Karni, E. C. Regan, F. Wang, and T. F. Heinz, "Ultrafast dynamics in van der Waals heterostructures", Nature Nanotechnology **13**, 994–1003.

[11] B. Miller, A. Steinhoff, B. Pano, J. Klein, F. Jahnke, A. Holleitner, and U. Wurstbauer, "Long-Lived Direct and Indirect Interlayer Excitons in van der Waals Heterostructures", Nano Letters **17**, 5229–5237.

[12] A. K. Geim and I. V. Grigorieva, “Van der Waals heterostructures”, Nature **499**, 419–425.

[13] J. Valasek, “Piezo-Electric and Allied Phenomena in Rochelle Salt”, Physical Review **17**, 475–481.

[14] D. D. Fong, G. B. Stephenson, S. K. Streiffer, J. A. Eastman, O. Auciello, P. H. Fuoss, and C. Thompson, “Ferroelectricity in Ultrathin Perovskite Films”, Science **304**, 1650–1653.

[15] I. Grinberg, D. V. West, M. Torres, G. Gou, D. M. Stein, L. Wu, G. Chen, E. M. Gallo, A. R. Akbashev, P. K. Davies, J. E. Spanier, and A. M. Rappe, “Perovskite oxides for visible-light-absorbing ferroelectric and photovoltaic materials”, Nature **503**, 509–512.

[16] S. Fichtner, N. Wolff, F. Lofink, L. Kienle, and B. Wagner, “AlScN: A III-V semiconductor based ferroelectric”, Journal of Applied Physics **125**, 114103.

[17] H. Wang, N. Adamski, S. Mu, and C. G. Van de Walle, “Piezoelectric effect and polarization switching in Al $_{1-x}$ Sc $_{x}$ N”, Journal of Applied Physics **130**, 104101.

[18] H. McAdams, R. Acklin, T. Blake, X.-H. Du, J. Eliason, J. Fong, W. Kraus, D. Liu, S. Madan, T. Moise, S. Natarajan, N. Qian, Y. Qiu, K. Remack, J. Rodriguez, J. Roscher, A. Seshadri, and S. Summerfelt, “A 64-Mb Embedded FRAM Utilizing a 130-nm 5LM Cu/FSG Logic Process”, IEEE Journal of Solid-State Circuits **39**, 667–677.

[19] K.-H. Kim, I. Karpov, R. H. Olsson, and D. Jariwala, “Wurtzite and fluorite ferroelectric materials for electronic memory”, Nature Nanotechnology **18**, 422–441.

[20] H. K. Yoo, J. S. Kim, Z. Zhu, Y. S. Choi, A. Yoon, M. R. MacDonald, X. Lei, T. Y. Lee, D. Lee, S. C. Chae, J. Park, D. Hemker, J. G. Langan, Y. Nishi, and S. J. Hong, “Engineering of ferroelectric switching speed in Si doped HfO2 for high-speed 1T-FERAM application”, in 2017 IEEE International Electron Devices Meeting (IEDM) (), pp. 19.6.1–19.6.4.

[21] M. Borsch, C. P. Schmid, L. Weigl, S. Schlauderer, N. Hofmann, C. Lange, J. T. Steiner, S. W. Koch, R. Huber, and M. Kira, “Super-resolution lightwave tomography of electronic bands in quantum materials”, Science **370**, 1204–1207.

[22] O. Schubert, M. Hohenleutner, F. Langer, B. Urbanek, C. Lange, U. Huttner, D. Golde, T. Meier, M. Kira, S. W. Koch, and R. Huber, “Sub-cycle control of terahertz high-harmonic generation by dynamical Bloch oscillations”, Nature Photonics **8**, 119–123.

[23] M. Borsch, M. Meierhofer, R. Huber, and M. Kira, “Lightwave electronics in condensed matter”, Nature Reviews Materials **8**, 668–687.

[24] A. Schiffrin, T. Paasch-Colberg, N. Karpowicz, V. Apalkov, D. Gerster, S. Mühlbrandt, M. Korbman, J. Reichert, M. Schultze, S. Holzner, J. V. Barth, R. Kienberger, R. Ernstorfer, V. S. Yakovlev, M. I. Stockman, and F. Krausz, "Optical-field-induced current in dielectrics", Nature **493**, 70–74.

[25] T. L. Cocker, D. Peller, P. Yu, J. Repp, and R. Huber, "Tracking the ultrafast motion of a single molecule by femtosecond orbital imaging", Nature **539**, 263–267.

[26] F. Langer, C. P. Schmid, S. Schlauderer, M. Gmitra, J. Fabian, P. Nagler, C. Schüller, T. Korn, P. G. Hawkins, J. T. Steiner, U. Huttner, S. W. Koch, M. Kira, and R. Huber, "Lightwave valleytronics in a monolayer of tungsten diselenide", Nature **557**, 76–80.

[27] N. H. Bonadeo, J. Erland, D. Gammon, D. Park, D. S. Katzer, and D. G. Steel, "Coherent Optical Control of the Quantum State of a Single Quantum Dot", Science **282**, 1473–1476.

[28] K. J. Yee, K. G. Lee, E. Oh, D. S. Kim, and Y. S. Lim, "Coherent Optical Phonon Oscillations in Bulk GaN Excited by Far below the Band Gap Photons", Physical Review Letters **88**, 105501.

[29] A. Gambetta, C. Manzoni, E. Menna, M. Meneghetti, G. Cerullo, G. Lanzani, S. Tretiak, A. Piryatinski, A. Saxena, R. L. Martin, and A. R. Bishop, "Real-time observation of nonlinear coherent phonon dynamics in single-walled carbon nanotubes", Nature Physics **2**, 515–520.

[30] T. D. Krauss and F. W. Wise, "Coherent Acoustic Phonons in a Semiconductor Quantum Dot", Physical Review Letters **79**, 5102–5105.

[31] T. Y. Jeong, B. M. Jin, S. H. Rhim, L. Debbichi, J. Park, Y. D. Jang, H. R. Lee, D.-H. Chae, D. Lee, Y.-H. Kim, S. Jung, and K. J. Yee, "Coherent Lattice Vibrations in Mono- and Few-Layer WSe_2", ACS Nano **10**, 5560–5566.

[32] C. Li, A. V. Scherbakov, P. Soubelet, A. K. Samusev, C. Ruppert, N. Balakrishnan, V. E. Gusev, A. V. Stier, J. J. Finley, M. Bayer, and A. V. Akimov, "Coherent Phonons in van der Waals $MoSe_2$ /WSe_2 Heterobilayers", Nano Letters **23**, 8186–8193.

[33] H. J. Zeiger, J. Vidal, T. K. Cheng, E. P. Ippen, G. Dresselhaus, and M. S. Dresselhaus, "Theory for displacive excitation of coherent phonons", Physical Review B **45**, 768–778.

[34] A. V. Kuznetsov and C. J. Stanton, "Theory of Coherent Phonon Oscillations in Semiconductors", Physical Review Letters **73**, 3243–3246.

[35] M. Kira and S. W. Koch, *Semiconductor Quantum Optics* (Cambridge University Press).

[36] F. Giustino, "Electron-phonon interactions from first principles", Reviews of Modern Physics **89**, 015003.

[37] W. Kohn and L. J. Sham, "Self-Consistent Equations Including Exchange and Correlation Effects", Physical Review **140**, A1133–A1138.

[38] M. Born and R. Oppenheimer, "Zur Quantentheorie der Molekeln", Annalen der Physik **389**, 457–484.

[39] A. Baumner, M. Kira, and S. W. Koch, "Charging Dynamics in Electrically Pumped Quantum Wells", IEEE JOURNAL OF QUANTUM ELECTRONICS **45**, 9.

[40] K. Wang, R. Dahan, M. Shentcis, Y. Kauffmann, A. Ben Hayun, O. Reinhardt, S. Tsesses, and I. Kaminer, "Coherent interaction between free electrons and a photonic cavity", Nature **582**, 50–54.

[41] J. Freudenstein, M. Borsch, M. Meierhofer, D. Afanasiev, C. P. Schmid, F. Sandner, M. Liebich, A. Girnghuber, M. Knorr, M. Kira, and R. Huber, "Attosecond clocking of correlations between Bloch electrons", Nature **610**, 290–295.

[42] J. Rauch and G. Mourou, "The time integrated far field for Maxwell's and D'Alembert's equations", Proceedings of the American Mathematical Society **134**, 851–858.

[43] P. Merkl, M. Knorr, C. Meineke, L. Kastner, D. Peller, and R. Huber, "Multibranch pulse synthesis and electro-optic detection of subcycle multi-terahertz electric fields", Optics Letters **44**, 5521.

[44] M. Plankl, P. E. Faria Junior, F. Mooshammer, T. Siday, M. Zizlsperger, F. Sandner, F. Schiegl, S. Maier, M. A. Huber, M. Gmitra, J. Fabian, J. L. Boland, T. L. Cocker, and R. Huber, "Subcycle contact-free nanoscopy of ultrafast interlayer transport in atomically thin heterostructures", Nature Photonics **15**, 594–600.

[45] C. Meineke, M. Prager, J. Hayes, Q. Wen, L. Z. Kastner, D. Schuh, K. Fritsch, O. Pronin, M. Stein, F. Schäfer, S. Chatterjee, M. Kira, R. Huber, and D. Bougeard, "Scalable high-repetition-rate sub-half-cycle terahertz pulses from spatially indirect interband transitions", Light: Science & Applications **11**, 151.

[46] D. Ahn and S. L. Chuang, "Model of the field-effect quantum-well laser with free-carrier screening and valence band mixing", Journal of Applied Physics **64**, 6143–6149.

[47] X. Liu, D. Wang, K.-H. Kim, K. Katti, J. Zheng, P. Musavigharavi, J. Miao, E. A. Stach, R. H. Olsson, and D. Jariwala, "Post-CMOS Compatible Aluminum Scandium Nitride/2D Channel Ferroelectric Field-Effect-Transistor Memory", Nano Letters **21**, 3753–3761.

[48] L. W. Martin and A. M. Rappe, "Thin-film ferroelectric materials and their applications", Nature Reviews Materials **2**, 16087.

[49] P. Wang, D. Wang, N. M. Vu, T. Chiang, J. T. Heron, and Z. Mi, "Fully epitaxial ferroelectric ScAlN grown by molecular beam epitaxy", Applied Physics Letters **118**, 223504.

[50] S. Calderon, J. Hayden, S. M. Baksa, W. Tzou, S. Trolier-McKinstry, I. Dabo, J.-P. Maria, and E. C. Dickey, "Atomic-scale polarization switching in wurtzite ferroelectrics", Science **380**, 1034–1038.

[51] P. Wang, D. Wang, S. Mondal, M. Hu, J. Liu, and Z. Mi, "Dawn of nitride ferroelectric semiconductors: from materials to devices", Semiconductor Science and Technology **38**, 043002.

[52] J. Li, B. Nagaraj, H. Liang, W. Cao, Chi. H. Lee, and R. Ramesh, "Ultrafast polarization switching in thin-film ferroelectrics", Applied Physics Letters **84**, 1174–1176.

[53] R. Mankowsky, A. Von Hoegen, M. Först, and A. Cavalleri, "Ultrafast Reversal of the Ferroelectric Polarization", Physical Review Letters **118**, 197601.

[54] F. Chen, Y. Zhu, S. Liu, Y. Qi, H. Y. Hwang, N. C. Brandt, J. Lu, F. Quirin, H. Enquist, P. Zalden, T. Hu, J. Goodfellow, M.-J. Sher, M. C. Hoffmann, D. Zhu, H. Lemke, J. Glownia, M. Chollet, A. R. Damodaran, J. Park, Z. Cai, I. W. Jung, M. J. Highland, D. A. Walko, J. W. Freeland, P. G. Evans, A. Vailionis, J. Larsson, K. A. Nelson, A. M. Rappe, K. Sokolowski-Tinten, L. W. Martin, H. Wen, and A. M. Lindenberg, "Ultrafast terahertz-field-driven ionic response in ferroelectric BaTiO 3", Physical Review B **94**, 180104.

[55] A. Grigoriev, D.-H. Do, D. M. Kim, C.-B. Eom, B. Adams, E. M. Dufresne, and P. G. Evans, "Nanosecond Domain Wall Dynamics in Ferroelectric Pb (Zr , Ti) O 3 Thin Films", Physical Review Letters **96**, 187601.

[56] J. Y. Jo, S. M. Yang, T. H. Kim, H. N. Lee, J.-G. Yoon, S. Park, Y. Jo, M. H. Jung, and T. W. Noh, "Nonlinear Dynamics of Domain-Wall Propagation in Epitaxial Ferroelectric Thin Films", Physical Review Letters **102**, 045701.

[57] S. Liu, I. Grinberg, and A. M. Rappe, "Intrinsic ferroelectric switching from first principles", Nature **534**, 360–363.

[58] K. Mølmer, Y. Castin, and J. Dalibard, "Monte Carlo wave-function method in quantum optics", Journal of the Optical Society of America B **10**, 524.

[59] P. R. Berman and V. S. Malinovsky, *Principles of Laser Spectroscopy and Quantum Optics* (Princeton University Press).

[60] W. Hu, S. Kaiser, D. Nicoletti, C. R. Hunt, I. Gierz, M. C. Hoffmann, M. Le Tacon, T. Loew, B. Keimer, and A. Cavalleri, "Optically enhanced coherent transport in YBa2Cu3O6.5 by ultrafast redistribution of interlayer coupling", Nature Materials **13**, 705–711.

[61] J. Wang, J. Ardelean, Y. Bai, A. Steinhoff, M. Florian, F. Jahnke, X. Xu, M. Kira, J. Hone, and X.-Y. Zhu, "Optical generation of high carrier densities in 2D semiconductor heterobilayers", Science Advances **5**, eaax0145.

[62] M. Kira and S. Koch, "Many-body correlations and excitonic effects in semiconductor spectroscopy", Prog. in Quant. Electron. **30**, 155–296.

[63] K. F. Mak, C. Lee, J. Hone, J. Shan, and T. F. Heinz, "Atomically thin MoS2: A new direct-gap semiconductor", Physical Review Letters **105**, 136805.

[64] F. Cadiz, E. Courtade, C. Robert, G. Wang, Y. Shen, H. Cai, T. Taniguchi, K. Watanabe, H. Carrere, D. Lagarde, M. Manca, T. Amand, P. Renucci, S. Tongay, X. Marie, and B. Urbaszek, "Excitonic linewidth approaching the homogeneous limit in MoS2-Based van der waals heterostructures", Physical Review X **7**, 021026.

[65] G. Scuri, Y. Zhou, A. A. High, D. S. Wild, C. Shu, K. De Greve, L. A. Jauregui, T. Taniguchi, K. Watanabe, P. Kim, M. D. Lukin, and H. Park, "Large excitonic reflectivity of monolayer MoSe2 encapsulated in hexagonal boron nitride", Physical Review Letters **120**, 037402.

[66] P. Back, S. Zeytinoglu, A. Ijaz, M. Kroner, and A. Imamoğğlu, "Realization of an electrically tunable narrow-bandwidth atomically thin mirror using monolayer MoSe2", Physical Review Letters **120**, 037401.

[67] J. Horng, Y.-H. Chou, T.-c. Chang, C.-Y. Hsu, T.-c. Lu, and H. Deng, *Engineering effects of vacuum fluctuations on two-dimensional semiconductors.*

[68] J. Horng, E. W. Martin, Y.-H. Chou, E. Courtade, T.-c. Chang, C.-Y. Hsu, M.-H. Wentzel, H. G. Ruth, T.-c. Lu, S. T. Cundiff, F. Wang, and H. Deng, *Perfect absorption by an atomically thin crystal.*

[69] D. Bayerl, S. M. Islam, C. M. Jones, V. Protasenko, D. Jena, and E. Kioupakis, "Deep ultraviolet emission from ultra-thin GaN/AlN heterostructures", Applied Physics Letters **109**, 241102.

[70] A. Aiello, Y. Wu, A. Pandey, P. Wang, W. Lee, D. Bayerl, N. Sanders, Z. Deng, J. Gim, K. Sun, R. Hovden, E. Kioupakis, Z. Mi, and P. Bhattacharya, "Deep ultraviolet luminescence due to extreme confinement in monolayer GaN/Al(Ga)N nanowire and planar heterostructures", Nano Letters **19**, 7852–7858.

[71] Y. Wu, X. Liu, P. Wang, D. A. Laleyan, K. Sun, Y. Sun, C. Ahn, M. Kira, E. Kioupakis, and Z. Mi, "Monolayer GaN excitonic deep ultraviolet light emitting diodes", Applied Physics Letters **116**, 013101.

[72] M. Kira and S. W. Koch, *Semiconductor quantum optics* (Cambridge University Press, Cambridge).

[73] T. Stroucken, A. Knorr, P. Thomas, and S. W. Koch, "Coherent dynamics of radiatively coupled quantum-well excitons", Physical Review B **53**, 2026–2033.

[74] C. E. Stevens, T. Stroucken, A. V. Stier, J. Paul, H. Zhang, P. Dey, S. A. Crooker, S. W. Koch, and D. Karaiskaj, "Superradiant coupling effects in transition-metal dichalcogenides", Optica **5**, 749–755.

[75] J. P. Prineas, C. Ell, E. S. Lee, G. Khitrova, H. M. Gibbs, and S. W. Koch, "Exciton-polariton eigenmodes in light-coupled $In_{0.04}Ga_{0.96}As$/GaAs semiconductor multiple-quantum-well periodic structures", Physical Review B **61**, 13863–13872.

[76] M. Florian, M. Hartmann, A. Steinhoff, J. Klein, A. W. Holleitner, J. J. Finley, T. O. Wehling, M. Kaniber, and C. Gies, "The dielectric impact of layer distances on exciton and trion binding energies in van der waals heterostructures", Nano Letters **18**, 2725–2732.

[77] M. Kira and S. W. Koch, "Exciton-population inversion and terahertz gain in semiconductors excited to resonance", Physical Review Letters **93**, 076402.

[78] S. Brem, J. Zipfel, M. Selig, A. Raja, L. Waldecker, J. D. Ziegler, T. Taniguchi, K. Watanabe, A. Chernikov, and E. Malic, "Intrinsic lifetime of higher excitonic states in tungsten diselenide monolayers", Nanoscale **11**, 12381–12387.

[79] K. Yoshikawa, W. Yoshida, T. Irie, H. Kawasaki, K. Konishi, H. Ishibashi, T. Asatani, D. Adachi, M. Kanematsu, H. Uzu, and K. Yamamoto, "Exceeding conversion efficiency of 26% by heterojunction interdigitated back contact solar cell with thin film Si technology", Solar Energy Materials and Solar Cells **173**, 37–42.

[80] Y. Wang, Y. Wu, K. Sun, and Z. Mi, "A quadruple-band metal–nitride nanowire artificial photosynthesis system for high efficiency photocatalytic overall solar water splitting", Materials Horizons **6**, 1454–1462.

[81] F. Chowdhury, M. Trudeau, H. Guo, and Z. Mi, "A photochemical diode artificial photosynthesis system for unassisted high efficiency overall pure water splitting", Nature Communications **9**, 1707.

[82] G. Cassabois, P. Valvin, and B. Gil, "Hexagonal boron nitride is an indirect bandgap semiconductor", Nature Photonics **10**, 262–266.

[83] L. Sponza, H. Amara, F. Ducastelle, A. Loiseau, and C. Attaccalite, "Exciton interference in hexagonal boron nitride", Physical Review B **97**, 075121.

[84] D. A. Laleyan, K. Mengle, S. Zhao, Y. Wang, E. Kioupakis, and Z. Mi, "Effect of growth temperature on the structural and optical properties of few-layer hexagonal boron nitride by molecular beam epitaxy", Optics Express **26**, 23031.

[85] T. Galvani, F. Paleari, H. P. C. Miranda, A. Molina-Sánchez, L. Wirtz, S. Latil, H. Amara, and F. Ducastelle, "Excitons in boron nitride single layer", Physical Review B **94**, 125303.

[86] F. Zhang, C. S. Ong, J. W. Ruan, M. Wu, X. Q. Shi, Z. K. Tang, and S. G. Louie, "Intervalley Excitonic Hybridization, Optical Selection Rules, and Imperfect Circular Dichroism in Monolayer h - BN", Physical Review Letters **128**, 047402.

[87] P. Wang, W. Lee, J. P. Corbett, W. H. Koll, N. M. Vu, D. A. Laleyan, Q. Wen, Y. Wu, A. Pandey, J. Gim, D. Wang, D. Y. Qiu, R. Hovden, M. Kira, J. T. Heron, J. A. Gupta, E. Kioupakis, and Z. Mi, "Scalable Synthesis of Monolayer Hexagonal Boron Nitride on Graphene with Giant Bandgap Renormalization", Advanced Materials **34**, 2201387.

[88] A. Chernikov, V. Bornwasser, M. Koch, S. Chatterjee, C. N. Böttge, T. Feldtmann, M. Kira, S. W. Koch, T. Wassner, S. Lautenschläger, B. K. Meyer, and M. Eickhoff, "Phonon-assisted luminescence of polar semiconductors: Fröhlich coupling versus deformation-potential scattering", Physical Review B **85**, 035201.

[89] M. Kira and S. Koch, "Many-body correlations and excitonic effects in semiconductor spectroscopy", Progress in Quantum Electronics **30**, 155–296.

[90] M. Selig, G. Berghäuser, A. Raja, P. Nagler, C. Schüller, T. F. Heinz, T. Korn, A. Chernikov, E. Malic, and A. Knorr, "Excitonic linewidth and coherence lifetime in monolayer transition metal dichalcogenides", Nature Communications **7**, 13279.